

**Finite Element Electrode and Individual Patient Modeling to Optimize Restorative
Neuroengineering**

by

Karlo A. Malaga

A dissertation submitted in partial fulfillment
of the requirements for the degree of
Doctor of Philosophy
(Biomedical Engineering)
in the University of Michigan
2019

Doctoral Committee:

Associate Professor Parag G. Patil, Chair
Assistant Professor Timothy M. Bruns
Associate Professor Cynthia A. Chestek
Associate Professor William C. Stacey

Karlo A. Malaga

karloma@umich.edu

ORCID iD: 0000-0001-9153-5032

© Karlo A. Malaga 2019

Dedication

This dissertation is dedicated to the memory of my mother, Herminia N. Malaga, who taught me to never give up.

Acknowledgements

I would like to thank my fellow (and former) members of the Restorative Neuroengineering Group, Sunjay Dodani, Layla Houshmand, Charles Lu, Dorsa Haji Ghaffari, Suseendrakumar Duraivel, Jayashree Chandrasekaran, Lilliana Colon-Sanchez, Joseph Costello, Nicole Bentley, Matthew Willsey, James Mossner, Kelly Lupo, Wilma Mackenzie, and Melissa Matthews, for their help, support, and friendship. Thanks to my doctoral committee, Dr. Parag Patil, Dr. Cynthia Chestek, Dr. Timothy Bruns, and Dr. William Stacey, for their feedback, advice, and guidance. I would especially like to thank Dr. Patil, my advisor, for teaching me more than I could ever give him credit for and for showing me firsthand what a good scientist, mentor, and person should be like.

Nobody has been more important to me in the pursuit of this degree than my family and friends. I would like to thank my parents, Bernard and Herminia Malaga, for their love, encouragement, and sacrifices. Special thanks to Dr. Lianette Rivera Báez, my other half, for exposing me to so many new things and for genuinely making me want to become a better person (because she deserves nothing less than the best).

This work would not have been possible without the financial support of the NSF Graduate Research Fellowship, the Ford Foundation Predoctoral Fellowship, and the University of Michigan Rackham Merit Fellowship. I am sincerely grateful to these organizations for their investment in my success.

Table of Contents

Dedication	ii
Acknowledgements.....	iii
List of Tables	vii
List of Figures	viii
Abstract	x
Chapter 1 Introduction	1
Background	1
Outline.....	5
References	8
Chapter 2 Atlas-Independent, N-of-1 Tissue Activation Modeling to Map the Optimal Location of Subthalamic Deep Brain Stimulation for Parkinson Disease	13
Abstract	13
Introduction	14
Methods.....	17
Patient Selection	17
Image Acquisition and Processing	19
Clinical Evaluation	19
Atlas-Independent, N-of-1 Tissue Activation Modeling.....	23
STN Segmentation.....	25
Electrode Contact Localization	25
Anisotropic Brain Tissue Conductivity Estimation.....	26
Finite Element Analysis.....	26

VTA Mapping.....	27
Optimality of Stimulation.....	28
Statistical Analysis	28
Results.....	29
Patient Motor Outcome	29
Optimal Location of Stimulation.....	29
Difference in Stimulation Location between Optimal and Sub-Optimal Stimulation.....	34
Relationship between Stimulation Location and Motor Improvement	37
Patient Variability in STN Anatomy and Stimulation Location.....	39
Discussion	42
Optimal Location of Stimulation.....	43
Difference in Stimulation Location between Optimal and Sub-Optimal Stimulation.....	44
Relationship between Stimulation Location and Motor Improvement	45
Patient Variability in STN Anatomy and Stimulation Location.....	46
Limitations and Alternative Modeling Approaches	47
Conclusion.....	50
References	51
Chapter 3 Clinical Validation of Atlas-Independent, N-of-1 Thalamic Segmentation and Tissue	
Activation Modeling in Thalamic Deep Brain Stimulation for Essential Tremor.....	59
Abstract	59
Introduction	61
Methods.....	63
Patient Selection	63
Pre-Operative Image Acquisition and Processing.....	65
Surgical Procedure and Initial Programming Session	65
Post-Operative Image Acquisition and Processing and Electrode Contact Localization.....	68
Thalamic Tracing and Atlas-Independent, N-of-1 Segmentation	68
Atlas-Independent, N-of-1 Tissue Activation Modeling.....	71
Atlas-Based Thalamic Segmentation.....	72
Statistical Analysis	72
Results.....	73

Clinical Outcome.....	73
Atlas-Independent, N-of-1 Thalamic Segmentation.....	74
Difference in Thalamic Anatomy	77
Difference in Therapeutic Contact Location	80
Difference in VTA Location and Predictive Capability	81
Discussion	87
Thalamic Segmentation	89
Therapeutic Contact Localization.....	91
Tissue Activation Modeling	92
Limitations, Alternative Approaches, and Future Directions.....	95
Conclusion.....	96
References	98
Chapter 4 Data-Driven Model Comparing the Effects of Glial Scarring and Interface Interactions on Chronic Neural Recordings in Non-Human Primates	105
Abstract	105
Introduction	106
Methods.....	110
Experimental Methods.....	110
Computational Methods	113
Results	119
Electrode Impedance	119
Waveform Amplitude	127
Relationship between Impedance and Signal Quality	133
Discussion	135
Conclusion.....	139
References	141
Chapter 5 Placing the Work in Context	145
Future Directions.....	148
References	152

List of Tables

Table 2-1 Patient demographics and post-operative change in LEDD with DBS	18
Table 2-2 Post-operative change in lateralized MDS-UPDRS III scores with DBS	21
Table 2-3 Clinical DBS settings, electrode impedance, and modeled VTA.....	22
Table 3-1 Patient demographics.....	64
Table 3-2 Clinical DBS settings, electrode impedance, and modeled VTA.....	67
Table 4-1 Material and electrical resistivity of FEM domains	116
Table 4-2 Distribution of regression slope in impedance (k Ω /week).....	126
Table 4-3 Distribution of regression slope in amplitude (μ V/week)	132

List of Figures

Figure 2-1 Atlas-independent, n-of-1 tissue activation modeling approach.....	24
Figure 2-2 Lateralized, post-operative MDS-UPDRS III scores and pre-operative LEDD without and with DBS.....	29
Figure 2-3 VTA mapping for overall motor improvement.....	31
Figure 2-4 VTA mapping for rigidity improvement.....	32
Figure 2-5 VTA mapping for bradykinesia improvement	33
Figure 2-6 VTA mapping for tremor improvement.....	34
Figure 2-7 Difference in stimulation location between patients with optimal and sub-optimal stimulation.....	37
Figure 2-8 Relationship between stimulation location and motor improvement.....	39
Figure 2-9 Variability in STN anatomy and stimulation location across patients	39
Figure 2-10 Variability in STN location and size across patients	40
Figure 2-11 Variability in active contact position across patients	41
Figure 2-12 Variability in VTA location across patients.....	42
Figure 3-1 Thalamic tracing for one patient	69
Figure 3-2 Comparison of tensor distance metrics for n-of-1 thalamic segmentation	75
Figure 3-3 Stability analysis for n-of-1 thalamic segmentation.....	76
Figure 3-4 Comparison of n-of-1 and atlas-based thalamic segmentation for one patient.....	77

Figure 3-5 Difference in subnuclei location and size between n-of-1 and atlas-based thalamic segmentation	79
Figure 3-6 Difference in therapeutic contact location between n-of-1 and atlas-based thalamic segmentation	81
Figure 3-7 Difference in the amount of motor and sensory thalamus stimulation associated with therapeutic VTAs between n-of-1 and atlas-based thalamic segmentation	83
Figure 3-8 Difference in the amount of sensory thalamus stimulation associated with therapeutic and sustained paresthesia VTAs between n-of-1 and atlas-based thalamic segmentation	85
Figure 3-9 Difference in the amount of external stimulation associated with therapeutic and dysarthria/motor contraction VTAs between n-of-1 and atlas-based thalamic segmentation	87
Figure 4-1 Neural recording model.....	114
Figure 4-2 Mean impedance (at 1 kHz) over time (3/4 pooled arrays, all viable electrodes)	120
Figure 4-3 Effect of encapsulation thickness on impedance	122
Figure 4-4 Gliosis around the electrodes obtained from one monkey 17 weeks post-implantation	123
Figure 4-5 Effect of encapsulation and interface resistivity on impedance.....	124
Figure 4-6 Distribution of regression slope and measurement-to-measurement difference in impedance (all viable electrodes, 238/288)	125
Figure 4-7 Mean amplitude over time (3/4 pooled arrays, all viable electrodes).....	128
Figure 4-8 Effect of encapsulation and interface on amplitude.....	130
Figure 4-9 Distribution of regression slope in amplitude (all viable electrodes, 238/288)	131
Figure 4-10 Correlation between impedance and amplitude (all viable electrodes, 238/288) ...	134

Abstract

Parkinson disease (PD) and essential tremor (ET) are the most common neurological movement disorders among adults. Deep brain stimulation (DBS) is an established surgical treatment for both conditions that involves implanting electrodes in the brain and then applying electrical stimulation. Despite the clinical effectiveness of DBS, its underlying mechanisms remain unclear. As DBS advances into a viable treatment for other conditions, it has become important to address the fundamental principles behind the procedure, specifically the spatial extent of stimulation. Furthermore, as DBS moves toward the adoption of closed-loop stimulation paradigms, an increased understanding of how neural recordings are affected by different biological factors is also key. Broadly, this work utilizes finite element electrode and individual patient modeling in an effort to help improve established procedures within Restorative Neuroengineering.

The first study presents an atlas-independent, n-of-1 tissue activation modeling methodology utilizing diffusion tensor imaging to map the optimal location of subthalamic DBS for PD. The volume of tissue activated (VTA) was modeled using finite element analysis for 40 PD patients. High variability in neuroanatomy, stimulation location, and motor improvement was observed across patients, highlighting the need for n-of-1 modeling approaches. The optimal stimulation location was mapped to the dorsolateral border of the subthalamic nucleus, in the posterior half. Therapeutic VTAs spread further in the dorsal direction, providing more evidence for caudal zona incerta as an important DBS target.

The second study applies the VTA modeling methodology from the previous study to thalamic DBS for ET and combines it with atlas-independent, n-of-1 thalamic segmentation to evaluate the effects of DBS on individual patients. Twenty-two ET patients were modeled. Thalami were segmented into 13 distinct subnuclei using a k-means clustering algorithm. Therapeutic and side effect-inducing VTAs were calculated. Results were compared with those obtained using an atlas-based segmentation approach. Within the thalamus, the shape and size of the VTA was highly variable across patients. Overall, n-of-1 segmentation performed better than atlas-based segmentation in explaining DBS side effects.

The third study investigates the effects of gliosis and interface interactions at the electrode recording site on single-unit recording quality using a computational model incorporating impedance and neural data from Utah arrays implanted in rhesus macaques. A finite element model of a Utah array microelectrode in neural tissue was coupled with a multi-compartment neuron model to quantify the effects of encapsulation thickness, encapsulation resistivity, and interface resistivity on electrode impedance and waveform amplitude. The neural recording model was then reconciled with the *in vivo* data. From week 1-3, mean impedance and amplitude increased at rates of 115.8 k Ω /week and 23.1 μ V/week, respectively. This initial ramp up in impedance and amplitude was consistent with increasing interface resistivity and tissue resistivity, respectively, in the model. The modeled gliosis could not match the *in vivo* data. However, a thin interface layer at the recording site could. Despite having a large effect on impedance, interface resistivity did not have a noticeable effect on amplitude, suggesting that gliosis does not cause an electrical problem with regard to signal quality.

The significance of this work is in the n-of-1 modeling framework that it provides. As insight regarding stimulation spread in the brain increases, the techniques described can be

applied to other conditions to inform novel stimulation strategies and help bridge the gap between model-based evidence and clinical practice.

Chapter 1

Introduction

Background

Parkinson disease (PD) and essential tremor (ET) are two of the most common neurological movement disorders among adults. The prevalence of PD and ET increases with age and is estimated to be 1.8% (de Rijk et al., 2000) and 4.6% (Louis and Ferreira, 2010), respectively, in individuals aged 65 or older. Parkinson disease is characterized by resting tremor, rigidity, bradykinesia, and postural instability, while ET is characterized exclusively by action tremor. There is currently no cure for PD or ET. However, a surgical procedure called deep brain stimulation (DBS) has emerged as a safe and effective treatment for PD and ET (DeLong and Wichmann, 2012). More than 100,000 patients worldwide have received DBS (Sugiyama et al., 2015). The procedure involves implanting electrodes in specific regions of the brain, such as the subthalamic nucleus (STN) for PD and ventral intermediate (VIM) nucleus of the thalamus for ET, and then applying chronic high-frequency electrical stimulation to those regions.

Despite the clinical effectiveness of DBS, the underlying mechanisms by which it provides therapeutic benefit remain unclear (Deniau et al., 2010; Florence et al., 2016; Johnson et al., 2008; McIntyre et al., 2004c; McIntyre et al., 2004d; McIntyre and Thakor, 2002; Montgomery and Gale, 2008; Vitek, 2002; Vitek, 2008). Deep brain stimulation is hypothesized to modulate pathological network activity by activating axons and inhibiting cell bodies

(McIntyre et al., 2004a; McIntyre and Hahn, 2010). However, this hypothesis has yet to be proven definitively and alternative hypotheses also exist (Chiken and Nambu, 2014, 2016). This lack of understanding translates to the clinic. For example, post-operative DBS programming to determine optimal stimulation parameters for a patient (amplitude, frequency, and pulse width) often relies on a trial-and-error approach, which makes the process both difficult and time-consuming (Kuncel and Grill, 2004). Such an approach can result in patients receiving sub-optimal stimulation and requiring surgical revision (Okun et al., 2005). As DBS advances into a viable treatment for other conditions, such as chronic pain and major depression (Perlmutter and Mink, 2006), it has become increasingly more important to address the fundamental principles behind the procedure, specifically the spatial extent of neural activation.

The therapeutic benefit of DBS is strongly dependent on the spatial distribution of the stimulation-induced electric field relative to the individual neuroanatomy of the patient undergoing treatment (Kuncel et al., 2008; Maks et al., 2009; McIntyre et al., 2004b). To maximize symptom suppression while minimizing side effects, such as paresthesia, dysarthria, and dyskinesia, accurate predictions of the spread of stimulation in the brain are essential. Due to the inherent difficulty in measuring the electric field *in vivo*, computational models of DBS have been used to visualize and quantify the spatial extent of neural activation, termed the volume of tissue activated (VTA) (Butson, 2012). The VTA is a stimulation parameter-dependent metric that can be used to predict clinical outcomes (Butson et al., 2007; Butson and McIntyre, 2006b; Chaturvedi et al., 2006; Chaturvedi et al., 2010), optimize stimulation parameters (Cooper et al., 2008; Frankemolle et al., 2010; McIntyre et al., 2006; McIntyre et al., 2009), identify alternative DBS targets (Butson et al., 2011; Cooper et al., 2014; Miocinovic et al., 2006; Zitella et al., 2013), and design novel electrodes (Buhlmann et al., 2011; Butson and McIntyre, 2006a; Howell

et al., 2015; Keane et al., 2012; Martens et al., 2011; van Dijk et al., 2015). The clinical utility of these models hinges on their ability to make meaningful and accurate predictions. Significant efforts have gone towards validating VTA predictions with experimental data (Miocinovic et al., 2009; Zitella et al., 2015).

Tissue activation modeling continues to grow more complex over time. For example, models can now incorporate detailed neuroanatomy, heterogeneous and anisotropic tissue properties, explicit representation of the DBS lead and electrode-tissue interface, and clinically determined stimulation parameters (Butson et al., 2007). Model complexity can be further augmented by the addition of biophysical neuron models (McIntyre and Grill, 1999; McIntyre et al., 2002). Each of these modeling advancements have been made in an effort to tailor DBS models to individual patients. However, there is still room for improvement when it comes to creating truly n-of-1 models. For example, deep brain structures are typically derived from a brain atlas, translated, rotated, and scaled to best fit the anatomy of the patient (Miocinovic et al., 2007). Anisotropic tissue properties, derived from diffusion tensor (DT) imaging, are also typically atlas-based (Wakana et al., 2004). Since most atlases are based on a single subject, there is a limitation in how representative one can be to a patient population, especially one that is in a diseased state (Dickie et al., 2017; Nowacki et al., 2018). Individual patients respond differently to DBS. For example, the optimal stimulation parameters for one patient may induce side effects in another. This is why it is important that DBS is tailored to the individual needs of the patient (Okun and Foote, 2010). Tissue activation modeling should follow suit by deriving all model components from a single source (the patient being modeled) to accurately characterize the VTA.

Deep brain stimulation is only one example of brain-machine interface (BMI) technology. In general, BMIs are neuroprosthetic devices created to restore motor, sensory, and/or cognitive function to patients with neurological disorders (Collinger et al., 2014; Hochberg et al., 2006; Taylor et al., 2002). However, the term BMI is typically reserved for devices that record electrical signals from the brain to control separate devices, such as robotic limbs. These neural signals can come from different sources, such as electroencephalography, electrocorticography, and single-unit recordings, that vary in their degree of invasiveness. For single-unit recordings, action potentials from individual neurons are measured using electrodes implanted in the brain. Notable examples of intracortical microelectrode arrays used to record single-unit activity include microwires (Williams et al., 1999), Michigan probes (Vetter et al., 2004), and Utah arrays (Nordhausen et al., 1996). Recordings from such devices provide high spatial resolution. However, it can be difficult to identify and isolate individual units. For BMIs to become clinically viable, electrode arrays must be able to acquire stable, high-quality signals for years. The ability to reliably record single-unit activity with intracortical microelectrode arrays is currently hindered by low signal-to-noise ratio (SNR), which can come from a variety of biological, material, or mechanical failure modes (Barrese et al., 2013).

Alongside experimental studies, computational models have been developed to increase the understanding of neural recordings and how they are affected by different factors (Holt and Koch, 1999; Lempka et al., 2011; Mainen et al., 1995; Moffitt and McIntyre, 2005; Reimann et al., 2013). These models employ many of the same tools used in DBS modeling, such as finite element analysis and neuron modeling, and can make interesting predictions, encouraging further investigation. For example, Moffitt and McIntyre reported that electrode encapsulation increased the amplitude of neural waveforms (Moffitt and McIntyre, 2005), a finding that challenged

current assumptions regarding the effect of gliosis on single-unit recordings. As DBS technology progresses towards the adoption of closed-loop stimulation paradigms, where brain signals are recorded to control how stimulation is delivered in real-time (Ghasemi et al., 2018), an increased understanding of how chronic neural recordings are affected by different biological factors is important.

Outline

The objective of the work in this dissertation is two-fold: (1) to characterize the spatial extent of neural activation associated with therapeutic outcome and side effects in STN and VIM DBS for PD and ET, respectively, by developing atlas-independent, truly n-of-1 DT-based tissue activation models; (2) to investigate the effects of gliosis and the electrode-tissue interface on single-unit recording quality by developing a data-driven neural recording model.

Chapter 2 presents an atlas-independent, truly n-of-1 tissue activation modeling methodology utilizing patient DT imaging to map the optimal location of STN DBS for PD and evaluate the relationship between VTAs associated with therapeutic outcome and symptom-specific motor improvement. The stimulation-induced electric field for 40 PD patients treated with bilateral STN DBS was modeled using finite element analysis. Tissue activation models were tailored to each patient, incorporating their individual STN anatomy, DBS lead position and orientation, anisotropic brain tissue conductivity, and clinical stimulation settings. A voxel-based analysis of the VTAs was used to map the optimal location of stimulation. High variability in neuroanatomy, stimulation location, and motor improvement across patients was observed, highlighting the need for n-of-1 modeling approaches. The optimal location of stimulation was mapped to the dorsolateral border of the STN, in the posterior half of the nucleus. Therapeutic

VTAAs spread noticeably more in the dorsal direction, providing further evidence for caudal zona incerta as an important DBS target.

Chapter 3 presents a novel modeling methodology to evaluate the clinical effects of VIM DBS for ET on an individual patient basis – one that combines DT-based, atlas-independent thalamic segmentation and tissue activation modeling. Twenty-two ET patients treated with unilateral VIM DBS were modeled. For each patient, the thalamus was segmented into 13 distinct subnuclei using a modified, k-means clustering algorithm. Volumes of tissue activation associated with therapeutic outcome (tremor suppression) and side effects (sustained paresthesia and dysarthria/motor contraction) were calculated by applying the modeling methodology presented in Chapter 2. The amount of VTA overlap with the motor and sensory regions of the thalamus was then measured to correlate motor and sensory thalamus stimulation with observed outcomes. The results obtained using n-of-1 thalamic segmentation were compared with those obtained using an atlas-based segmentation approach. Within the thalamus, the shape and size of the VTA, even with similar stimulation parameters, was highly variable across patients. Both segmentation approaches showed that therapeutic VTAs had significantly more overlap with motor than sensory thalamus and that sustained paresthesia VTAs had significantly more overlap with sensory thalamus than therapeutic VTAs. Only n-of-1 thalamic segmentation showed that dysarthria/motor contraction VTAs had significantly more external stimulation than therapeutic VTAs. Overall, n-of-1 thalamic segmentation performed better than atlas-based segmentation in terms of explaining DBS side effects, especially when the thalamic anatomy of the patient differed considerably in size and shape from the atlas thalamus.

Chapter 4 investigates the effects of gliosis and interface interactions at the electrode recording site on single-unit recording quality using a computational model incorporating

impedance and neural data acquired from chronically-implanted Utah arrays in rhesus macaques. A finite element model of a Utah array microelectrode in neural tissue was coupled with a multi-compartment model of a neuron to quantify the effects of encapsulation thickness, encapsulation resistivity, and interface resistivity on electrode impedance and waveform amplitude. The neural recording model was then reconciled with the *in vivo* data. From week 1-3, mean impedance and amplitude increased at rates of 115.8 k Ω /week and 23.1 μ V/week, respectively. This initial ramp up in impedance and amplitude was observed across all arrays, and is consistent with biofouling (increasing interface resistivity) and edema clearing (increasing tissue resistivity), respectively, in the model. Beyond week 3, the trends leveled out. In the model, gliosis could not match the *in vivo* data. However, a thin interface layer at the recording site could. Despite having a large effect on impedance, interface resistivity did not have a noticeable effect on amplitude. These findings suggest that gliosis does not cause an electrical problem with regard to signal quality since it does not appear to be the main contributor to increasing impedance or significantly affect amplitude. This, in turn, suggests that neural recordings can be obtained reliably despite gliosis as long as the recording site has sufficiently low impedance after accumulating a thin layer of biofouling.

Lastly, Chapter 5 discusses the main results of each study and their implications, and expands upon the n-of-1 and data-driven modeling framework that this work provides, specifically how it can be used to develop, validate, evaluate, and translate new approaches for improving clinical outcome in patients with neurological disorders.

References

- Barrese, J.C., Rao, N., Paroo, K., Triebwasser, C., Vargas-Irwin, C., Franquemont, L., Donoghue, J.P., 2013. Failure mode analysis of silicon-based intracortical microelectrode arrays in non-human primates. *J Neural Eng* 10, 066014.
- Buhlmann, J., Hofmann, L., Tass, P.A., Hauptmann, C., 2011. Modeling of a segmented electrode for desynchronizing deep brain stimulation. *Front Neuroeng* 4, 15.
- Butson, C.R., 2012. Computational models of neuromodulation. *Int Rev Neurobiol* 107, 5-22.
- Butson, C.R., Cooper, S.E., Henderson, J.M., McIntyre, C.C., 2007. Patient-specific analysis of the volume of tissue activated during deep brain stimulation. *NeuroImage* 34, 661-670.
- Butson, C.R., Cooper, S.E., Henderson, J.M., Wolgamuth, B., McIntyre, C.C., 2011. Probabilistic analysis of activation volumes generated during deep brain stimulation. *NeuroImage* 54, 2096-2104.
- Butson, C.R., McIntyre, C.C., 2006a. Role of electrode design on the volume of tissue activated during deep brain stimulation. *Journal of neural engineering* 3, 1-8.
- Butson, C.R., McIntyre, C.C., 2006b. Role of electrode design on the volume of tissue activated during deep brain stimulation. *J Neural Eng* 3, 1-8.
- Chaturvedi, A., Butson, C.R., Cooper, S.E., McIntyre, C.C., 2006. Subthalamic nucleus deep brain stimulation: accurate axonal threshold prediction with diffusion tensor based electric field models. *Conf Proc IEEE Eng Med Biol Soc* 1, 1240-1243.
- Chaturvedi, A., Butson, C.R., Lempka, S.F., Cooper, S.E., McIntyre, C.C., 2010. Patient-specific models of deep brain stimulation: influence of field model complexity on neural activation predictions. *Brain Stimul* 3, 65-67.
- Chiken, S., Nambu, A., 2014. Disrupting neuronal transmission: mechanism of DBS? *Front Syst Neurosci* 8, 33.
- Chiken, S., Nambu, A., 2016. Mechanism of Deep Brain Stimulation: Inhibition, Excitation, or Disruption? *Neuroscientist* 22, 313-322.
- Collinger, J.L., Kryger, M.A., Barbara, R., Betler, T., Bowsher, K., Brown, E.H., Clanton, S.T., Degenhart, A.D., Foldes, S.T., Gaunt, R.A., Gyulai, F.E., Harchick, E.A., Harrington, D., Helder, J.B., Hemmes, T., Johannes, M.S., Katyal, K.D., Ling, G.S., McMorland, A.J., Palko, K., Para, M.P., Scheuermann, J., Schwartz, A.B., Skidmore, E.R., Solzbacher, F., Srikameswaran, A.V., Swanson, D.P., Swetz, S., Tyler-Kabara, E.C., Velliste, M., Wang, W., Weber, D.J., Wodlinger, B., Boninger, M.L., 2014. Collaborative approach in the development of high-performance brain-computer interfaces for a neuroprosthetic arm: translation from animal models to human control. *Clin Transl Sci* 7, 52-59.

- Cooper, S.E., Driesslein, K.G., Noecker, A.M., McIntyre, C.C., Machado, A.M., Butson, C.R., 2014. Anatomical targets associated with abrupt versus gradual washout of subthalamic deep brain stimulation effects on bradykinesia. *PLoS one* 9, e99663.
- Cooper, S.E., Kuncel, A.M., Wolgamuth, B.R., Rezai, A.R., Grill, W.M., 2008. A model predicting optimal parameters for deep brain stimulation in essential tremor. *J Clin Neurophysiol* 25, 265-273.
- de Rijk, M.C., Launer, L.J., Berger, K., Breteler, M.M., Dartigues, J.F., Baldereschi, M., Fratiglioni, L., Lobo, A., Martinez-Lage, J., Trenkwalder, C., Hofman, A., 2000. Prevalence of Parkinson's disease in Europe: A collaborative study of population-based cohorts. Neurologic Diseases in the Elderly Research Group. *Neurology* 54, S21-23.
- DeLong, M., Wichmann, T., 2012. Deep brain stimulation for movement and other neurologic disorders. *Ann N Y Acad Sci* 1265, 1-8.
- Deniau, J.M., Degos, B., Bosch, C., Maurice, N., 2010. Deep brain stimulation mechanisms: beyond the concept of local functional inhibition. *Eur J Neurosci* 32, 1080-1091.
- Dickie, D.A., Shenkin, S.D., Anblagan, D., Lee, J., Blesa Cabez, M., Rodriguez, D., Boardman, J.P., Waldman, A., Job, D.E., Wardlaw, J.M., 2017. Whole Brain Magnetic Resonance Image Atlases: A Systematic Review of Existing Atlases and Caveats for Use in Population Imaging. *Front Neuroinform* 11, 1.
- Florence, G., Sameshima, K., Fonoff, E.T., Hamani, C., 2016. Deep Brain Stimulation: More Complex than the Inhibition of Cells and Excitation of Fibers. *Neuroscientist* 22, 332-345.
- Frankemolle, A.M., Wu, J., Noecker, A.M., Voelcker-Rehage, C., Ho, J.C., Vitek, J.L., McIntyre, C.C., Alberts, J.L., 2010. Reversing cognitive-motor impairments in Parkinson's disease patients using a computational modelling approach to deep brain stimulation programming. *Brain* 133, 746-761.
- Ghasemi, P., Sahraee, T., Mohammadi, A., 2018. Closed- and Open-loop Deep Brain Stimulation: Methods, Challenges, Current and Future Aspects. *J Biomed Phys Eng* 8, 209-216.
- Hochberg, L.R., Serruya, M.D., Friehs, G.M., Mukand, J.A., Saleh, M., Caplan, A.H., Branner, A., Chen, D., Penn, R.D., Donoghue, J.P., 2006. Neuronal ensemble control of prosthetic devices by a human with tetraplegia. *Nature* 442, 164-171.
- Holt, G.R., Koch, C., 1999. Electrical interactions via the extracellular potential near cell bodies. *J Comput Neurosci* 6, 169-184.
- Howell, B., Huynh, B., Grill, W.M., 2015. Design and *in vivo* evaluation of more efficient and selective deep brain stimulation electrodes. *J Neural Eng* 12, 046030.
- Johnson, M.D., Miocinovic, S., McIntyre, C.C., Vitek, J.L., 2008. Mechanisms and targets of deep brain stimulation in movement disorders. *Neurotherapeutics* 5, 294-308.

Keane, M., Deyo, S., Abosch, A., Bajwa, J.A., Johnson, M.D., 2012. Improved spatial targeting with directionally segmented deep brain stimulation leads for treating essential tremor. *J Neural Eng* 9, 046005.

Kuncel, A.M., Cooper, S.E., Grill, W.M., 2008. A method to estimate the spatial extent of activation in thalamic deep brain stimulation. *Clin Neurophysiol* 119, 2148-2158.

Kuncel, A.M., Grill, W.M., 2004. Selection of stimulus parameters for deep brain stimulation. *Clin Neurophysiol* 115, 2431-2441.

Lempka, S.F., Johnson, M.D., Moffitt, M.A., Otto, K.J., Kipke, D.R., McIntyre, C.C., 2011. Theoretical analysis of intracortical microelectrode recordings. *J Neural Eng* 8, 045006.

Louis, E.D., Ferreira, J.J., 2010. How common is the most common adult movement disorder? Update on the worldwide prevalence of essential tremor. *Mov Disord* 25, 534-541.

Mainen, Z.F., Joerges, J., Huguenard, J.R., Sejnowski, T.J., 1995. A model of spike initiation in neocortical pyramidal neurons. *Neuron* 15, 1427-1439.

Maks, C.B., Butson, C.R., Walter, B.L., Vitek, J.L., McIntyre, C.C., 2009. Deep brain stimulation activation volumes and their association with neurophysiological mapping and therapeutic outcomes. *J Neurol Neurosurg Psychiatry* 80, 659-666.

Martens, H.C.F., Toader, E., Decre, M.M.J., Anderson, D.J., Vetter, R., Kipke, D.R., Baker, K.B., Johnson, M.D., Vitek, J.L., 2011. Spatial steering of deep brain stimulation volumes using a novel lead design. *Clin Neurophysiol* 122, 558-566.

McIntyre, C.C., Butson, C.R., Maks, C.B., Noecker, A.M., 2006. Optimizing deep brain stimulation parameter selection with detailed models of the electrode-tissue interface. *Conf Proc IEEE Eng Med Biol Soc* 1, 893-895.

McIntyre, C.C., Frankenmolle, A.M., Wu, J., Noecker, A.M., Alberts, J.L., 2009. Customizing deep brain stimulation to the patient using computational models. *Conf Proc IEEE Eng Med Biol Soc* 2009, 4228-4229.

McIntyre, C.C., Grill, W.M., 1999. Excitation of central nervous system neurons by nonuniform electric fields. *Biophys J* 76, 878-888.

McIntyre, C.C., Grill, W.M., Sherman, D.L., Thakor, N.V., 2004a. Cellular effects of deep brain stimulation: model-based analysis of activation and inhibition. *J Neurophysiol* 91, 1457-1469.

McIntyre, C.C., Hahn, P.J., 2010. Network perspectives on the mechanisms of deep brain stimulation. *Neurobiol Dis* 38, 329-337.

McIntyre, C.C., Mori, S., Sherman, D.L., Thakor, N.V., Vitek, J.L., 2004b. Electric field and stimulating influence generated by deep brain stimulation of the subthalamic nucleus. *Clin Neurophysiol* 115, 589-595.

- McIntyre, C.C., Richardson, A.G., Grill, W.M., 2002. Modeling the excitability of mammalian nerve fibers: influence of afterpotentials on the recovery cycle. *J Neurophysiol* 87, 995-1006.
- McIntyre, C.C., Savasta, M., Kerkerian-Le Goff, L., Vitek, J.L., 2004c. Uncovering the mechanism(s) of action of deep brain stimulation: activation, inhibition, or both. *Clin Neurophysiol* 115, 1239-1248.
- McIntyre, C.C., Savasta, M., Walter, B.L., Vitek, J.L., 2004d. How Does Deep Brain Stimulation Work? Present Understanding and Future Questions. *Journal of Clinical Neurophysiology* 21, 40-50.
- McIntyre, C.C., Thakor, N.V., 2002. Uncovering the Mechanisms of Deep Brain Stimulation for Parkinson's Disease through Functional Imaging, Neural Recording, and Neural Modeling. *Critical Reviews? in Biomedical Engineering* 30, 249-282.
- Miocinovic, S., Lempka, S.F., Russo, G.S., Maks, C.B., Butson, C.R., Sakaie, K.E., Vitek, J.L., McIntyre, C.C., 2009. Experimental and theoretical characterization of the voltage distribution generated by deep brain stimulation. *Exp Neurol* 216, 166-176.
- Miocinovic, S., Noecker, A.M., Maks, C.B., Butson, C.R., McIntyre, C.C., 2007. Cicerone: stereotactic neurophysiological recording and deep brain stimulation electrode placement software system. *Acta Neurochir Suppl* 97, 561-567.
- Miocinovic, S., Parent, M., Butson, C.R., Hahn, P.J., Russo, G.S., Vitek, J.L., McIntyre, C.C., 2006. Computational analysis of subthalamic nucleus and lenticular fasciculus activation during therapeutic deep brain stimulation. *J Neurophysiol* 96, 1569-1580.
- Moffitt, M.A., McIntyre, C.C., 2005. Model-based analysis of cortical recording with silicon microelectrodes. *Clin Neurophysiol* 116, 2240-2250.
- Montgomery, E.B., Jr., Gale, J.T., 2008. Mechanisms of action of deep brain stimulation(DBS). *Neurosci Biobehav Rev* 32, 388-407.
- Nordhausen, C.T., Maynard, E.M., Normann, R.A., 1996. Single unit recording capabilities of a 100 microelectrode array. *Brain Res* 726, 129-140.
- Nowacki, A., Nguyen, T.A., Tinkhauser, G., Petermann, K., Debove, I., Wiest, R., Pollo, C., 2018. Accuracy of different three-dimensional subcortical human brain atlases for DBS -lead localisation. *Neuroimage Clin* 20, 868-874.
- Okun, M.S., Foote, K.D., 2010. Parkinson's disease DBS: what, when, who and why? The time has come to tailor DBS targets. *Expert review of neurotherapeutics* 10, 1847-1857.
- Okun, M.S., Tagliati, M., Pourfar, M., Fernandez, H.H., Rodriguez, R.L., Alterman, R.L., Foote, K.D., 2005. Management of referred deep brain stimulation failures: a retrospective analysis from 2 movement disorders centers. *Arch Neurol* 62, 1250-1255.
- Perlmutter, J.S., Mink, J.W., 2006. Deep brain stimulation. *Annu Rev Neurosci* 29, 229-257.

- Reimann, M.W., Anastassiou, C.A., Perin, R., Hill, S.L., Markram, H., Koch, C., 2013. A biophysically detailed model of neocortical local field potentials predicts the critical role of active membrane currents. *Neuron* 79, 375-390.
- Sugiyama, K., Nozaki, T., Asakawa, T., Koizumi, S., Saitoh, O., Namba, H., 2015. The present indication and future of deep brain stimulation. *Neurol Med Chir (Tokyo)* 55, 416-421.
- Taylor, D.M., Tillery, S.I., Schwartz, A.B., 2002. Direct cortical control of 3D neuroprosthetic devices. *Science* 296, 1829-1832.
- van Dijk, K.J., Verhagen, R., Chaturvedi, A., McIntyre, C.C., Bour, L.J., Heida, C., Veltink, P.H., 2015. A novel lead design enables selective deep brain stimulation of neural populations in the subthalamic region. *J Neural Eng* 12, 046003.
- Vetter, R.J., Williams, J.C., Hetke, J.F., Nunamaker, E.A., Kipke, D.R., 2004. Chronic neural recording using silicon-substrate microelectrode arrays implanted in cerebral cortex. *IEEE Trans Biomed Eng* 51, 896-904.
- Vitek, J.L., 2002. Mechanisms of deep brain stimulation: excitation or inhibition. *Mov Disord* 17 Suppl 3, S69-72.
- Vitek, J.L., 2008. Deep brain stimulation: how does it work? *Cleveland Clinic journal of medicine* 75 Suppl 2, 65.
- Wakana, S., Jiang, H., Nagae-Poetscher, L.M., van Zijl, P.C., Mori, S., 2004. Fiber tract-based atlas of human white matter anatomy. *Radiology* 230, 77-87.
- Williams, J.C., Rennaker, R.L., Kipke, D.R., 1999. Long-term neural recording characteristics of wire microelectrode arrays implanted in cerebral cortex. *Brain Res Brain Res Protoc* 4, 303-313.
- Zitella, L.M., Mohsenian, K., Pahwa, M., Gloeckner, C., Johnson, M.D., 2013. Computational modeling of pedunculopontine nucleus deep brain stimulation. *J Neural Eng* 10, 045005.
- Zitella, L.M., Teplitzky, B.A., Yager, P., Hudson, H.M., Brintz, K., Duchin, Y., Harel, N., Vitek, J.L., Baker, K.B., Johnson, M.D., 2015. Subject-specific computational modeling of DBS in the PPTg area. *Front Comput Neurosci* 9, 93.

Chapter 2

Atlas-Independent, N-of-1 Tissue Activation Modeling to Map the Optimal Location of Subthalamic Deep Brain Stimulation for Parkinson Disease

Abstract

Deep brain stimulation (DBS) of the subthalamic nucleus (STN) is an established surgical treatment for the motor symptoms of Parkinson disease (PD). Motor outcomes after DBS can vary considerably from one patient to another and depend strongly on where stimulation is applied in the brain. The objective of this retrospective study was to map the optimal location of STN DBS for PD using an atlas-independent, n-of-1 tissue activation modeling approach and to assess the relationship between the therapeutic volume of tissue activated (VTA) and motor improvement.

The stimulation-induced electric field for 40 PD patients treated with bilateral STN DBS was modeled using finite element analysis. Neurostimulation models were tailored to each patient, incorporating their individual STN anatomy, DBS lead position and orientation, anisotropic brain tissue conductivity, and clinical stimulation settings. A voxel-based analysis of the VTAs was used to map the optimal location of stimulation. The amount of stimulation in specific regions relative to the STN was measured and compared between patients with optimal and sub-optimal stimulation, as determined by their motor improvement scores and VTA. The relationship between VTA location and motor outcome was assessed using correlation analysis.

Patient variability in terms of STN anatomy, active contact position, and VTA location and a simplified VTA modeling approach were also evaluated.

Tissue activation modeling mapped the optimal location of stimulation to a region lateral, posterior, and dorsal to the STN centroid. This region overlapped with the STN and extended beyond its boundary towards the caudal zona incerta (cZI). VTA location and active contact position differed significantly between patients with optimal and sub-optimal stimulation in the dorsal-ventral and anterior-posterior directions. There were significant linear relationships between the amount of dorsal and posterior stimulation, as measured by the VTA, and motor improvement. These relationships were more robust than those between active contact position and motor improvement. There was high variability in STN anatomy, active contact position, and VTA location across patients. Spherical VTA modeling was unable to reproduce these results and tended to overestimate the size of the VTA.

Accurate characterization of the spread of stimulation in the brain is important for optimizing STN DBS for PD. High variability in neuroanatomy, stimulation location, and motor improvement across patients highlights the need for n-of-1 modeling techniques. This study mapped the optimal location of stimulation to the dorsolateral border of the STN, in the posterior half of the nucleus. Therapeutic stimulation spread noticeably more in the dorsal direction, providing additional evidence for cZI as an important DBS target. The atlas-independent, n-of-1 tissue activation modeling approach presented in this study can be used to develop and evaluate stimulation strategies to improve clinical outcome on an individual basis.

Introduction

Deep brain stimulation (DBS) of the subthalamic nucleus (STN) is an established surgical treatment for the motor symptoms of Parkinson disease (PD) in patients who no longer respond

well to medication (Benabid et al., 2009; Okun, 2012). The treatment involves implanting electrodes in the subthalamic region of the brain and then applying high-frequency electrical stimulation to said region (Collins et al., 2010). Despite the proven clinical effectiveness of DBS, motor improvement can vary considerably from one patient to another (Deuschl et al., 2006; Kleiner-Fisman et al., 2006; Okun et al., 2005). The underlying mechanism by which DBS provides its therapeutic effect is still uncertain (Ashkan et al., 2017; Deniau et al., 2010; Florence et al., 2016; Johnson et al., 2008; McIntyre and Hahn, 2010; McIntyre et al., 2004c; Montgomery and Gale, 2008; Vitek, 2002). However, it is widely accepted that DBS outcomes depend strongly on where stimulation is applied (Conrad et al., 2018; Maks et al., 2009; McIntyre et al., 2004b). Differences in the location of stimulation relative to the STN may, in part, explain the variability in motor improvement across patients.

The location of stimulation is typically defined by measuring the position of the active electrode contact relative to an anatomical reference point (Caire et al., 2013). The limitation of this approach is that it does not take into account the full spatial extent of stimulation. This could explain why there are conflicting findings regarding the relationship between active contact position and motor improvement (Bot et al., 2018; Koivu et al., 2018; McClelland et al., 2005; Nestor et al., 2014; Paek et al., 2008; Verhagen et al., 2019; Wodarg et al., 2012). When stimulation is applied by the active contact, an electric field is induced in the brain tissue that spreads outward in all directions. Due to the difficulty in measuring the stimulation field experimentally, modeling approaches have been used to characterize the spatial distribution of the DBS-induced electric field (Butson, 2012). From this, the theoretical amount of tissue directly affected by stimulation, termed the volume of tissue activated (VTA), can be calculated (Astrom et al., 2009; Butson et al., 2007). The VTA is a stimulation-dependent metric that can be

used to predict clinical outcomes (Avecillas-Chasin et al., 2019; Butson et al., 2006), optimize stimulation settings (Frankemolle et al., 2010; McIntyre et al., 2009), explore alternative surgical targets (Miocinovic et al., 2006; Zitella et al., 2013), and evaluate novel electrode designs (Butson and McIntyre, 2006; Howell et al., 2015; van Dijk et al., 2015). The utility of tissue activation modeling hinges on its ability to make accurate and clinically meaningful predictions. Substantial efforts have gone towards validating VTA predictions with experimental data (Miocinovic et al., 2009; Zitella et al., 2015).

Tissue activation modeling has become increasingly more complex over time. Neurostimulation models can now incorporate detailed anatomical information, heterogeneous and anisotropic tissue properties, explicit representation of the DBS lead and electrode-tissue interface, clinically determined stimulation settings, and biophysical neuron models (Chaturvedi et al., 2010; Gunalan et al., 2017; Gunalan et al., 2018; Howell and McIntyre, 2016). The primary motivation for each of these advancements has been a more accurate and patient-specific characterization of the spatial extent of stimulation. Previous studies have shown tissue anisotropy to be one of the most relevant factors impacting model prediction accuracy (Astrom et al., 2012; Howell and McIntyre, 2017; Ineichen et al., 2018; Schmidt and van Rienen, 2012; Vargas Cardona et al., 2017). However, tissue properties are typically derived from a brain atlas instead of individual patient data when creating tailored neurostimulation models (Butson et al., 2011). Since most brain atlases are based on a single subject, there is a limitation in how representative an atlas is to a patient population, especially one that is in a Parkinsonian state (Dickie et al., 2017; Nowacki et al., 2018).

The objective of this retrospective study was to map the optimal location of STN DBS for PD using an atlas-independent, n-of-1 tissue activation modeling approach and to assess the

relationship between the therapeutic VTA and motor improvement. The stimulation-induced electric field for 40 PD patients treated with bilateral STN DBS was modeled using finite element analysis. Neurostimulation models were tailored to each patient, incorporating their individual STN anatomy, DBS lead position and orientation, anisotropic brain tissue conductivity, and clinical stimulation settings. A voxel-based analysis of the VTAs was used to map the optimal location of stimulation. The amount of stimulation in specific regions relative to the STN was measured and compared between patients with optimal and sub-optimal stimulation, as determined by their motor improvement scores and VTA. The relationship between VTA location and motor outcome was assessed using correlation analysis. Patient variability in terms of STN anatomy, active contact position, and VTA location and a simplified VTA modeling approach were also evaluated to highlight the need for n-of-1 modeling approaches.

Methods

Patient Selection

For this study, patients were drawn from a clinical database of patients who received bilateral STN DBS for PD at the University of Michigan. Selection criteria were an established diagnosis of idiopathic PD and the availability of pre-operative MR and DT imaging, post-operative CT imaging, and clinical follow-up assessments at least six months after surgery (Chou et al., 2013). Patients with structural brain abnormalities on MR imaging, non-monopolar stimulation, or comorbid neuropsychiatric disorders, such as dementia and depression, were excluded. Forty patients were selected (Table 2-1), resulting in a total of 72 brain hemispheres for analysis. Informed consent was obtained from all patients in accordance with the policies of the Medical Institutional Review Board at the University of Michigan.

Table 2-1 Patient demographics and post-operative change in LEDD with DBS

	n	Mean	Standard deviation	Minimum	Maximum
Age at baseline [yr]	40	63.1	6.7	52.7	74.7
Age diagnosed [yr]	40	52.9	8.6	33	69
Disease duration at baseline [yr]	40	10.2	5.4	-0.7	22.8
Time to follow-up [mo]	40	9.6	5.6	6	24
LEDD (pre-operative) [mg/d]	40	1370.5	777.6	0	3342
LEDD (post-operative) [mg/d]	40	579.9	459.3	0	1746
LEDD reduction [%]	36	55.4	33.4	-50	100

n: 40 patients total (28 male and 12 female; 36 with medication); LEDD: L-DOPA equivalent daily dose.

Image Acquisition and Processing

Pre-operative 3-T MR images were acquired for each patient at their baseline evaluation. Post-operative CT images were acquired two to four weeks after surgery to allow intracranial air to resolve (Bentley et al., 2017). The MR and CT imaging protocols used have been previously reported (Patil et al., 2012). Pre-operative 3-T DT images were also acquired at baseline using a single-shot echo-planar imaging sequence combined with dS SENSE, a parallel imaging scheme used to decrease image distortion (Jaermann et al., 2004). Diffusion weighting was encoded along 15 independent orientations with a b-value of 800 mm²/s. DT imaging parameters included a 1 x 1 x 2 mm voxel size, 224 x 224 mm field-of-view, and reduction factor of 2.

MR and DT images were resampled using linear and cubic spline interpolation, respectively, to match the resolution of the CT images (Houshmand, 2015). MR images were transformed to Talairach space, where the anterior and posterior commissures lie on a straight horizontal line (Talairach and Tournoux, 1988). The midcommissural point (MCP) was defined as the origin, with positive x, y, and z coordinates corresponding to right, anterior, and dorsal (superior), respectively. CT and DT images were oriented to Talairach space via co-registration to the MR images using a normalized mutual information algorithm and manual refinement. All image processing was performed by the same individual to minimize co-registration variability using Analyze (12.0, AnalyzeDirect, Inc., Overland Park, KS, USA).

Clinical Evaluation

Part III of the Movement Disorders Society revision of the Unified Parkinson Disease Rating Scale (MDS-UPDRS III) was used to evaluate the severity of motor symptoms (Chou et al., 2013). Post-operative scores without medication for rigidity, bradykinesia, and tremor were used instead of baseline scores to isolate the stimulation-specific effects of DBS from those

associated with surgery or disease progression (Table 2-2). Scores were measured at least six months after surgery. Rigidity scores came from item 3.3, bradykinesia scores from items 3.4-3.8, and tremor scores from items 3.15 and 3.16. Overall motor scores were defined as the sum of the rigidity, bradykinesia, and tremor scores. Scores were lateralized to their respective hemispheres. Axial symptoms, such as speech and posture, were excluded from analysis. Motor improvement was defined as:

$$\text{improvement [\%]} = \frac{\text{score}_{\text{off med/off stim}} - \text{score}_{\text{off med/on stim}}}{\text{score}_{\text{off med/off stim}}} * 100$$

where $\text{score}_{\text{off med/off stim}}$ and $\text{score}_{\text{off med/on stim}}$ were the values of the post-operative scores without medication and stimulation and without medication and with stimulation, respectively. The stimulation amplitude at the electrode contact that maximized therapeutic effect and minimized side effects, as determined by a movement disorders neurologist (K.L.C.) during monopolar review, was recorded (Table 2-3).

Table 2-2 Post-operative change in lateralized MDS-UPDRS III scores with DBS

	n	Mean	Standard deviation	Minimum	Maximum
Rigidity score (off med/off stim)	72	2.4	1.9	0	8
Rigidity score (off med/on stim)	72	1.2	1.7	0	8
Rigidity improvement [%]	58	56.2	43.8	-50	100
Bradykinesia score (off med/off stim)	72	9.2	4.0	1	17
Bradykinesia score (off med/on stim)	72	6.2	4.2	0	17
Bradykinesia improvement [%]	72	36.9	41.3	-166.7	100
Tremor score (off med/off stim)	72	1.3	2.1	0	8
Tremor score (off med/on stim)	72	0.3	0.9	0	6
Tremor improvement [%]	29	80.0	37.1	0	100
Overall motor score (off med/off stim)	72	12.9	5.7	2	26
Overall motor score (off med/on stim)	72	7.7	5.3	0	25
Overall motor improvement [%]	72	39.9	44.6	-233.3	100

n: 72 brain hemispheres total (37 left and 35 right; 58 with rigidity, 72 with bradykinesia, and 29 with tremor); overall motor score: sum of rigidity, bradykinesia, and tremor scores.

Table 2-3 Clinical DBS settings, electrode impedance, and modeled VTA

	n	Mean	Standard deviation	Minimum	Maximum
Stimulation amplitude [V]	72	2.7	0.6	1.5	4.2
Electrode impedance [Ω]	71	1225.8	279.4	441	1902
VTA [mm ³]	72	68.6	22.9	30.1	124.7

Stimulation frequency and pulse width were set to 130 Hz and 60 μ s, respectively, for the majority of patients. n: 72 brain hemispheres total (37 left and 35 right); VTA: volume of tissue activated.

Atlas-Independent, N-of-1 Tissue Activation Modeling

Multi-step, electric field modeling techniques using atlas-based anatomical nuclei and tissue properties have been previously developed (Astrom et al., 2009; Butson et al., 2007). In this study, an atlas-independent, n-of-1 tissue activation modeling approach building from these previous works was designed to increase the accuracy of VTA modeling on a patient-by-patient basis (Figure 2-1). The n-of-1 modeling approach is described below.

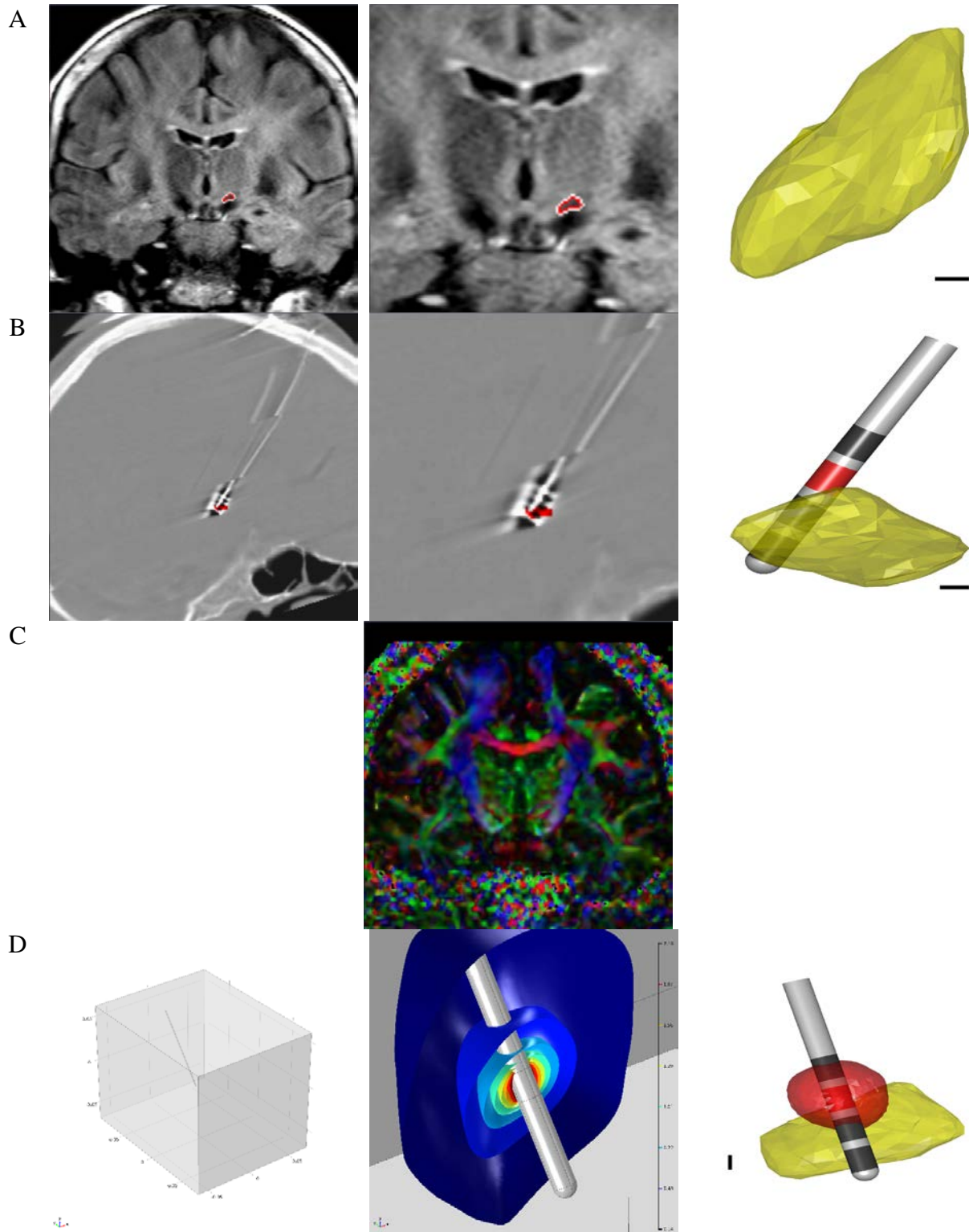


Figure 2-1 Atlas-independent, n-of-1 tissue activation modeling approach. (A) STN segmentation. Left: coronal MR image from one patient showing the left (outlined in red) and right STN. Center: zoomed in version. Right: left STN in MATLAB after STN segmentation. (B) Electrode contact localization. Left: sagittal CT image showing the electrode contacts (shown in black) of the left DBS lead. Left STN mask is shown in red. Center: zoomed in version. Right:

left STN and DBS lead in MATLAB after electrode contact localization. (C) Anisotropic brain tissue conductivity estimation. Coronal DT image showing the calculated eigenvector color map. Red, green, and blue correspond to the x, y, and z direction, respectively. (D) Finite element analysis. Left: bulk brain tissue and left DBS lead geometry in COMSOL. Center: DBS-induced potential distribution around the active contact. Colors correspond to different isolevels in V. Positive x, y, and z correspond to the right hemisphere, anterior direction, and dorsal direction, respectively. Right: left STN, DBS lead, and VTA, defined by the thresholded electric field norm, in MATLAB after finite element analysis. The STN is shown in yellow, active contact and VTA are shown in red, and inactive contacts are shown in dark gray. Scale bars equal 1 mm.

STN Segmentation

3D anatomical models of the STNs were created for each patient from their MR imaging (72 STNs total). STNs were manually traced from coronal slices using Analyze. Visualization of the STN was optimized by maximizing contrast between it and substantia nigra pars reticulata (Conrad et al., 2018; Houshmand et al., 2014; Patil et al., 2012). All STNs were traced by the same individual (K.A.M.) and validated by the neurosurgeon who performed the DBS surgeries (P.G.P.) to minimize segmentation variability. STN traces were then exported to MATLAB (R2018b, The MathWorks, Inc., Natick, MA, USA) for analysis.

Electrode Contact Localization

All patients were implanted with quadripolar DBS leads (model 3389, Medtronic, Inc., Minneapolis, MN, USA). Electrode contacts were localized in the brain of each patient from their CT imaging (288 electrodes and 72 active contacts total). Contact coordinates were measured from sagittal slices using Analyze. Visualization of the electrode contacts was optimized via CT windowing (Conrad et al., 2018; Patil et al., 2012). All electrode contacts were measured by the same individual to minimize localization variability. Contact coordinates were then exported to MATLAB for analysis.

Anisotropic Brain Tissue Conductivity Estimation

The anisotropic electrical conductivity of the brain tissue was estimated for each patient from their DT imaging (40 tensor fields total) (Tuch et al., 2001). Diffusion eigenvalue and eigenvector maps were calculated using Analyze and then exported to MATLAB, where they were converted into 3D conductivity tensors on a per-voxel basis (Houshmand, 2015). Conductivity tensor fields were then exported to COMSOL Multiphysics (5.2, COMSOL, Inc., Burlington, MA, USA) for finite element analysis.

Finite Element Analysis

3D finite element models (FEMs) incorporating individual brain anatomy, DBS lead position and orientation, anisotropic tissue conductivity, and clinical stimulation settings were created for each hemisphere of each patient (72 FEMs total) to calculate the spatial distribution of the DBS-induced electric field and estimate the therapeutic VTA (Astrom et al., 2009; Butson et al., 2007). The bulk brain tissue was modeled as a block surrounding the DBS lead, which was modeled as a Medtronic 3389 lead. The block of tissue had a width, length, and depth equal to that of the patient's brain, as measured on MR imaging, and the cylindrical lead had a contact length of 1.5 mm, contact spacing of 0.5 mm, and electrode diameter of 1.27 mm. The DBS lead was translated and rotated such that the electrode contacts best matched the measured contact coordinates. The bulk tissue domain was assigned the DT imaging-based anisotropic electrical conductivities by linearly interpolating the conductivity tensors onto the mesh. The remaining domains, contact and insulation, were assigned isotropic conductivities of $1.42e^7$ S/m and $1e^{-13}$ S/m, respectively (Kent and Grill, 2014). Boundary conditions were defined for the electrode contacts and bulk tissue. An electric potential equal to the patient's therapeutic stimulation amplitude was applied to the surface of said patient's therapeutic electrode contact (active

contact) and ground was applied to the bottom surface of the bulk tissue (Pelot et al., 2018). The remaining electrode contacts were disabled. FEMs were then meshed, with finer meshing applied at and around the DBS lead. After testing for model convergence by modifying the mesh density, simulations were run to solve for the electric potential throughout the brain using the Poisson equation. All FEMs were electrostatic because the impedance of gray matter has been shown to be frequency-independent for clinically relevant stimulation frequencies (Logothetis et al., 2007). The VTA was defined by the electric field norm, thresholded at stimulation-specific activation levels derived from biophysical neuron models (Astrom et al., 2015). Simulations and VTA predictions were performed using COMSOL. VTAs were then exported to MATLAB, where their location relative to the STN was characterized for analysis.

VTA Mapping

N-of-1 VTAs were placed into a common coordinate space (single hemisphere) by flipping, translating, scaling, and rotating each patient-specific STN to the median STN (based on volume) and then applying the associated transformations to each VTA. The number of VTAs at each position (voxel) was calculated to identify the region of greatest VTA overlap. A clinical score reflecting the motor outcomes of each patient (percent improvement) was then assigned to the voxels comprising each VTA (Akram et al., 2017; Butson et al., 2011; Haegelen et al., 2018). The mean score was calculated at each voxel to identify the optimal location of stimulation. VTAs were mapped for overall motor improvement as well as improvement in rigidity, bradykinesia, and tremor. If patients did not have a particular motor symptom, then their VTAs were excluded from the symptom-specific analysis.

Optimality of Stimulation

Despite some patients having similar motor outcomes, the size and shape of their n-of-1 VTAs often varied. Assuming an optimal location of stimulation existed, it was reasoned that patients with active contacts near said location would require less stimulation (and in turn have smaller VTAs) to gain therapeutic benefit from DBS (Conrad et al., 2018). A measure of how optimal stimulation was, termed optimality of stimulation, was defined to differentiate patients with similar levels of motor improvement. This measure was the ratio of improvement to the VTA size. Patients with greater improvement and smaller VTAs were considered to have more optimal stimulation.

Statistical Analysis

Paired, two-sided Wilcoxon signed rank tests were used to determine if post-operative assessments with DBS ON differed significantly from those with DBS OFF. For VTA mapping, a bootstrap analysis was performed in which the clinical scores were randomly assigned to each VTA (and its associated voxels) prior to averaging to distinguish statistically significant voxel-score pairs. This process was repeated 1000 times to create a null distribution of mean scores at each voxel. A voxel-score pair was determined significant if the actual mean score at said voxel lay within the top five percent of the distribution. Two-sided Wilcoxon rank sum tests (equivalent to Mann-Whitney U-tests) were used to determine if stimulation location for patients with optimal stimulation differed significantly from that for patients with sub-optimal stimulation. Correlation analysis was used to determine if there was a significant linear relationship between stimulation location and the optimality of stimulation (ratio of motor improvement to the VTA size). Analysis was performed using MATLAB. Significance was determined at a p-value of less than 0.05.

Results

Patient Motor Outcome

Lateralized, post-operative overall motor, rigidity, bradykinesia, and tremor scores from the MDS-UPDRS III improved significantly with DBS ON; and pre-operative LEDD decreased significantly with DBS ($p < 0.001$, Wilcoxon signed rank test) (Figure 2-2). The overall motor score improved by 5.2 points (40.5%), while the rigidity, bradykinesia, and tremor scores improved by 1.2 points (51.5%), 3.0 points (32.3%), and 1.0 points (79.3%), respectively. LEDD decreased by 790.6 mg/d (57.7%).

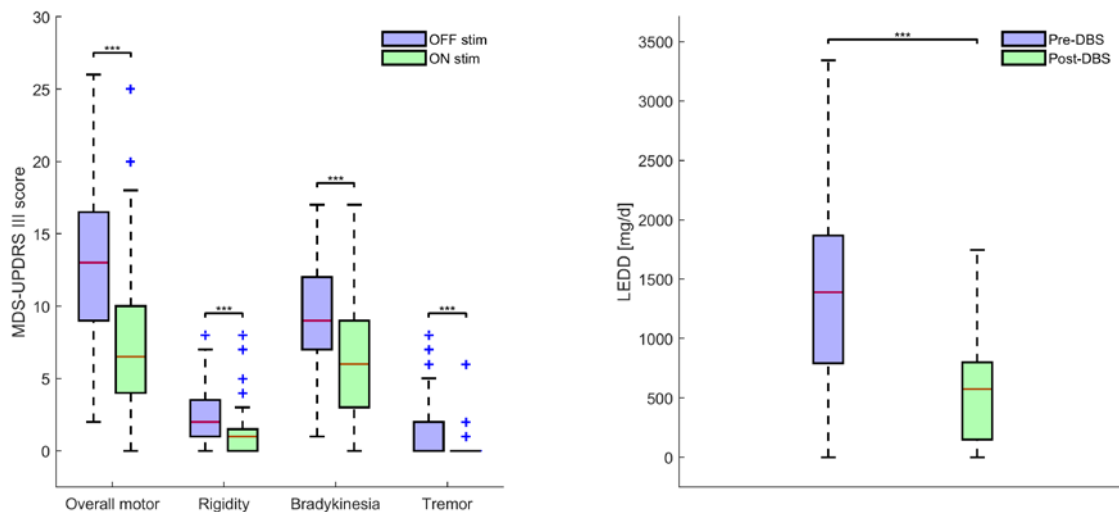


Figure 2-2 Lateralized, post-operative MDS-UPDRS III scores OFF and ON DBS, and pre- and post-operative LEDD. Left: overall motor, rigidity, bradykinesia, and tremor scores. Right: LEDD. *** $p < 0.001$, Wilcoxon signed rank test.

Optimal Location of Stimulation

For overall motor improvement, all n-of-1 VTAs were analyzed (Figure 2-3). The region of greatest VTA overlap was located 0.20 mm medial and 0.80 mm posterior to the STN centroid (-0.20, -0.80, 0). In contrast, the optimal location of stimulation was mapped to a region lateral,

posterior, and dorsal to the STN centroid. This region overlapped with the STN and extended beyond its boundary in each direction.

For rigidity, bradykinesia, and tremor improvement, 58/72, 72/72, and 29/72 VTAs were analyzed, respectively (Figure 2-4, Figure 2-5, and Figure 2-6). The regions of greatest VTA overlap were the same as or similar to that identified for overall motor improvement (rigidity: -0.20, -0.80, 0; bradykinesia: -0.20, -0.80, 0; tremor: -0.33, -0.66, -0.35). Likewise, the optimal locations of stimulation were mapped to regions lateral, posterior, and dorsal to the STN centroid irrespective of the motor symptom. These regions also overlapped with the STN and extended beyond its boundary in each direction.

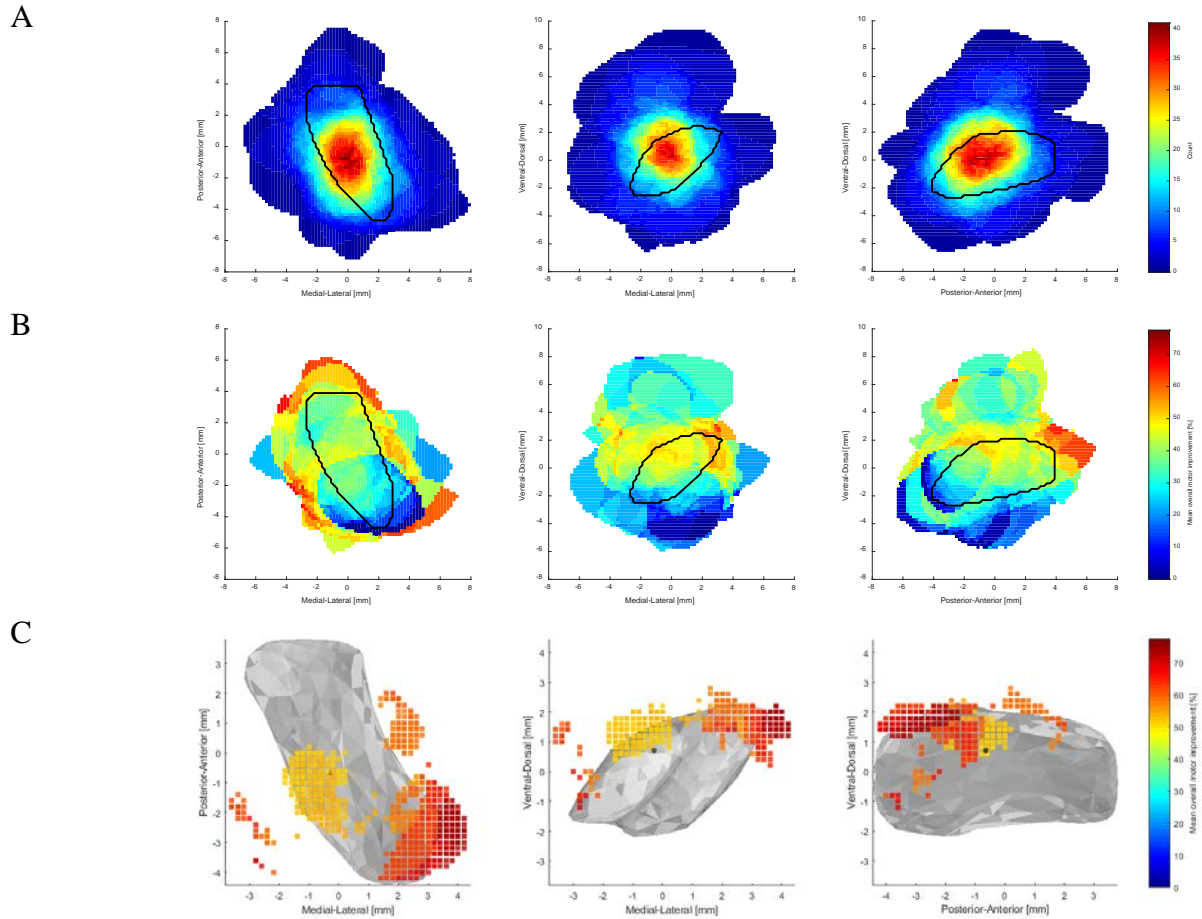


Figure 2-3 VTA mapping for overall motor improvement. (A) Map of the number of overlapping VTAs. (B) Map of mean overall motor improvement. Slices are at the STN centroid (origin). The median STN (based on volume) is shown as a black outline. (C) 3D map of mean overall motor improvement at statistically significant voxels (determined via bootstrap analysis). The mean active contact position is shown as a black circle and the median STN is shown as a gray surface. Axial, coronal, and sagittal views are shown.

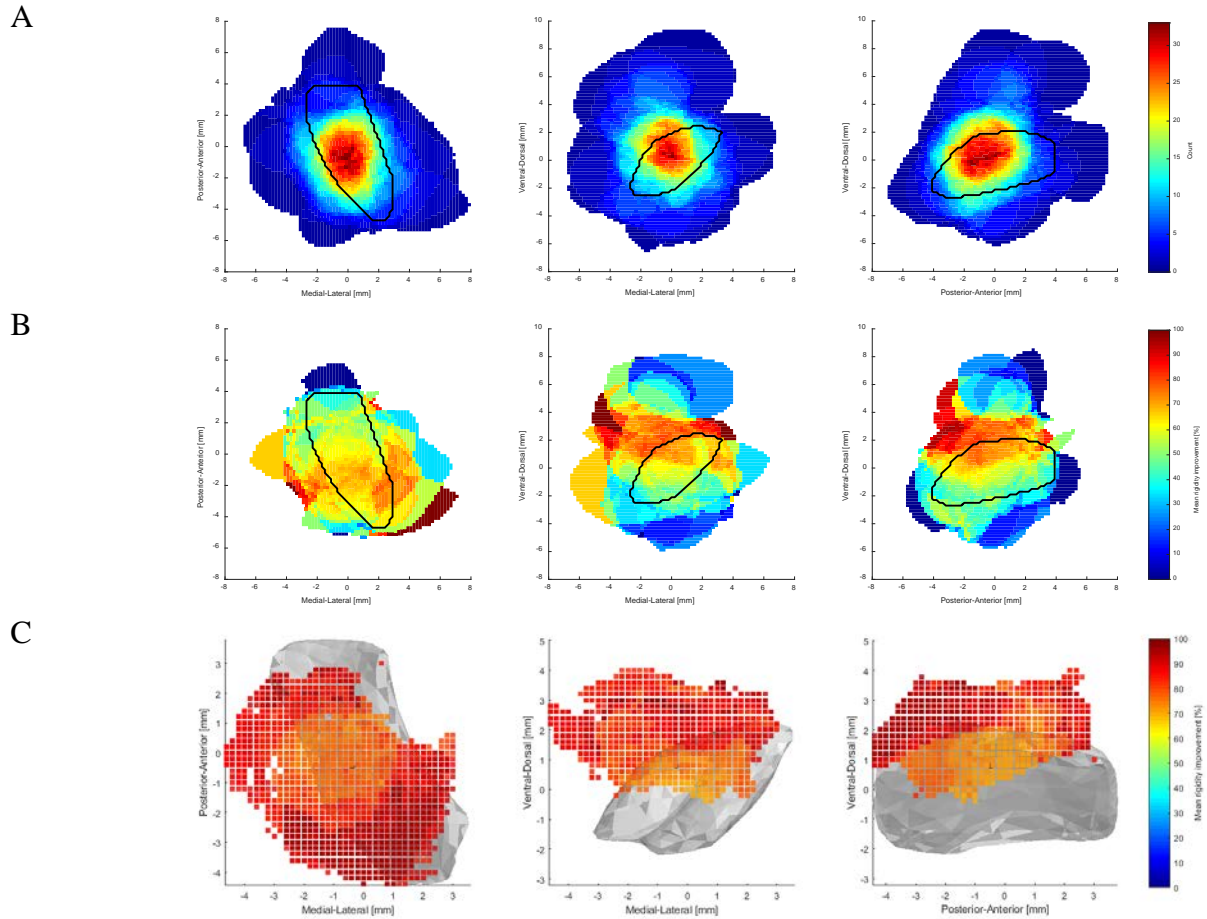


Figure 2-4 VTA mapping for rigidity improvement. (A) Map of the number of overlapping VTAs. (B) Map of mean rigidity improvement. Slices are at the STN centroid (origin). The median STN (based on volume) is shown as a black outline. (C) 3D map of mean rigidity improvement at statistically significant voxels (determined via bootstrap analysis). The mean active contact position is shown as a black circle and the median STN is shown as a gray surface. Axial, coronal, and sagittal views are shown.

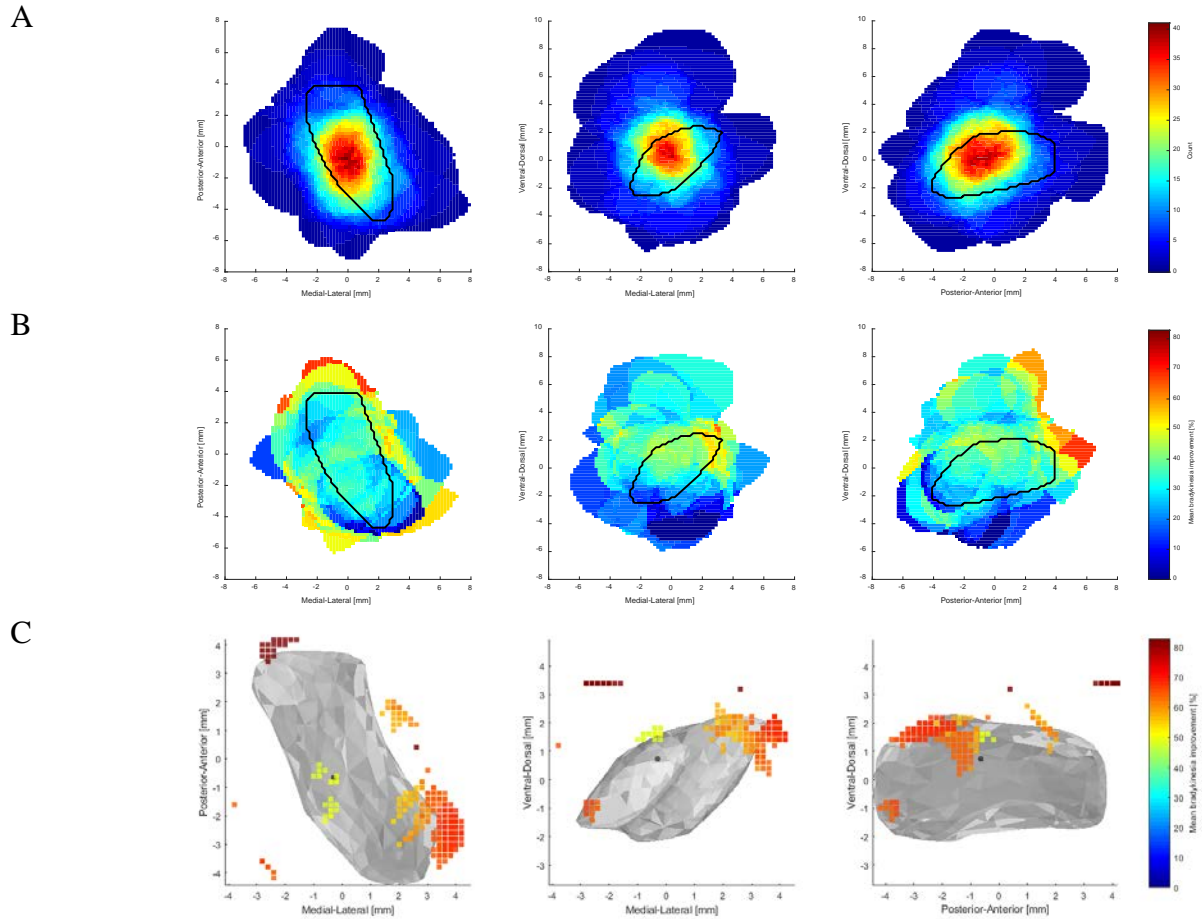


Figure 2-5 VTA mapping for bradykinesia improvement. (A) Map of the number of overlapping VTAs. (B) Map of mean bradykinesia improvement. Slices are at the STN centroid (origin). The median STN (based on volume) is shown as a black outline. (C) 3D map of mean bradykinesia improvement at statistically significant voxels (determined via bootstrap analysis). The mean active contact position is shown as a black circle and the median STN is shown as a gray surface. Axial, coronal, and sagittal views are shown.

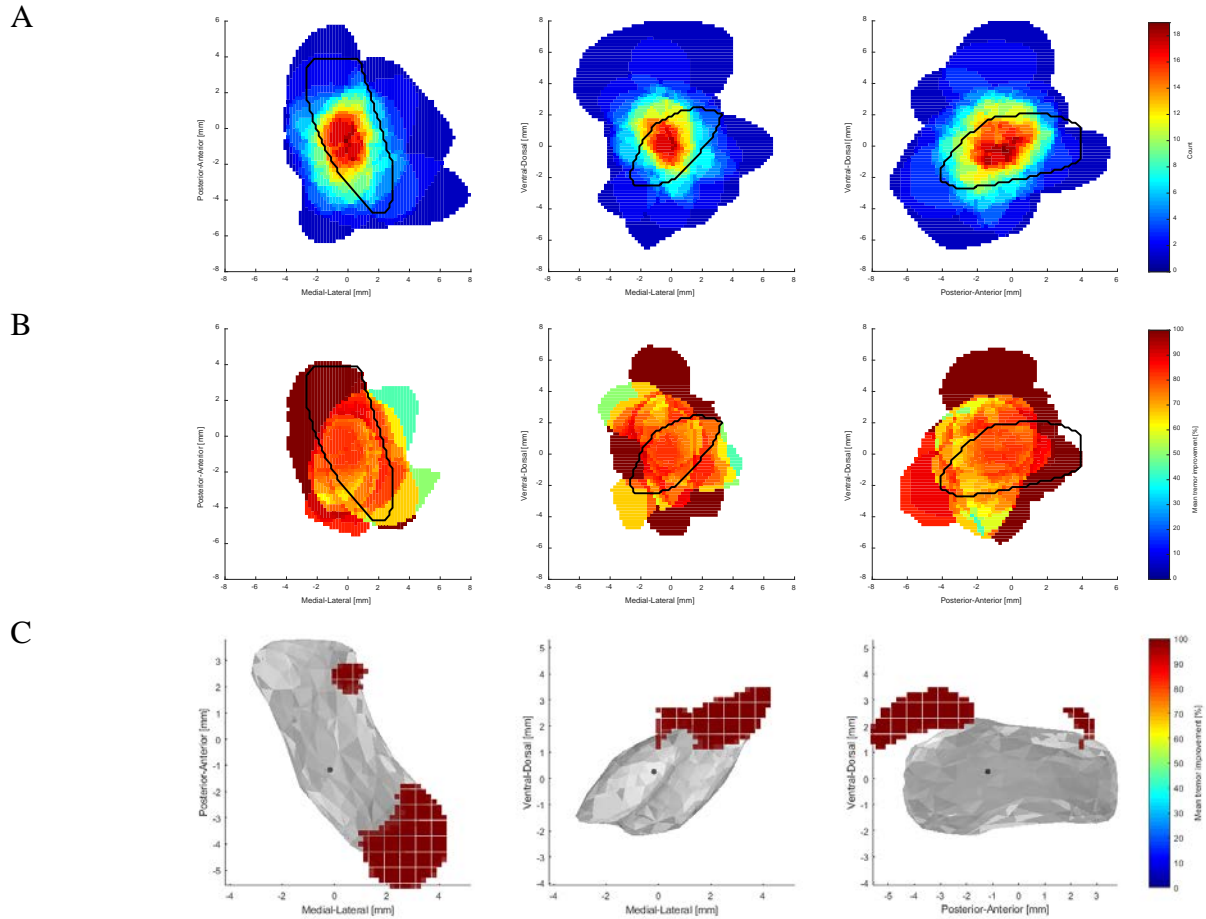


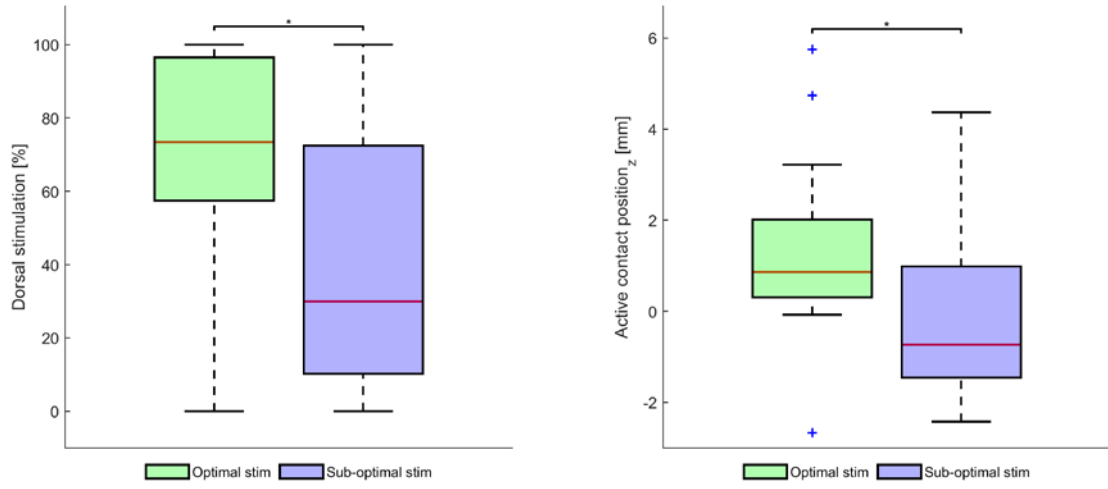
Figure 2-6 VTA mapping for tremor improvement. (A) Map of the number of overlapping VTAs. (B) Map of mean tremor improvement. Slices are at the STN centroid (origin). The median STN (based on volume) is shown as a black outline. (C) 3D map of mean tremor improvement at statistically significant voxels (determined via bootstrap analysis). The mean active contact position is shown as a black circle and the median STN is shown as a gray surface. Axial, coronal, and sagittal views are shown.

Difference in Stimulation Location between Optimal and Sub-Optimal Stimulation

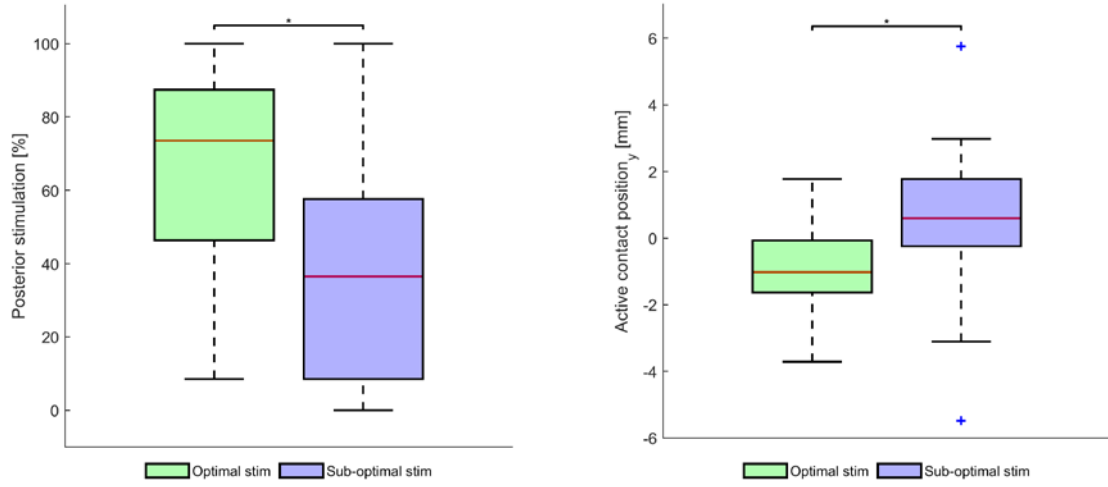
Patients were ranked by their optimality of stimulation (ratio of motor improvement to the VTA size) to determine if those with optimal and sub-optimal stimulation differed in terms of VTA location and active contact position (Figure 2-7). The top and bottom 25% of patients were placed into optimal and sub-optimal stimulation groups, respectively. For overall motor and bradykinesia, patients with optimal stimulation had significantly more dorsal stimulation and significantly more dorsal active contacts (relative to the STN centroid) than those with sub-

optimal stimulation ($p < 0.05$, Mann-Whitney U-test). For rigidity, patients with optimal stimulation had significantly more posterior stimulation and significantly more posterior active contacts than those with sub-optimal stimulation ($p < 0.05$, Mann-Whitney U-test). These findings were consistent with the VTA mapping results above.

A



B



C

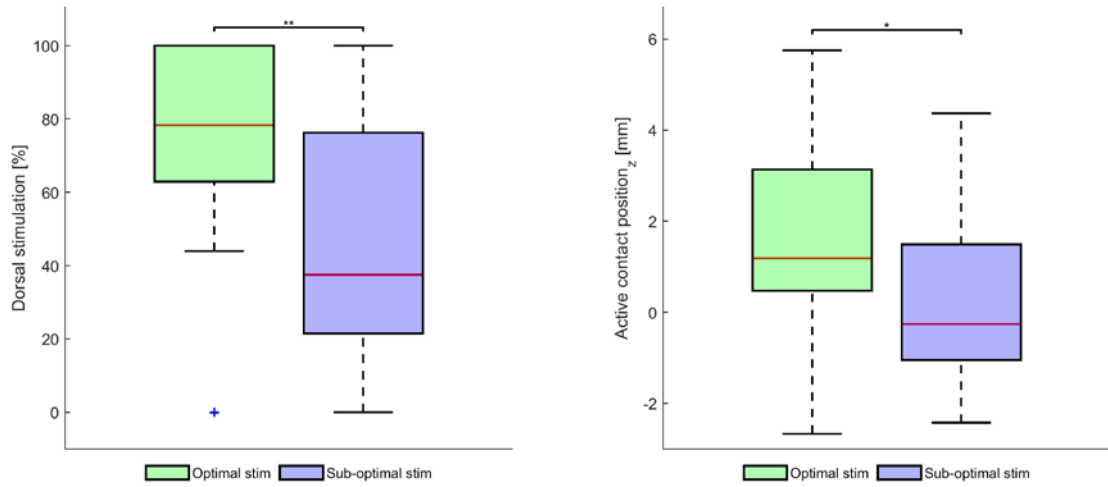
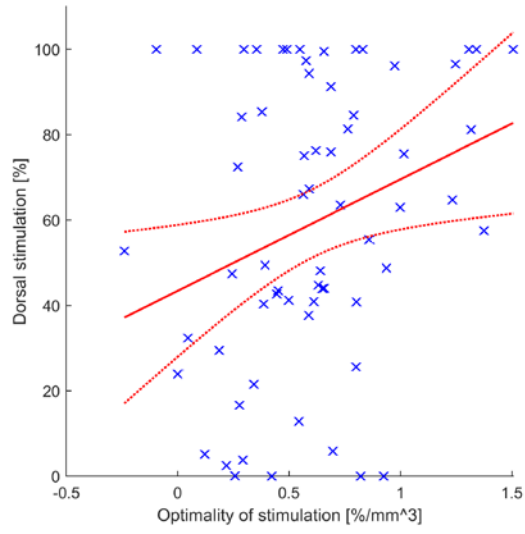


Figure 2-7 Difference in stimulation location between patients with optimal and sub-optimal stimulation. (A) Overall motor. Patients with optimal stimulation (top 25%) had significantly more dorsal stimulation and significantly more dorsal active contacts (relative to the STN centroid) than those with sub-optimal stimulation (bottom 25%). (B) Rigidity. Patients with optimal stimulation had significantly more posterior stimulation and significantly more posterior active contacts than those with sub-optimal stimulation. (C) Bradykinesia. Patients with optimal stimulation had significantly more dorsal stimulation and significantly more dorsal active contacts than those with sub-optimal stimulation. * $p < 0.05$ and ** $p < 0.01$, Mann-Whitney U-test.

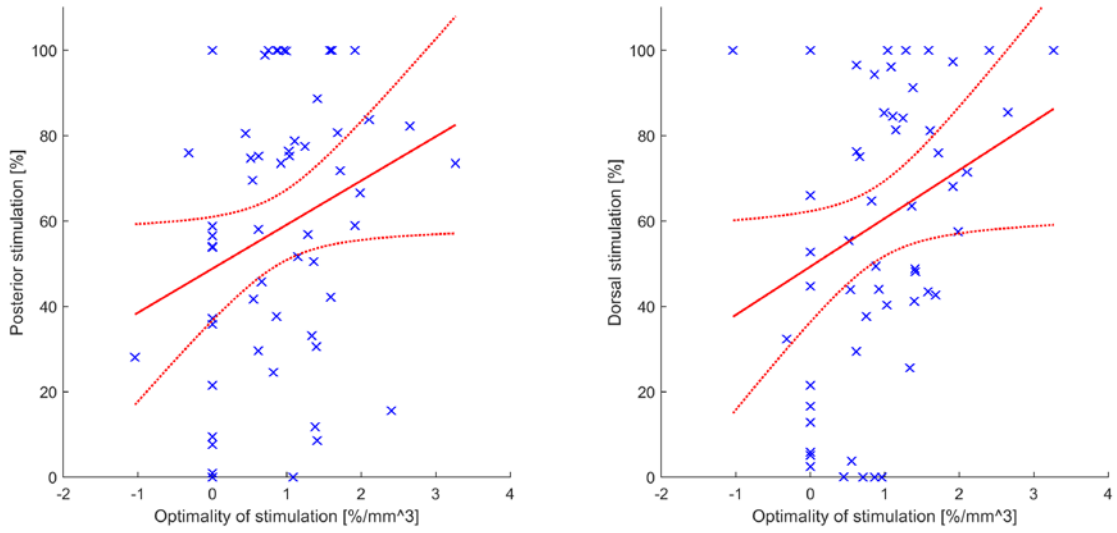
Relationship between Stimulation Location and Motor Improvement

Correlation analysis was used to assess the relationship between stimulation location and the optimality of stimulation (ratio of motor improvement to the VTA size) (Figure 2-8). For overall motor outcomes, there was a statistically significant linear relationship between the amount of dorsal stimulation (as measured by the VTA) and the optimality of stimulation ($r = 0.29$, $p = 0.02$). For rigidity, there were significant relationships between the amounts of posterior and dorsal stimulation and the optimality of stimulation (posterior: $r = 0.26$, $p = 0.046$; dorsal: $r = 0.27$, $p = 0.04$). For bradykinesia, there was a significant relationship between active contact position in the lateral-medial direction and the optimality of stimulation ($r = 0.28$, $p = 0.02$). These findings were also consistent with the VTA mapping results above. For tremor, there was no relationship between stimulation location and the optimality of stimulation. Compared to active contact position, VTA location had more robust relationships with motor improvement.

A



B



C

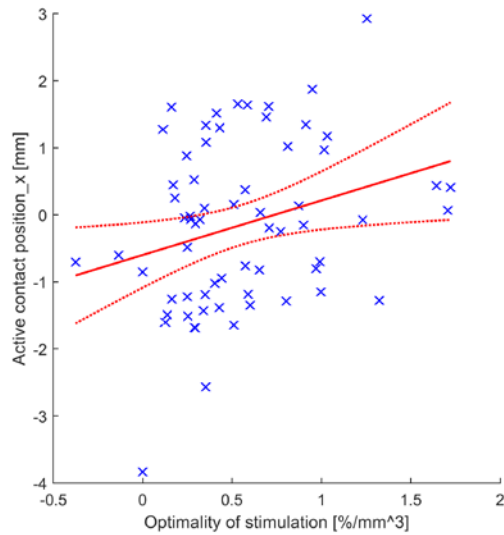


Figure 2-8 Relationship between stimulation location and motor improvement. (A) Overall motor. Linear regression model of the amount of dorsal stimulation (as measured by the VTA) and the optimality of stimulation (ratio of motor improvement to the VTA size). (B) Rigidity. Linear regression models of the amounts of posterior and dorsal stimulation and the optimality of stimulation. (C) Bradykinesia. Linear regression model of active contact position in the lateral-medial direction and the optimality of stimulation. Legend: blue x = data, solid red line = fit, and dashed red line = confidence bounds. $p < 0.05$, Pearson's linear correlation coefficient.

Patient Variability in STN Anatomy and Stimulation Location

High variability in STN anatomy (location and size) and stimulation location (active contact position and VTA location) was observed across patients (Figure 2-9). STN location was characterized by its centroid position relative to the MCP; and STN size was characterized by its width, length, depth, and volume (Figure 2-10). The STN centroid was located 11.13 ± 1.39 mm lateral (mean \pm standard deviation), 0.92 ± 2.59 mm posterior, and 3.24 ± 1.22 mm ventral to the MCP. STN width, length, depth, and volume were 7.91 ± 1.67 mm, 8.56 ± 1.45 mm, 5.19 ± 1.12 mm, and 80.9 ± 31.3 mm³, respectively.

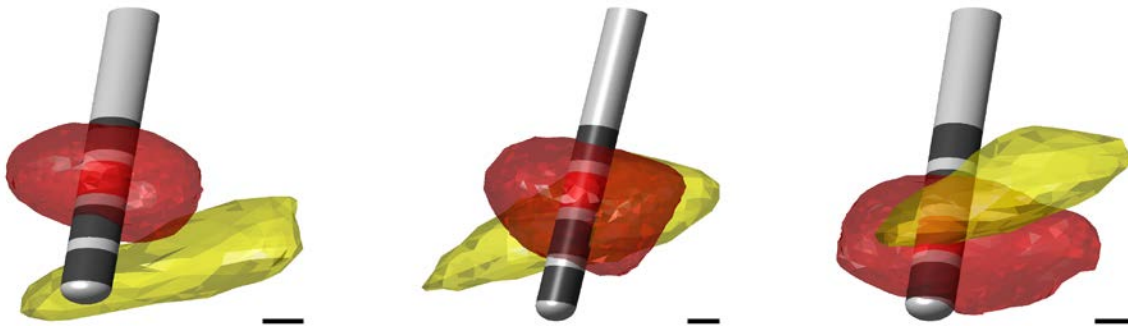


Figure 2-9 Variability in STN anatomy and stimulation location across patients. 3D models of the patient-specific STN, DBS lead, and VTA for three patients. The STN is shown in yellow, active contact and VTA are shown in red, and inactive contacts are shown in dark gray. Coronal views are shown. Scale bars equal 1 mm.

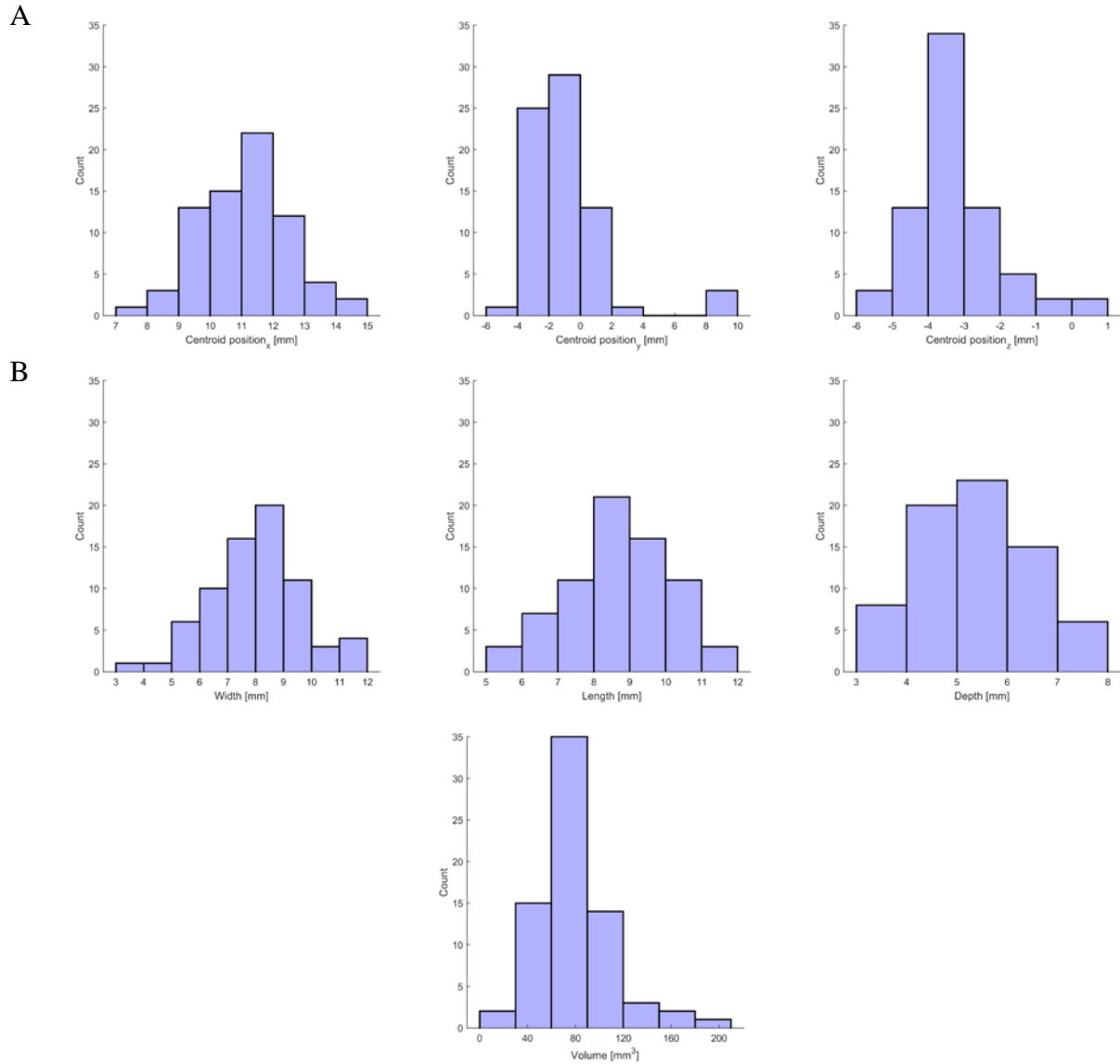


Figure 2-10 Variability in STN location and size across patients. (A) Histograms of STN centroid position (relative to the MCP) in the lateral-medial, anterior-posterior, and dorsal-ventral directions. Positive x, y, and z correspond to the lateral, anterior, and dorsal directions, respectively. (B) Histograms of STN width, length, depth, and volume.

Active contact location was characterized by its position relative to the STN centroid (Figure 2-11). The mean active contact was located 0.21 ± 1.35 mm medial, 0.63 ± 1.93 mm posterior, and 0.79 ± 1.99 mm dorsal to the STN centroid. Active contacts were distributed quite evenly around the STN centroid in all directions.

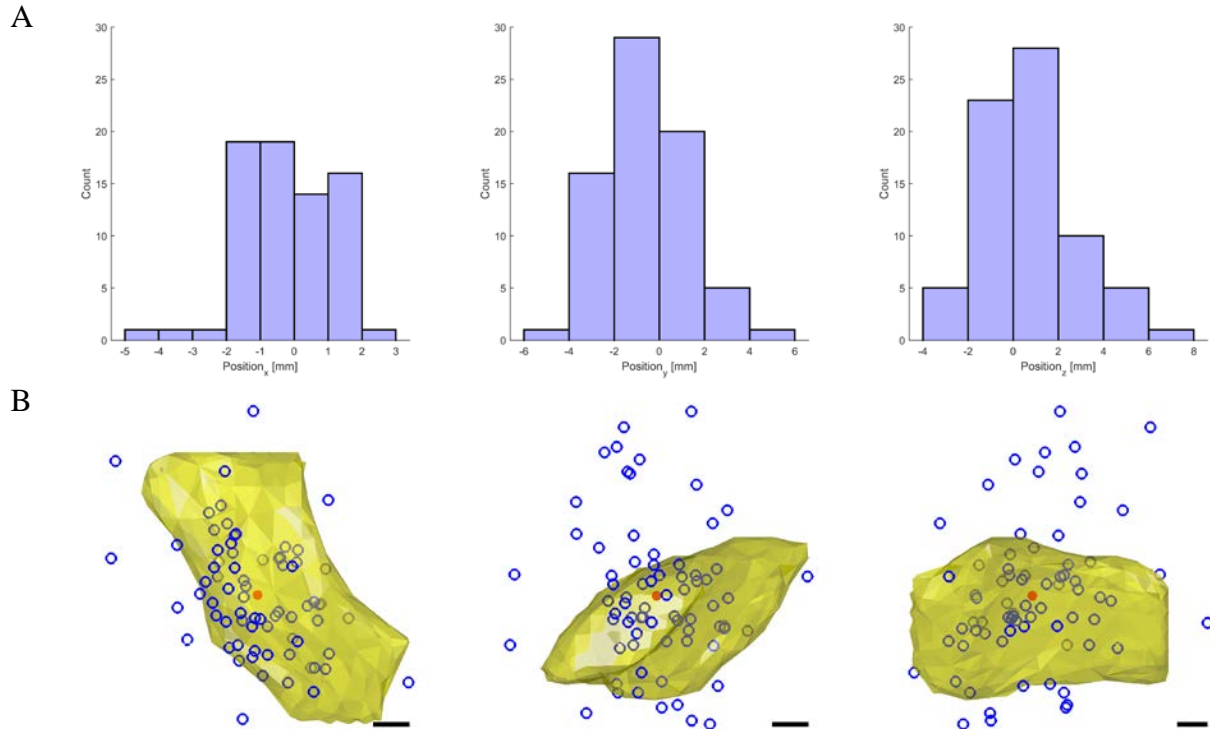


Figure 2-11 Variability in active contact position across patients. (A) Histograms of active contact position (relative to the STN centroid) in the lateral-medial, anterior-posterior, and dorsal-ventral directions. Positive x, y, and z correspond to the lateral, anterior, and dorsal directions, respectively. (B) Scatter plots of active contact position for 72 implants (open, blue circles; normalized by STN dimensions). The mean active contact position is shown as a filled, red circle and the median STN (based on volume) is shown in yellow. Axial, coronal, and sagittal views are shown. Scale bars equal 1 mm.

VTA location was characterized by the percentage of the VTA lateral, posterior, and dorsal to the STN centroid (lateral, posterior, and dorsal stimulation, respectively) and the percentage of the VTA outside of the STN (external stimulation) (Figure 2-12). $46.3 \pm 28.1\%$ of the VTA was lateral, $60.9 \pm 33.1\%$ was posterior, and $59.2 \pm 33.0\%$ was dorsal to the STN centroid. $77.7 \pm 16.3\%$ of the VTA was outside of the STN. VTAs were distributed quite evenly around the STN centroid in the lateral-medial direction. However, VTAs spread noticeably more posterior and dorsal than anterior and ventral, respectively (in contrast to active contact position). In all but two cases, over half of the VTA spread beyond the STN boundary.

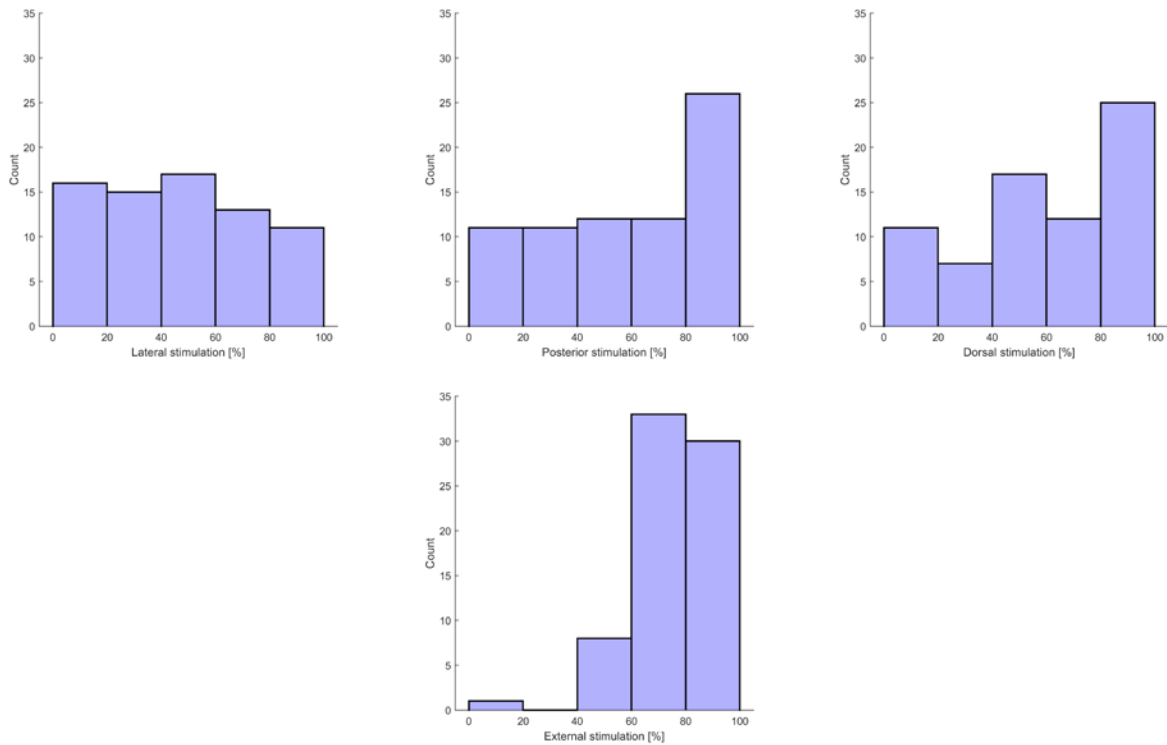


Figure 2-12 Variability in VTA location across patients. Histograms of VTA location (top row: relative to the STN centroid, bottom row: relative to the STN boundary) in the lateral-medial, anterior-posterior, and dorsal-ventral directions.

Discussion

STN DBS is an established surgical treatment for the motor symptoms of PD. Despite the proven clinical effectiveness of DBS, motor improvement can vary considerably from one patient to another. A possible explanation for this variability are differences in where stimulation is applied in the subthalamic region. Previous studies have highlighted the need for a more detailed identification of stimulation location relative to DBS targets, one that goes beyond simple active contact position (Caire et al., 2013; Nestor et al., 2014). In this study, an atlas-independent, n-of-1 tissue activation modeling approach was used to characterize the spatial extent of stimulation, termed the VTA, in 40 patients with PD who received bilateral STN DBS. Individual MR, CT, and DT imaging data were used to build each patient-specific neurostimulation model, and individual clinical scores from the MDS-UPDRS III were assigned

to the VTA predictions to assess the effectiveness of each stimulation zone. To the best of our knowledge, this study is the first to use a truly n-of-1, atlas-independent VTA modeling approach to identify the optimal location of STN DBS for PD at this large a patient group.

Optimal Location of Stimulation

For overall motor improvement, mapping the individual VTAs to a common coordinate space revealed the optimal location of stimulation to be in a region lateral, posterior, and dorsal to the STN centroid. This finding is consistent with previous studies attempting to identify the optimal stimulation site for STN DBS (Akram et al., 2017; Butson et al., 2011; Conrad et al., 2018; Haegelen et al., 2018; Herzog et al., 2004; Maks et al., 2009; Pollo et al., 2007; Voges et al., 2002; Yokoyama et al., 2006). The optimal location of stimulation overlapped with the STN and extended outside its borders in each direction. In contrast, the mean active contact position lay firmly within the dorsal half of the STN. Therapeutic stimulation consistently spread beyond the STN, as confirmed by calculating the percentage of the VTA external to the STN. In 70/72 cases, over half of the total VTA lay outside the STN. These findings suggest that the optimal location of stimulation lies at the dorsolateral border of the STN, in the posterior half of the nucleus. This location varied little when motor symptoms were analyzed individually, suggesting that optimal stimulation sites for rigidity, bradykinesia, and tremor may not be unique. The optimal location of stimulation was largest for rigidity and smallest for bradykinesia. This finding is consistent with a previous modeling study (Butson et al., 2011). The optimal stimulation site for STN DBS is still under debate (Plaha et al., 2006; Welter et al., 2014). Alternative DBS targets have been explored to better tailor treatment to the individual needs of PD patients (Anderson et al., 2017). These targets include the globus pallidus internus, ventral intermediate nucleus of the thalamus, and caudal zona incerta (cZI). The cZI, in particular, has

recently been suggested as an overall superior target (Blomstedt et al., 2012; Plaha et al., 2006). The optimal location of stimulation identified in this study includes the region where the cZI is located in addition to the motor subregion of the STN (Alkemade, 2013).

Difference in Stimulation Location between Optimal and Sub-Optimal Stimulation

As a way to validate the optimal location of stimulation identified from VTA mapping, stimulation location was compared between patients with optimal and sub-optimal stimulation. Patients were ranked according to how optimal their therapeutic stimulation was, termed the optimality of stimulation, and then separated into an optimal and sub-optimal stimulation group. The optimality of stimulation measure was defined as the ratio of motor improvement to the VTA size, such that patients with larger improvement and smaller VTAs were considered to have more optimal stimulation. The logic behind this measure was that patients with active contacts closer to some presumed optimal stimulation site would require less stimulation (and in turn have smaller VTAs) to gain therapeutic benefit from DBS (Conrad et al., 2018). Unlike for VTA mapping, measurements for this analysis were taken in the native space of each patient. Once patients were grouped, differences in VTA location and active contact position between the two groups were assessed. For overall motor and bradykinesia, patients with optimal stimulation had significantly more dorsal stimulation and significantly more dorsal active contacts (relative to the STN centroid) than those with sub-optimal stimulation ($p < 0.05$). For rigidity, patients with optimal stimulation had significantly more posterior stimulation and significantly more posterior active contacts than those with sub-optimal stimulation ($p < 0.05$). These findings suggest that the optimal location of stimulation lies dorsal and posterior to the STN centroid, which is consistent with the VTA mapping results. There were no significant differences in stimulation location between the two groups for tremor. This was likely due to the lower number

of tremor VTAs available and the fact that tremor improvement was the least sensitive motor outcome to stimulation location (tremor was completely alleviated by DBS in most patients regardless of the size of their VTA).

Relationship between Stimulation Location and Motor Improvement

There is conflicting evidence in the literature regarding the relationship between coordinate-based electrode location and DBS motor outcomes. Several studies have reported that electrode location can predict motor improvement (Bot et al., 2018; Verhagen et al., 2019), while others have reported that there is no significant correlation between the two variables (Koivu et al., 2018; McClelland et al., 2005; Nestor et al., 2014; Paek et al., 2008; Wodarg et al., 2012). Using individual STNs manually segmented from patient MR imaging (not an atlas STN warped to each patient), the position of the active contact relative to the STN centroid was measured in each hemisphere (if applicable). The STN centroid was chosen over the typically used MCP as the anatomical reference point to account for neuroanatomical variability across patients (Bot et al., 2018). A correlation analysis was then performed between active contact position and the optimality of stimulation. Bradykinesia was the only motor symptom with a significant relationship between the two variables ($p < 0.05$), where more lateral electrode contacts were correlated with more optimal stimulation. A key limitation of using active contact position to identify where stimulation is located is that it does not take into account the full spatial extent of stimulation (unlike the VTA), which varies based on the DBS settings and electrical properties of the brain. Consequently, the correlation analysis was repeated using VTA location instead of active contact position. For overall motor outcomes, there was a significant relationship between the amount of dorsal stimulation and the optimality of stimulation ($p < 0.05$). For rigidity, there were significant relationships between the amounts of posterior and dorsal stimulation and the

optimality of stimulation ($p < 0.05$). There was no significant relationship between stimulation location (VTA location and active contact position) and the optimality of stimulation for tremor, likely due to the reasons mentioned above. Again, these findings are consistent with the VTA mapping results. Additionally, there was no significant correlation between the amount of STN stimulation (VTA inside the STN) or the amount of external stimulation (proxy for ZI stimulation) and the optimality of stimulation, suggesting that the optimal location of stimulation may lie between the two structures (Falconer et al., 2018). Overall, VTA location had more robust relationships with motor improvement and showed greater predictive capability than active contact position. Combining these two measures of stimulation location may improve the reliability of models attempting to predict DBS clinical outcomes (Nestor et al., 2014).

Patient Variability in STN Anatomy and Stimulation Location

High variability in STN anatomy and stimulation location (VTA location and active contact position) was observed across patients. Measurements for this analysis were again taken in the native space of each patient. STN anatomy was characterized by its location (centroid position relative to the MCP) and size (width, length, depth, and volume). The degree of neuroanatomical variability was similar to that reported in previous studies (Daniluk et al., 2010; Duchin et al., 2018; Massey et al., 2012; Richter et al., 2004; Xiao et al., 2014). To account for this variability, the STN centroid was chosen over the typically used MCP as the anatomical reference point when measuring active contact position and VTA location. Previous studies have proposed alternative reference points for a similar reason (Bot et al., 2018). Despite using a more individualized reference point, active contacts were distributed quite evenly around the STN centroid in all directions (Figure 2-11), making it difficult to determine an optimal location of stimulation based on active contact position alone. In contrast, therapeutic VTAs spread

noticeably more into the posterior and dorsal halves of the STN (Figure 2-12). Interestingly, the location of therapeutic stimulation, as measured by the VTA, varied considerably across patients. This finding highlights the need for n-of-1 modeling approaches when characterizing stimulation location to optimize DBS for individual patients (Cubo et al., 2015).

Limitations and Alternative Modeling Approaches

In this study, neurostimulation models were tailored to each patient by incorporating their individual STN anatomy, DBS lead position and orientation, anisotropic brain tissue conductivity, and clinical stimulation settings in an effort to characterize the most accurate representation of their therapeutic stimulation field. Despite this, there are several limitations that have to be considered when interpreting the results. First, the DBS outcomes evaluated only included rigidity, bradykinesia, and tremor, the primary motor symptoms of PD. Side effects and non-motor outcomes were not included in the overall analysis due to the unavailability of lateralized clinical scores. However, these outcomes can be readily incorporated into the n-of-1 modeling framework reported here, which future studies will do. Second, only therapeutic electrode contacts and VTAs based on the clinically optimized stimulation settings of each patient were evaluated (one active contact and VTA per hemisphere per patient). The remaining three electrode contacts were not included in the overall analysis. This limited the spatial coverage of stimulation in the subthalamic region. However, given that the therapeutic contacts were distributed quite evenly around the STN centroid in all directions (Figure 2-11), sufficient VTA coverage was still attained. Since a specific aim of this study was to determine how variable therapeutic stimulation was across patients, it made sense to focus on the clinically optimized stimulation settings of each patient, as determined through clinical DBS programming. Stimulation settings (and VTAs) associated with side effects or other DBS outcomes can be

analyzed in a similar manner, which again future studies will do. Third, since multiple imaging modalities were required to create each neurostimulation model, image co-registration is a possible source of error. Image co-registration was performed using commercial software for visualizing and analyzing medical imaging (Analyze) to minimize error between pre- and post-operative imaging data. A normalized mutual information algorithm was used to precisely align the CT and DT imaging of each patient with their MR imaging (Studholme et al., 1998). All co-registrations were done and evaluated by a board certified physician assistant, and verified by a functional neurosurgeon. If deemed necessary by visual inspection, manual refinements were made to ensure an accurate co-registration. Fourth, the brain was assumed to be purely resistive and linear with regard to DBS (Bedard et al., 2004). Consequently, all FEMs built were electrostatic. Previous experimental studies have shown that the impedance of gray matter is frequency-independent for clinically relevant stimulation frequencies (Logothetis et al., 2007). Furthermore, previous modeling studies have shown that it is reasonable to ignore the capacitive properties of brain tissue (Grant and Lowery, 2010; Howell and McIntyre, 2016; Schmidt et al., 2013). Regardless, possible limitations with electrostatic solutions can be addressed by frequency-dependent models combined with impedance spectroscopy measurements that account for the resistive and capacitive properties of the tissue (Lempka and McIntyre, 2013). Fifth, FEM solutions were not coupled to biophysical neuron models to determine the VTA. Instead, the VTA was defined by activation field strength thresholds of the electric field (Astrom et al., 2015). These thresholds were derived for clinically relevant stimulation amplitudes and pulse widths using axon cable models. An exponential was fit to the activation field thresholds corresponding to an axon diameter of 2.5 μm and a stimulation pulse width of 60 μs to calculate the individual thresholds for each patient based on their therapeutic stimulation amplitude.

Astrom et al. showed that the VTA can be approximated by a constant electric field threshold without the need to couple axon models to the FEM solution (Astrom et al., 2015). This greatly reduces computation time, which is highly favorable since an intended application of this work is to run simulations to test and optimize stimulation settings for patients in a clinical setting. However, it is important to note that their analyses were performed using isotropic tissue conductivities. Lastly, tractography was not incorporated into the n-of-1 modeling framework. Several studies have used tractography to aid in identifying optimal stimulation sites to treat PD with DBS (Akram et al., 2017; Avecillas-Chasin et al., 2019; Garcia-Gomar et al., 2017; Gunalan et al., 2017; O'Halloran et al., 2016). This is of interest because DBS is hypothesized to elicit its therapeutic effect through a combination of axonal activation and cellular inhibition (McIntyre et al., 2004a; McIntyre and Hahn, 2010). The DT imaging data used to estimate the anisotropic tissue conductivities for each patient can also be used to perform tractography. Doing so would allow direct comparison of gray and white matter stimulation, such as the hyperdirect pathway and internal capsule, and their effects on DBS outcomes (Akram et al., 2017; Chen et al., 2018; Gunalan et al., 2017). However, the accuracy of the tractography results would be limited by the voxel resolution of the DT imaging (Rodrigues et al., 2018).

Regarding clinical application of the n-of-1 modeling framework reported here, alternative methods of modeling the VTA are available (Cubo et al., 2017; Madler and Coenen, 2012). One such approach uses a sphere centered at the active contact to estimate the VTA, where the radius of the sphere is a function of the stimulation amplitude and electrode impedance (Madler and Coenen, 2012). To assess the validity of this approximation, spherical VTAs were calculated for each patient and the overall analysis was repeated using them in place of the n-of-1 VTAs. Spherical VTA modeling was unable to reproduce the results presented in this study and

tended to overestimate the size of the VTA (data not shown). Previous studies have described VTA overestimation as a possible limitation of simplified modeling approaches (Butson and McIntyre, 2005; Chaturvedi et al., 2006). While simplified VTA modeling approaches can be useful in identifying general regions where stimulation would be therapeutic, they are limited in their ability to optimize stimulation at the individual patient level because they typically do not take into account tissue anisotropy, one of the most relevant factors impacting VTA prediction accuracy.

Conclusion

Accurate characterization of the spread of stimulation in the brain is important for optimizing STN DBS for PD. High variability in neuroanatomy, stimulation location, and motor improvement across patients highlights the need for n-of-1 modeling techniques. Using an atlas-independent, n-of-1 tissue activation modeling approach, this study mapped the optimal location of stimulation to the dorsolateral border of the STN, in the posterior half of the nucleus. This location varied little when motor symptoms were analyzed individually, suggesting that optimal stimulation sites for rigidity, bradykinesia, and tremor may not be unique. Therapeutic stimulation spread noticeably more in the dorsal direction, providing additional evidence for cZI as an important DBS target. The n-of-1 modeling approach presented in this study can be used to develop and evaluate stimulation strategies to improve clinical outcome on an individual basis. Furthermore, these methods can be used to investigate the non-motor and side effects associated with STN DBS and be extended to other conditions treated with DBS, such as essential tremor and depression, to identify other optimal stimulation sites.

References

- Akram, H., Sotiropoulos, S.N., Jbabdi, S., Georgiev, D., Mahlknecht, P., Hyam, J., Foltynie, T., Limousin, P., De Vita, E., Jahanshahi, M., Hariz, M., Ashburner, J., Behrens, T., Zrinzo, L., 2017. Subthalamic deep brain stimulation sweet spots and hyperdirect cortical connectivity in Parkinson's disease. *Neuroimage* 158, 332-345.
- Alkemade, A., 2013. Subdivisions and anatomical boundaries of the subthalamic nucleus. *J Neurosci* 33, 9233-9234.
- Anderson, D., Beecher, G., Ba, F., 2017. Deep Brain Stimulation in Parkinson's Disease: New and Emerging Targets for Refractory Motor and Nonmotor Symptoms. *Parkinsons Dis* 2017, 5124328.
- Ashkan, K., Rogers, P., Bergman, H., Ughratdar, I., 2017. Insights into the mechanisms of deep brain stimulation. *Nature Reviews Neurology* 13, 548-554.
- Astrom, M., Diczfalusy, E., Martens, H., Wardell, K., 2015. Relationship between neural activation and electric field distribution during deep brain stimulation. *IEEE Trans Biomed Eng* 62, 664-672.
- Astrom, M., Lemaire, J.J., Wardell, K., 2012. Influence of heterogeneous and anisotropic tissue conductivity on electric field distribution in deep brain stimulation. *Med Biol Eng Comput* 50, 23-32.
- Astrom, M., Zrinzo, L.U., Tisch, S., Tripoliti, E., Hariz, M.I., Wardell, K., 2009. Method for patient-specific finite element modeling and simulation of deep brain stimulation. *Med Biol Eng Comput* 47, 21-28.
- Avecillas-Chasin, J.M., Alonso-Frech, F., Nombela, C., Villanueva, C., Barcia, J.A., 2019. Stimulation of the Tractography-Defined Subthalamic Nucleus Regions Correlates With Clinical Outcomes. *Neurosurgery*.
- Bedard, C., Kroger, H., Destexhe, A., 2004. Modeling extracellular field potentials and the frequency-filtering properties of extracellular space. *Biophysical journal* 86, 1829-1842.
- Benabid, A.L., Chabardes, S., Mitrofanis, J., Pollak, P., 2009. Deep brain stimulation of the subthalamic nucleus for the treatment of Parkinson's disease. *Lancet Neurol* 8, 67-81.
- Bentley, J.N., Guan, Z., Cummings, K.S., Chou, K.L., Patil, P.G., 2017. Influence of Intracranial Air on Electrode Position and Clinical Outcomes following Deep Brain Stimulation for Parkinson's Disease. *Stereotact Funct Neurosurg* 95, 6-12.
- Blomstedt, P., Fytagoridis, A., Astrom, M., Linder, J., Forsgren, L., Hariz, M.I., 2012. Unilateral caudal zona incerta deep brain stimulation for Parkinsonian tremor. *Parkinsonism Relat Disord* 18, 1062-1066.

- Bot, M., Schuurman, P.R., Odekerken, V.J.J., Verhagen, R., Contarino, F.M., De Bie, R.M.A., van den Munckhof, P., 2018. Deep brain stimulation for Parkinson's disease: defining the optimal location within the subthalamic nucleus. *J Neurol Neurosurg Psychiatry* 89, 493-498.
- Butson, C.R., 2012. Computational models of neuromodulation. *Int Rev Neurobiol* 107, 5-22.
- Butson, C.R., Cooper, S.E., Henderson, J.M., McIntyre, C.C., 2006. Predicting the effects of deep brain stimulation with diffusion tensor based electric field models. *Med Image Comput Comput Assist Interv* 9, 429-437.
- Butson, C.R., Cooper, S.E., Henderson, J.M., McIntyre, C.C., 2007. Patient-specific analysis of the volume of tissue activated during deep brain stimulation. *Neuroimage* 34, 661-670.
- Butson, C.R., Cooper, S.E., Henderson, J.M., Wolgamuth, B., McIntyre, C.C., 2011. Probabilistic analysis of activation volumes generated during deep brain stimulation. *Neuroimage* 54, 2096-2104.
- Butson, C.R., McIntyre, C.C., 2005. Tissue and electrode capacitance reduce neural activation volumes during deep brain stimulation. *Clin Neurophysiol* 116, 2490-2500.
- Butson, C.R., McIntyre, C.C., 2006. Role of electrode design on the volume of tissue activated during deep brain stimulation. *J Neural Eng* 3, 1-8.
- Caire, F., Ranoux, D., Guehl, D., Burbaud, P., neurochirurgica, C.-E., 2013. A systematic review of studies on anatomical position of electrode contacts used for chronic subthalamic stimulation in Parkinson's disease. *Acta neurochirurgica*.
- Chaturvedi, A., Butson, C.R., Cooper, S.E., McIntyre, C.C., 2006. Subthalamic nucleus deep brain stimulation: accurate axonal threshold prediction with diffusion tensor based electric field models. *Conf Proc IEEE Eng Med Biol Soc* 1, 1240-1243.
- Chaturvedi, A., Butson, C.R., Lempka, S.F., Cooper, S.E., McIntyre, C.C., 2010. Patient-specific models of deep brain stimulation: influence of field model complexity on neural activation predictions. *Brain Stimul* 3, 65-67.
- Chen, Y., Ge, S., Li, Y., Li, N., Wang, J., Wang, X., Li, J., Jing, J., Su, M., Zheng, Z., Luo, T., Qiu, C., Wang, X., 2018. Role of the Cortico-Subthalamic Hyperdirect Pathway in Deep Brain Stimulation for the Treatment of Parkinson Disease: A Diffusion Tensor Imaging Study. *World Neurosurg* 114, e1079-e1085.
- Chou, K.L., Taylor, J.L., related disorders, P.-P.G., 2013. The MDS– UPDRS tracks motor and non-motor improvement due to subthalamic nucleus deep brain stimulation in Parkinson disease. *Parkinsonism & related disorders*.
- Collins, K.L., Lehmann, E.M., Patil, P.G., 2010. Deep brain stimulation for movement disorders. *Neurobiol Dis* 38, 338-345.

- Conrad, E.C., Mossner, J.M., Chou, K.L., Patil, P.G., 2018. Atlas-Independent, Electrophysiological Mapping of the Optimal Locus of Subthalamic Deep Brain Stimulation for the Motor Symptoms of Parkinson Disease. *Stereotact Funct Neurosurg* 96, 91-99.
- Cubo, R., Fahlstrom, M., Jiltsova, E., Andersson, H., Medvedev, A., 2017. Semi-individualized electrical models in Deep Brain Stimulation: a variability analysis. 2017 Ieee Conference on Control Technology and Applications (Ccta 2017), 517-522.
- Cubo, R., Medvedev, A., Test, Å.-M., 2015. Model-based optimization of individualized deep brain stimulation therapy. *IEEE Design & Test*.
- Daniluk, S., K, G.D., Ellias, S.A., Novak, P., Nazzaro, J.M., 2010. Assessment of the variability in the anatomical position and size of the subthalamic nucleus among patients with advanced Parkinson's disease using magnetic resonance imaging. *Acta Neurochir (Wien)* 152, 201-210; discussion 210.
- Deniau, J.M., Degos, B., Bosch, C., Maurice, N., 2010. Deep brain stimulation mechanisms: beyond the concept of local functional inhibition. *Eur J Neurosci* 32, 1080-1091.
- Deuschl, G., Schade-Brittinger, C., Krack, P., Volkmann, J., Schafer, H., Botzel, K., Daniels, C., Deutschlander, A., Dillmann, U., Eisner, W., Gruber, D., Hamel, W., Herzog, J., Hilker, R., Klebe, S., Kloss, M., Koy, J., Krause, M., Kupsch, A., Lorenz, D., Lorenzl, S., Mehdorn, H.M., Moringlane, J.R., Oertel, W., Pinski, M.O., Reichmann, H., Reuss, A., Schneider, G.H., Schnitzler, A., Steude, U., Sturm, V., Timmermann, L., Tronnier, V., Trottenberg, T., Wojtecki, L., Wolf, E., Poewe, W., Voges, J., German Parkinson Study Group, N.S., 2006. A randomized trial of deep-brain stimulation for Parkinson's disease. *N Engl J Med* 355, 896-908.
- Dickie, D.A., Shenkin, S.D., Anblagan, D., Lee, J., Blesa Cabez, M., Rodriguez, D., Boardman, J.P., Waldman, A., Job, D.E., Wardlaw, J.M., 2017. Whole Brain Magnetic Resonance Image Atlases: A Systematic Review of Existing Atlases and Caveats for Use in Population Imaging. *Front Neuroinform* 11, 1.
- Duchin, Y., Shamir, R.R., Patriat, R., Kim, J., Vitek, J.L., Sapiro, G., Harel, N., 2018. Patient-specific anatomical model for deep brain stimulation based on 7 Tesla MRI. *PLoS One* 13, e0201469.
- Falconer, R.A., Rogers, S.L., Shenai, M., 2018. Using Directional Deep Brain Stimulation to Co-activate the Subthalamic Nucleus and Zona Incerta for Overlapping Essential Tremor/Parkinson's Disease Symptoms. *Front Neurol* 9, 544.
- Florence, G., Sameshima, K., Fonoff, E.T., Hamani, C., 2016. Deep Brain Stimulation: More Complex than the Inhibition of Cells and Excitation of Fibers. *Neuroscientist* 22, 332-345.
- Frankemolle, A.M., Wu, J., Noecker, A.M., Voelcker-Rehage, C., Ho, J.C., Vitek, J.L., McIntyre, C.C., Alberts, J.L., 2010. Reversing cognitive-motor impairments in Parkinson's disease patients using a computational modelling approach to deep brain stimulation programming. *Brain* 133, 746-761.

- Garcia-Gomar, M.G., Soto-Abraham, J., Velasco-Campos, F., Concha, L., 2017. Anatomic characterization of prelemniscal radiations by probabilistic tractography: implications in Parkinson's disease. *Brain structure & function* 222, 71-81.
- Grant, P.F., Lowery, M.M., 2010. Effect of dispersive conductivity and permittivity in volume conductor models of deep brain stimulation. *IEEE Trans Biomed Eng* 57, 2386-2393.
- Gunalan, K., Chaturvedi, A., Howell, B., Duchin, Y., Lempka, S.F., Patriat, R., Sapiro, G., Harel, N., McIntyre, C.C., 2017. Creating and parameterizing patient-specific deep brain stimulation pathway-activation models using the hyperdirect pathway as an example. *PLoS One* 12, e0176132.
- Gunalan, K., Howell, B., McIntyre, C.C., 2018. Quantifying axonal responses in patient-specific models of subthalamic deep brain stimulation. *Neuroimage* 172, 263-277.
- Haegelen, C., Baumgarten, C., Houvenaghel, J.F., Zhao, Y., Peron, J., Drapier, S., Jannin, P., Morandi, X., 2018. Functional atlases for analysis of motor and neuropsychological outcomes after medial globus pallidus and subthalamic stimulation. *PLoS One* 13, e0200262.
- Herzog, J., Fietzek, U., Hamel, W., Morsnowski, A., Steigerwald, F., Schrader, B., Weinert, D., Pfister, G., Muller, D., Mehdorn, H.M., Deuschl, G., Volkmann, J., 2004. Most effective stimulation site in subthalamic deep brain stimulation for Parkinson's disease. *Mov Disord* 19, 1050-1054.
- Houshmand, L., 2015. Optimized Targeting in Deep Brain Stimulation for Movement Disorders. *Optimized Targeting in Deep Brain Stimulation for Movement Disorders*.
- Houshmand, L., Cummings, K.S., Chou, K.L., Patil, P.G., 2014. Evaluating indirect subthalamic nucleus targeting with validated 3-tesla magnetic resonance imaging. *Stereotact Funct Neurosurg* 92, 337-345.
- Howell, B., Huynh, B., Grill, W.M., 2015. Design and *in vivo* evaluation of more efficient and selective deep brain stimulation electrodes. *J Neural Eng* 12, 046030.
- Howell, B., McIntyre, C.C., 2016. Analyzing the tradeoff between electrical complexity and accuracy in patient-specific computational models of deep brain stimulation. *J Neural Eng* 13, 036023.
- Howell, B., McIntyre, C.C., 2017. Role of Soft-Tissue Heterogeneity in Computational Models of Deep Brain Stimulation. *Brain Stimul* 10, 46-50.
- Ineichen, C., Shepherd, N.R., Surucu, O., 2018. Understanding the Effects and Adverse Reactions of Deep Brain Stimulation: Is It Time for a Paradigm Shift Toward a Focus on Heterogenous Biophysical Tissue Properties Instead of Electrode Design Only? *Front Hum Neurosci* 12, 468.

Jaermann, T., Crelier, G., Pruessmann, K.P., Golay, X., Netsch, T., van Muiswinkel, A.M.C., Mori, S., van Zijl, P.C.M., Valavanis, A., Kollias, S., Boesiger, P., 2004. SENSE-DTI at 3 T. *Magnetic Resonance in Medicine*.

Johnson, M.D., Miocinovic, S., McIntyre, C.C., Vitek, J.L., 2008. Mechanisms and targets of deep brain stimulation in movement disorders. *Neurotherapeutics* 5, 294-308.

Kent, A.R., Grill, W.M., 2014. Analysis of deep brain stimulation electrode characteristics for neural recording. *J Neural Eng* 11, 046010.

Kleiner-Fisman, G., Herzog, J., Fisman, D.N., Tamma, F., Lyons, K.E., Pahwa, R., Lang, A.E., Deuschl, G., 2006. Subthalamic nucleus deep brain stimulation: summary and meta-analysis of outcomes. *Mov Disord* 21 Suppl 14, S290-304.

Koivu, M., Huotari, A., Scheperjans, F., Laakso, A., Kivisaari, R., Pekkonen, E., 2018. Motor outcome and electrode location in deep brain stimulation in Parkinson's disease. *Brain Behav* 8, e01003.

Lempka, S.F., McIntyre, C.C., 2013. Theoretical analysis of the local field potential in deep brain stimulation applications. *PLoS One* 8, e59839.

Logothetis, N.K., Kayser, C., Oeltermann, A., 2007. *In vivo* measurement of cortical impedance spectrum in monkeys: implications for signal propagation. *Neuron* 55, 809-823.

Madler, B., Coenen, V.A., 2012. Explaining clinical effects of deep brain stimulation through simplified target-specific modeling of the volume of activated tissue. *AJNR Am J Neuroradiol* 33, 1072-1080.

Maks, C.B., Butson, C.R., Walter, B.L., Vitek, J.L., McIntyre, C.C., 2009. Deep brain stimulation activation volumes and their association with neurophysiological mapping and therapeutic outcomes. *J Neurol Neurosurg Psychiatry* 80, 659-666.

Massey, L.A., Miranda, M.A., Zrinzo, L., Al-Helli, O., Parkes, H.G., Thornton, J.S., So, P.W., White, M.J., Mancini, L., Strand, C., Holton, J.L., Hariz, M.I., Lees, A.J., Revesz, T., Yousry, T.A., 2012. High resolution MR anatomy of the subthalamic nucleus: imaging at 9.4 T with histological validation. *Neuroimage* 59, 2035-2044.

McClelland, S., 3rd, Ford, B., Senatus, P.B., Winfield, L.M., Du, Y.E., Pullman, S.L., Yu, Q., Frucht, S.J., McKhann, G.M., 2nd, Goodman, R.R., 2005. Subthalamic stimulation for Parkinson disease: determination of electrode location necessary for clinical efficacy. *Neurosurg Focus* 19, E12.

McIntyre, C.C., Frankenmoller, A.M., Wu, J., Noecker, A.M., Alberts, J.L., 2009. Customizing deep brain stimulation to the patient using computational models. *Conf Proc IEEE Eng Med Biol Soc* 2009, 4228-4229.

McIntyre, C.C., Grill, W.M., Sherman, D.L., Thakor, N.V., 2004a. Cellular effects of deep brain stimulation: model-based analysis of activation and inhibition. *J Neurophysiol* 91, 1457-1469.

- McIntyre, C.C., Hahn, P.J., 2010. Network perspectives on the mechanisms of deep brain stimulation. *Neurobiol Dis* 38, 329-337.
- McIntyre, C.C., Mori, S., Sherman, D.L., Thakor, N.V., Vitek, J.L., 2004b. Electric field and stimulating influence generated by deep brain stimulation of the subthalamic nucleus. *Clin Neurophysiol* 115, 589-595.
- McIntyre, C.C., Savasta, M., Kerkerian-Le Goff, L., Vitek, J.L., 2004c. Uncovering the mechanism(s) of action of deep brain stimulation: activation, inhibition, or both. *Clin Neurophysiol* 115, 1239-1248.
- Miocinovic, S., Lempka, S.F., Russo, G.S., Maks, C.B., Butson, C.R., Sakaie, K.E., Vitek, J.L., McIntyre, C.C., 2009. Experimental and theoretical characterization of the voltage distribution generated by deep brain stimulation. *Exp Neurol* 216, 166-176.
- Miocinovic, S., Parent, M., Butson, C.R., Hahn, P.J., Russo, G.S., Vitek, J.L., McIntyre, C.C., 2006. Computational analysis of subthalamic nucleus and lenticular fasciculus activation during therapeutic deep brain stimulation. *J Neurophysiol* 96, 1569-1580.
- Montgomery, E.B., Jr., Gale, J.T., 2008. Mechanisms of action of deep brain stimulation(DBS). *Neurosci Biobehav Rev* 32, 388-407.
- Nestor, K.A., Jones, J.D., Butson, C.R., Morishita, T., Jacobson, C.E.t., Peace, D.A., Chen, D., Foote, K.D., Okun, M.S., 2014. Coordinate-based lead location does not predict Parkinson's disease deep brain stimulation outcome. *PLoS One* 9, e93524.
- Nowacki, A., Nguyen, T.A., Tinkhauser, G., Petermann, K., Debove, I., Wiest, R., Pollo, C., 2018. Accuracy of different three-dimensional subcortical human brain atlases for DBS -lead localisation. *Neuroimage Clin* 20, 868-874.
- O'Halloran, R.L., Chartrain, A.G., Rasouli, J.J., Ramdhani, R.A., Kopell, B.H., 2016. Case Study of Image-Guided Deep Brain Stimulation: Magnetic Resonance Imaging–Based White Matter Tractography Shows Differences in Responders and Nonresponders. *World Neurosurgery*.
- Okun, M.S., 2012. Deep-Brain Stimulation for Parkinson's Disease. *New England Journal of Medicine* 367, 1529-1538.
- Okun, M.S., Tagliati, M., Pourfar, M., Fernandez, H.H., Rodriguez, R.L., Alterman, R.L., Foote, K.D., 2005. Management of referred deep brain stimulation failures: a retrospective analysis from 2 movement disorders centers. *Arch Neurol* 62, 1250-1255.
- Paek, S.H., Han, J.H., Lee, J.Y., Kim, C., Jeon, B.S., Kim, D.G., 2008. Electrode position determined by fused images of preoperative and postoperative magnetic resonance imaging and surgical outcome after subthalamic nucleus deep brain stimulation. *Neurosurgery* 63, 925-936; discussion 936-927.

- Patil, P.G., Conrad, E.C., Aldridge, J.W., Chenevert, T.L., Chou, K.L., 2012. The anatomical and electrophysiological subthalamic nucleus visualized by 3-T magnetic resonance imaging. *Neurosurgery* 71, 1089-1095; discussion 1095.
- Pelot, N.A., Thio, B.J., Grill, W.M., 2018. Modeling Current Sources for Neural Stimulation in COMSOL. *Front Comput Neurosci* 12, 40.
- Plaha, P., Ben-Shlomo, Y., Patel, N.K., Gill, S.S., 2006. Stimulation of the caudal zona incerta is superior to stimulation of the subthalamic nucleus in improving contralateral parkinsonism. *Brain* 129, 1732-1747.
- Pollo, C., Vingerhoets, F., Pralong, E., Ghika, J., Maeder, P., Meuli, R., Thiran, J.P., Villemure, J.G., 2007. Localization of electrodes in the subthalamic nucleus on magnetic resonance imaging. *J Neurosurg* 106, 36-44.
- Richter, E.O., Hoque, T., Halliday, W., Lozano, A.M., Saint-Cyr, J.A., 2004. Determining the position and size of the subthalamic nucleus based on magnetic resonance imaging results in patients with advanced Parkinson disease. *J Neurosurg* 100, 541-546.
- Rodrigues, N.B., Mithani, K., Meng, Y., Lipsman, N., Hamani, C., 2018. The Emerging Role of Tractography in Deep Brain Stimulation: Basic Principles and Current Applications. *Brain Sci* 8, 23.
- Schmidt, C., Grant, P., Lowery, M., van Rienen, U., 2013. Influence of uncertainties in the material properties of brain tissue on the probabilistic volume of tissue activated. *IEEE Trans Biomed Eng* 60, 1378-1387.
- Schmidt, C., van Rienen, U., 2012. Modeling the field distribution in deep brain stimulation: the influence of anisotropy of brain tissue. *IEEE Trans Biomed Eng* 59, 1583-1592.
- Studholme, C., Hawkes, D.J., Hill, D.L.G., 1998. Normalized entropy measure for multimodality image alignment. *Medical Imaging 1998: Image Processing*.
- Talairach, J., Tournoux, P., 1988. Co-planar stereotaxic atlas of the human brain. 3-Dimensional proportional system: an approach to cerebral imaging. Co-planar stereotaxic atlas of the human brain. 3-Dimensional proportional system: an approach to cerebral imaging.
- Tuch, D.S., Wedeen, V.J., Dale, A.M., George, J.S., Belliveau, J.W., 2001. Conductivity tensor mapping of the human brain using diffusion tensor MRI. *Proc Natl Acad Sci U S A* 98, 11697-11701.
- van Dijk, K.J., Verhagen, R., Chaturvedi, A., McIntyre, C.C., Bour, L.J., Heida, C., Veltink, P.H., 2015. A novel lead design enables selective deep brain stimulation of neural populations in the subthalamic region. *J Neural Eng* 12, 046003.
- Vargas Cardona, H.D., Orozco, Á.A., Álvarez, M.A., 2017. Analysis of the Geometry and Electric Properties of Brain Tissue in Simulation Models for Deep Brain Stimulation. *CIARP: Iberoamerican Congress on Pattern Recognition*.

Verhagen, R., Bour, L.J., Odekerken, V.J.J., van den Munckhof, P., Schuurman, P.R., de Bie, R.M.A., 2019. Electrode Location in a Microelectrode Recording-Based Model of the Subthalamic Nucleus Can Predict Motor Improvement After Deep Brain Stimulation for Parkinson's Disease. *Brain Sci* 9.

Vitek, J.L., 2002. Mechanisms of deep brain stimulation: excitation or inhibition. *Mov Disord* 17 Suppl 3, S69-72.

Voges, J., Volkmann, J., Allert, N., Lehrke, R., Koulousakis, A., Freund, H.J., Sturm, V., 2002. Bilateral high-frequency stimulation in the subthalamic nucleus for the treatment of Parkinson disease: correlation of therapeutic effect with anatomical electrode position. *J Neurosurg* 96, 269-279.

Welter, M.L., Schupbach, M., Czernecki, V., Karachi, C., Fernandez-Vidal, S., Golmard, J.L., Serra, G., Navarro, S., Welaratne, A., Hartmann, A., Mesnage, V., Pineau, F., Cornu, P., Pidoux, B., Worbe, Y., Zikos, P., Grabli, D., Galanaud, D., Bonnet, A.M., Belaid, H., Dormont, D., Vidailhet, M., Mallet, L., Houeto, J.L., Bardin, E., Yelnik, J., Agid, Y., 2014. Optimal target localization for subthalamic stimulation in patients with Parkinson disease. *Neurology* 82, 1352-1361.

Wodarg, F., Herzog, J., Reese, R., Falk, D., Pinsker, M.O., Steigerwald, F., Jansen, O., Deuschl, G., Mehdorn, H.M., Volkmann, J., 2012. Stimulation site within the MRI-defined STN predicts postoperative motor outcome. *Movement Disorders*.

Xiao, Y., Jannin, P., D'Albis, T., Guizard, N., Haegelen, C., Lalys, F., Verin, M., Collins, D.L., 2014. Investigation of morphometric variability of subthalamic nucleus, red nucleus, and substantia nigra in advanced Parkinson's disease patients using automatic segmentation and PCA-based analysis. *Hum Brain Mapp* 35, 4330-4344.

Yokoyama, T., Ando, N., Sugiyama, K., Akamine, S., Namba, H., 2006. Relationship of stimulation site location within the subthalamic nucleus region to clinical effects on parkinsonian symptoms. *Stereotact Funct Neurosurg* 84, 170-175.

Zitella, L.M., Mohsenian, K., Pahwa, M., Gloeckner, C., Johnson, M.D., 2013. Computational modeling of pedunclopontine nucleus deep brain stimulation. *J Neural Eng* 10, 045005.

Zitella, L.M., Teplitzky, B.A., Yager, P., Hudson, H.M., Brintz, K., Duchin, Y., Harel, N., Vitek, J.L., Baker, K.B., Johnson, M.D., 2015. Subject-specific computational modeling of DBS in the PPTg area. *Front Comput Neurosci* 9, 93.

Chapter 3

Clinical Validation of Atlas-Independent, N-of-1 Thalamic Segmentation and Tissue Activation Modeling in Thalamic Deep Brain Stimulation for Essential Tremor

Abstract

Deep brain stimulation (DBS) of the ventral intermediate (VIM) nucleus of the thalamus (also known as the ventral part of the ventral lateral posterior (VLpv) nucleus) is the primary neurosurgical therapy to treat idiopathic essential tremor (ET). Thalamic segmentation and tissue activation modeling have improved the understanding of structure-function relationships between DBS lead location, stimulation parameters, and clinical efficacy. Atlas-based segmentation and modeling approaches normalize anatomical variability across patients, providing clinical explanations that hold for the study population as a whole. However, DBS outcomes at the individual patient level may prove difficult to explain using atlas-based approaches.

An atlas-independent, n-of-1 modeling methodology combining diffusion tensor (DT) - based thalamic segmentation and tissue activation modeling was developed to evaluate the clinical effects of thalamic DBS on an individual patient basis. Twenty-two patients with ET who received unilateral thalamic DBS participated in this retrospective study. For each patient, the thalamus was segmented into 13 distinct subnuclei using a modified k-means clustering algorithm. Volumes of tissue activation (VTAs) associated with therapeutic outcome and side effects were calculated using finite element analysis. The amount of VTA overlap with the motor

and sensory regions of the thalamus was then measured to correlate motor and sensory thalamus stimulation with the observed outcomes. The results obtained using n-of-1 thalamic segmentation were compared with those obtained using an atlas-based segmentation approach to further assess the methodology.

Within the thalamus, the shape and size of the VTA was highly variable across individual patients. Using n-of-1 thalamic segmentation, 91% of the VTAs associated with therapeutic outcome overlapped with motor thalamus despite only 50% of the therapeutic electrode contacts being located in the structure. In contrast, 100% of the VTAs overlapped with motor thalamus using atlas-based segmentation. Both segmentation approaches showed that therapeutic VTAs had significantly more overlap with motor than sensory thalamus. For sustained paresthesia, 94% of the sustained paresthesia VTAs overlapped with sensory thalamus using n-of-1 thalamic segmentation, while 74% of the VTAs overlapped with sensory thalamus using atlas-based segmentation. Both segmentation approaches showed that sustained paresthesia VTAs had significantly more overlap with sensory thalamus than therapeutic VTAs. For dysarthria/motor contraction, 68% of the dysarthria/motor contraction VTAs spread outside of the thalamus using n-of-1 thalamic segmentation, while 79% of the VTAs spread outside of the thalamus using atlas-based segmentation. Only n-of-1 thalamic segmentation showed that dysarthria/motor contraction VTAs had significantly more external stimulation than therapeutic VTAs. Overall, n-of-1 thalamic segmentation performed better than atlas-based segmentation in terms of explaining DBS side effects and when the thalamic anatomy of the patient differed considerably in size and shape from the atlas thalamus.

While traditional atlas-based thalamic segmentation and VTA modeling are reliable tools for general DBS planning and mechanistic study, enhanced accuracy at the individual patient

level may be possible with atlas-independent, n-of-1 modeling approaches utilizing DT imaging data.

Introduction

Deep brain stimulation (DBS) of the thalamus is the primary neurosurgical therapy to treat idiopathic essential tremor (ET) (Benabid et al., 1996; Deuschl et al., 2011; Pahwa et al., 2006). The DBS target, known as the ventral intermediate (VIM) nucleus (Vaillancourt et al., 2003) or the ventral part of the ventral lateral posterior (VLpv) nucleus (Macchi and Jones, 1997), is a terminus of the cerebellothalamic outflow tract (Calabrese, 2016; Kwon et al., 2011). While the VIM and other thalamic subnuclei can be identified using histology, they are not clearly visualized using conventional magnetic resonance (MR) imaging (Klein et al., 2012; Spiegelmann et al., 2006; Zerroug et al., 2016). Consequently, surgical targeting and clinical studies for thalamic DBS have relied on the use of stereotactic brain atlases to map the location of relevant structures (Forutan et al., 2015; Lemaire et al., 2010; Morel et al., 1997; Schaltenbrand et al., 1977). Patient specificity is achieved by fitting a generic spatial model of the thalamus and other deep brain structures to individual anatomic imaging data. During DBS surgery, neurosurgeons localize the VIM target using atlas-based stereotactic coordinates and refine the location of the DBS lead iteratively using intraoperative electrophysiological testing (Hemm et al., 2016; Klein et al., 2012). Improved targeting accuracy could be achieved with individualized diffusion tensor (DT) -based thalamic segmentation and fiber tractography, which, in turn, would simplify surgery, reduce operative risk, and improve patient outcome (Akram et al., 2018; Calabrese, 2016; Coenen et al., 2011; Deoni et al., 2007; Lambert et al., 2017).

Diffusion tensor imaging has already been used to delineate the distinct subnuclei comprising the thalamus in individual subjects (Johansen-Berg et al., 2005; Lambert et al., 2017;

Wiegell et al., 2003). Several DT-based thalamic segmentation approaches also exist (Battistella et al., 2017; Deoni et al., 2007; Duan et al., 2007; Grassi et al., 2008; Jonasson et al., 2007; Mang et al., 2012; Rittner et al., 2010; Schultz, 2011; Ziyang and Westin, 2008). Fiber tractography is an emerging tool to identify the cerebellothalamic tracts for DBS targeting (Akram et al., 2018; Calabrese, 2016).

In addition to accurately targeting the VIM, the success of thalamic DBS depends on the activation of neural tissue surrounding the DBS lead. Finite element computational models of the volume of tissue activated (VTA) have been used to study the regional effects of DBS and optimize stimulation parameters to treat Parkinson disease (Butson et al., 2007; Butson et al., 2011; Chaturvedi et al., 2010; Madler and Coenen, 2012; Maks et al., 2009). Such approaches have also relied on atlas fitting to achieve patient specificity and make comparisons across subjects. Several studies have applied patient-specific, atlas-based VTA modeling to thalamic DBS for ET (Dembek et al., 2017; Vassal et al., 2012), while others have modeled thalamic DBS in different capacities (Hemm et al., 2016; Keane et al., 2012; Kuncel et al., 2008; Pouratian et al., 2011). To date, individual DT imaging data has yet to be used to create atlas-independent, n-of-1 VTA models for thalamic DBS in a large patient group.

In this retrospective study, a novel methodology to evaluate the clinical effects of thalamic DBS on an individual patient basis is presented. The methodology combined atlas-independent thalamic segmentation and tissue activation modeling using individual 3 T DT imaging data obtained from 22 patients with ET who received unilateral thalamic DBS. For each patient, the thalamus was segmented into 13 distinct subnuclei using a modified, DT-based k-means clustering algorithm. Tissue activation models were created using the same DT imaging data and then combined with the thalamic segmentation results. Volumes of tissue activation

associated with therapeutic outcome (tremor suppression) and side effects (sustained paresthesia and dysarthria/motor contraction) were calculated using an n-of-1 tissue activation modeling approach (Chapter 2). The amount of VTA overlap with the motor and sensory regions of the thalamus was then measured to correlate motor and sensory thalamus stimulation with observed outcomes. The results obtained using n-of-1 thalamic segmentation were compared with those obtained using an atlas-based thalamic segmentation approach to further assess the methodology.

Methods

Patient Selection

For this study, patients were drawn from a clinical database of patients who had undergone unilateral thalamic DBS for idiopathic ET at the University of Michigan. Selection criteria were an established diagnosis of medically intractable ET and the availability of pre-operative MR and DT imaging, post-operative CT imaging, and clinical assessments from the monopolar review performed a few weeks after DBS surgery. Patients with structural brain abnormalities on MR imaging, non-monopolar stimulation, or comorbid neuropsychiatric disorders, such as dementia or depression, were excluded. Twenty-two patients were selected (Table 3-1). Informed consent was obtained from all patients in accordance with the policies of the Medical Institutional Review Board at the University of Michigan.

Table 3-1 Patient demographics

	n	Mean	Standard deviation	Minimum	Maximum
Age at baseline [yr]	22	66.9	9.1	47.3	79.3
Age diagnosed [yr]	22	40.0	21.3	9	73
Disease duration at baseline [yr]	22	26.8	20.7	1.7	65.8

n: 22 patients total (14 male and 8 female; 19 left implant and 3 right implant).

Pre-Operative Image Acquisition and Processing

MR and DT images were obtained pre-operatively for each patient during their baseline evaluation. All imaging was performed on a Philips Ingenia 3.0T scanner (Philips Healthcare, Andover, MA, USA). MR images were acquired using a previously reported protocol (Patil et al., 2012), while DT images were acquired using a single-shot echo-planar imaging sequence combined with dS SENSE, a parallel imaging scheme used to decrease image distortion (Jaermann et al., 2004). Diffusion weighting was encoded along 15 independent orientations with a b-value of 800 mm²/s. DT imaging parameters included a 1 x 1 x 2 mm voxel size, 224 x 224 mm field-of-view, and reduction factor of 2. MR images were transformed to Talairach space along the intercommissural and midsagittal planes (Talairach and Tournoux, 1988). The midcommissural point (MCP) was defined as the origin, with positive x, y, and z coordinates corresponding to the right, anterior, and dorsal (superior) directions, respectively. DT images were resampled to match the resolution of the MR images using cubic spline interpolation (Houshmand, 2015) and then oriented to Talairach space via co-registration to the MR images. All image processing was performed by the same individual to minimize registration variability using Analyze, a medical imaging visualization and analysis software package (12.0, AnalyzeDirect, Inc., Overland Park, KS, USA).

Surgical Procedure and Initial Programming Session

Just before surgery, patients were fitted with a Leksell stereotactic frame (Elekta AB, Stockholm, Sweden) and had additional pre-operative MR images acquired at 1.5 T (Patil et al., 2012). The 3.0- and 1.5-T MR images were registered using Analyze and then exported to Framelink (Medtronic, Inc., Minneapolis, MN, USA) for frame-based, unilateral surgical targeting of the VIM. Indirect targeting was initially set to a point 11.5 mm lateral to the

thalamo-ventricular border, 3.5 mm anterior to the posterior commissure, and within the intercommissural plane. During surgery, microelectrode recording and macroelectrode stimulation were performed to refine targeting. A quadripolar DBS lead (model 3387, Medtronic, Inc., Minneapolis, MN, USA) was then precisely placed in the designated location after target confirmation. A movement disorders neurologist (K.L.C.) activated the DBS lead and evaluated each patient for symptom improvement and side effects at each electrode contact. In some cases where patients experienced side effects on all four contacts, the DBS lead was repositioned. Approximately 6 weeks after surgery, patients returned for their initial programming session. The same movement disorders neurologist performed the monopolar review to optimize the stimulation settings of each patient. Stimulation frequency and pulse width were set to 130 Hz and 60 μ s, respectively, while stimulation amplitude varied from 0.5-5 V. The stimulation amplitude at the electrode contact that maximized tremor suppression without inducing side effects was recorded for each patient (Table 3-2). Stimulation amplitudes at electrode contacts that induced sustained paresthesia, defined as paresthesia persisting beyond one minute, or dysarthria/motor contraction were also recorded.

Table 3-2 Clinical DBS settings, electrode impedance, and modeled VTA

	n	Mean	Standard deviation	Minimum	Maximum
Stimulation amplitude [V]	18	1.7	0.5	1.0	2.5
Stimulation amplitude [mA]	4	1.9	0.5	1.5	2.5
Electrode impedance [Ω]	18	1181.1	451.6	609	2501
VTA [mm ³]	22	54.0	33.4	2.4	120.3

Stimulation frequency and pulse width were set to 130 Hz and 60 μ s, respectively. n: 22 patients total (electrode impedance data was unavailable for 4 patients); VTA: volume of tissue activated.

Post-Operative Image Acquisition and Processing and Electrode Contact Localization

CT images were obtained post-operatively for each patient two-to-four weeks after surgery to allow intracranial air to resolve (Bentley et al., 2017). A previously reported protocol was used to acquire the CT imaging (Patil et al., 2012). CT images were oriented to Talairach space via co-registration to the MR images. Electrode contacts were then localized from the registered CT images (88 electrodes and 22 active contacts total). Contact coordinates were measured from CT images in the axial, coronal, and sagittal planes. Visualization of the electrode contacts was optimized via CT windowing (Conrad et al., 2018; Patil et al., 2012). All image processing and contact coordinate measurements were performed by the same individual to minimize registration and localization variability, respectively, using Analyze. Contact coordinates were then exported to MATLAB (R2018b, The MathWorks, Inc., Natick, MA, USA) for analysis.

Thalamic Tracing and Atlas-Independent, N-of-1 Segmentation

Three-dimensional anatomical models of the thalamus were created for each patient (22 thalami total). Thalami were manually traced from MR images in the coronal plane using Analyze (Power et al., 2015) (Figure 3-1). The borders of the thalamus were defined in the axial plane by the third ventricle and posterior limb of the internal capsule, and in the sagittal plane by the lateral ventricle and subthalamic nucleus. All thalami were traced by the same individual (J.C.) and validated by the neurosurgeon who performed the DBS surgeries (P.G.P.) to minimize tracing variability. Object maps containing the thalamic voxels were then exported to MATLAB for segmentation.

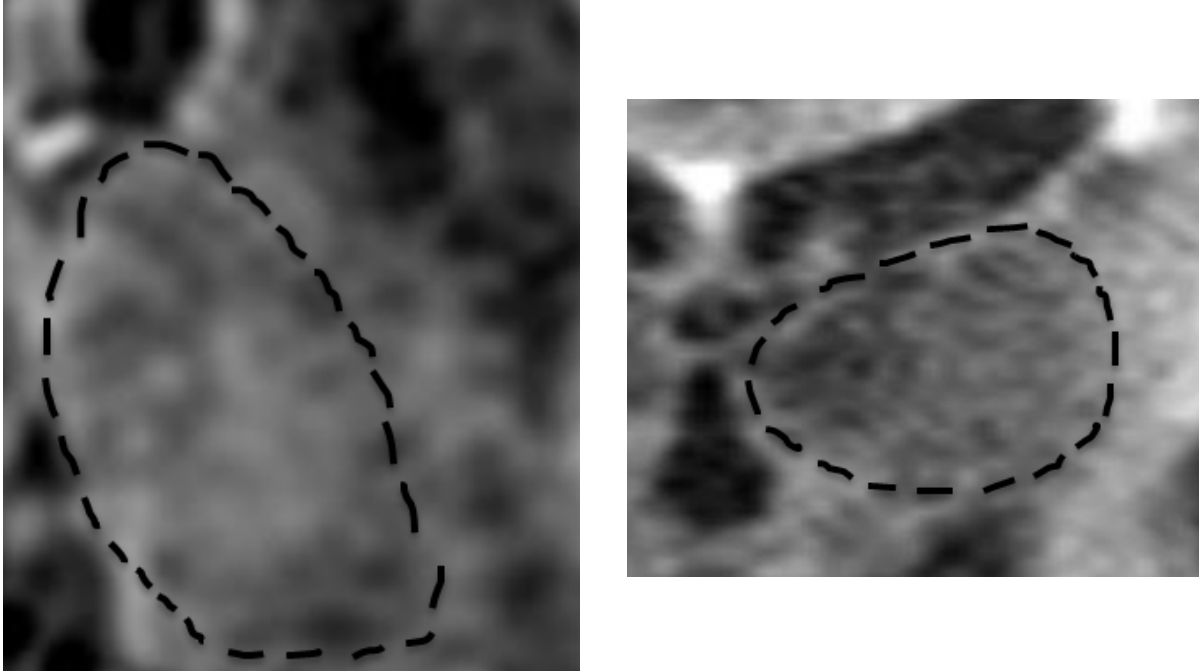


Figure 3-1 Thalamic tracing for one patient. MR images of the thalamus. The thalamic border is indicated by the dashed lines. Axial and coronal views are displayed.

Patient thalami were segmented into 13 distinct subnuclei based on local diffusion tensor information using a modified k-means clustering algorithm (Deoni et al., 2007; Wiegell et al., 2003). Thirteen clusters representing the anterior (A); ventral anterior (VA); ventral lateral anterior (VL_a); ventral lateral posterior, dorsal part (VL_{pd}); ventral lateral posterior, ventral part (VL_{pv}); ventral posterior lateral (VPL), ventral posterior medial (VPM), ventromedial (VM), medial dorsal (MD), lateral dorsal (LD), lateral posterior (LP), centromedian (CM), and pulvinar (Pul) subnuclei were chosen based on the Morel histological atlas (Morel et al., 1997) and previous thalamic segmentation studies (Deoni et al., 2007; Wiegell et al., 2003). The initial coordinates of each subnucleus centroid were determined according to the Morel thalamus. A digital version of the Morel atlas was obtained from (Jakab et al., 2012; Krauth et al., 2010) and exported to MATLAB. The Morel thalamus was then fitted to each patient thalamus via transposition, scaling, and rotation to map the atlas subnuclei centroids to the patient thalami for

k-means clustering. The anisotropic diffusivity of the brain tissue was estimated for each patient from their DT imaging. Diffusion eigenvalue and eigenvector maps were calculated using Analyze and then exported to MATLAB, where they were converted into 3D diffusion tensors on a per-voxel basis (22 tensor fields total) (Houshmand, 2015). The distance metric chosen for k-means clustering took into account the physical location of the thalamic voxels and different properties of the diffusion tensors at each voxel. The reasoning for this was that voxels belonging to a specific subnucleus should be close in spatial proximity and similar in tensor properties, indicating similar histological composition. The position-tensor distance between a voxel j and a subnucleus centroid k , d_{jk} , was defined as a linear combination of the Mahalanobis voxel distance (Wiegell et al., 2003) and the Hybrid tensor distance (de Luis-García et al., 2009; de Luis-García et al., 2012):

$$d_{jk} = \|\mathbf{x}_j - \bar{\mathbf{x}}_k\|_{\mathbf{W}_k} + \alpha \|\mathbf{K}(\mathbf{D}_j) - \mathbf{K}(\bar{\mathbf{D}}_k)\| + (1 - \alpha) \|\mathbf{U}(\mathbf{D}_j) - \mathbf{U}(\bar{\mathbf{D}}_k)\|_F$$

where \mathbf{x}_j is the position of voxel j , $\bar{\mathbf{x}}_k$ is the centroid position of subnuclei k , \mathbf{W}_k is the covariance matrix of the voxels in subnuclei k (recalculated each iteration), α is a weighting factor to control the relative importance of tensor shape and orientation ($\alpha = 0.5$ (default)), \mathbf{D}_j is the diffusion tensor of voxel j , and $\bar{\mathbf{D}}_k$ is the mean diffusion tensor of subnuclei k . \mathbf{K} is a feature vector containing three tensor invariants that describe the shape of the diffusion tensor (size, anisotropy, and mode) and \mathbf{U} is a tensor that describes the primary orientation of the diffusion tensor (de Luis-García et al., 2009; de Luis-García et al., 2012). The Mahalanobis, Euclidean, and Frobenius norms were used to calculate the voxel position distance, the difference between the diffusion tensor invariants, and the difference between the diffusion tensor orientations, respectively. The k-means clustering algorithm calculated the position-tensor distance between

the centroid of each subnucleus and all other thalamic voxels. Each voxel was then assigned to a specific subnucleus based on minimization of the distance metric. This process was repeated until the convergence criterion was satisfied, defined as the point where no subnucleus centroid moved more than 0.1 mm from its previous iteration (Wiegell et al., 2003). The stability of the k-means clustering algorithm was evaluated across three randomly selected patients by performing thalamic segmentation 1000 times, each time randomly displacing the initial coordinates of each subnucleus centroid within a 2 mm-radius. The similarity between the subnuclei resulting from the default and randomized centroid initializations was then measured for each trial using the Dice coefficient.

Atlas-Independent, N-of-1 Tissue Activation Modeling

Three-dimensional finite element models (FEMs) incorporating individual brain anatomy, DBS lead position and orientation, anisotropic tissue conductivity, and clinical stimulation settings were created for each patient to calculate the spatial distribution of the DBS-induced electric field and estimate the VTA (22 FEMs total) (Astrom et al., 2009; Butson et al., 2007). VTAs associated with therapeutic outcome (tremor suppression) and side effects (sustained paresthesia and dysarthria/motor contraction) were calculated using an atlas-independent, n-of-1 tissue activation modeling approach (Chapter 2). The amount of VTA overlap with the motor and sensory regions of the thalamus was then measured to correlate motor and sensory thalamus stimulation with observed DBS outcomes. The DBS lead was modeled as a Medtronic 3387 lead with a contact length of 1.5 mm, contact spacing of 1.5 mm, and electrode diameter of 1.27 mm. An electric potential or current equal to the therapeutic or side effect-inducing stimulation amplitudes obtained from DBS programming was applied to the surface of the appropriate electrode contact (active contact). The previously calculated diffusion

tensors were converted to conductivity tensors via a linear transformation (Tuch et al., 2001) using MATLAB and then exported to COMSOL Multiphysics (5.2, COMSOL, Inc., Burlington, MA, USA), where they were interpolated onto the finite element mesh. The electric potential throughout the brain was solved for using the Poisson equation. The VTA was defined by the electric field norm, thresholded at 0.2 V/mm (Alonso et al., 2018; Astrom et al., 2015; Hemm et al., 2016). All simulations and VTA predictions were performed using COMSOL. VTAs were then exported to MATLAB, where their location relative to the segmented thalami was characterized for analysis.

Atlas-Based Thalamic Segmentation

Patient thalami were also segmented using an atlas-based approach to enable comparison with the n-of-1 thalamic segmentation results. The Morel thalamus was fitted to each patient thalamus to map the atlas subnuclei to the patient thalami. It was then determined which voxels of the patient thalami lay within each of the 13 subnuclei defined by the Morel thalamus. Said voxels were assigned to the appropriate subnucleus. For the dysarthria/motor contraction analysis, the Morel thalamus was simply fitted to each patient thalamus.

Statistical Analysis

Paired, two-sided (unless otherwise specified) Wilcoxon signed rank tests were used to determine if differences between the n-of-1 and atlas-based thalamic segmentation results were statistically significant. Wilcoxon signed rank tests were also used to determine if n-of-1 thalamic segmentation using the Hybrid distance generated results that differed significantly from those generated using alternative tensor distance metrics (Frobenius norm, J-divergence, and eigenvector angular difference) (Wang and Vemuri, 2004; Wiegell et al., 2003; Ziyani et al., 2006). Two-sided (unless otherwise specified) Wilcoxon rank sum tests (equivalent to Mann-

Whitney U-tests) were used to determine if stimulation location corresponding to therapeutic VTAs differed significantly from that corresponding to side effect-inducing VTAs. Chi-squared tests were used to evaluate the predictive capability of the n-of-1 and atlas-based segmentation approaches. All statistical analysis was performed using MATLAB. Significance was determined at a p-value of less than 0.05.

Results

Clinical Outcome

Twenty-two patients who underwent unilateral thalamic DBS for contralateral upper extremity tremor participated in this study (Table 3-1). A movement disorders neurologist (K.L.C.), blinded to the thalamic segmentation and tissue activation modeling results, independently programmed the stimulation and evaluated the clinical outcome for each patient during their postoperative monopolar review visit. Eighty-eight electrode contacts in total were tested. Fifty-four out of 88 electrode contacts (61%) were associated with side effects: 35/88 (40%) with sustained paresthesia, 15/88 (17%) with dysarthria, and 4/88 (5%) with motor contraction. The electrode contact that provided the greatest tremor control without side effects was selected as the therapeutic contact and recorded (Table 3-2). Therapeutic contacts had a mean stimulation amplitude of 1.7 ± 0.5 V for voltage-controlled DBS and 1.9 ± 0.5 mA for current-controlled DBS. Stimulation frequency and pulse width were set to 130 Hz and 60 μ s, respectively. All patients experienced improved tremor control with DBS.

Atlas-Independent, N-of-1 Thalamic Segmentation

Tensor Distance Metric

In addition to the Hybrid distance, three alternative tensor distance metrics were used to perform n-of-1 thalamic segmentation: the Frobenius norm, J-divergence, and eigenvector angular difference. The four tensor distance metrics were evaluated based on the location of therapeutic contacts in the segmented thalami and the amount of motor and sensory thalamus stimulation associated with therapeutic VTAs to determine which metric best described the clinical data (Figure 3-2). Therapeutic contacts were located in motor thalamus most often (11/22 patients) and sensory thalamus least often (6/22 patients) using the Hybrid distance. There was also significantly less sensory than motor thalamus stimulation for therapeutic VTAs using the Hybrid distance ($p < 0.05$, Wilcoxon signed rank test). Since motor thalamus was the intended DBS target and assuming that therapeutic VTAs are associated with minimal sensory thalamus stimulation, the Hybrid distance was determined to perform better than the other tensor distance metrics in terms of explaining therapeutic outcome.

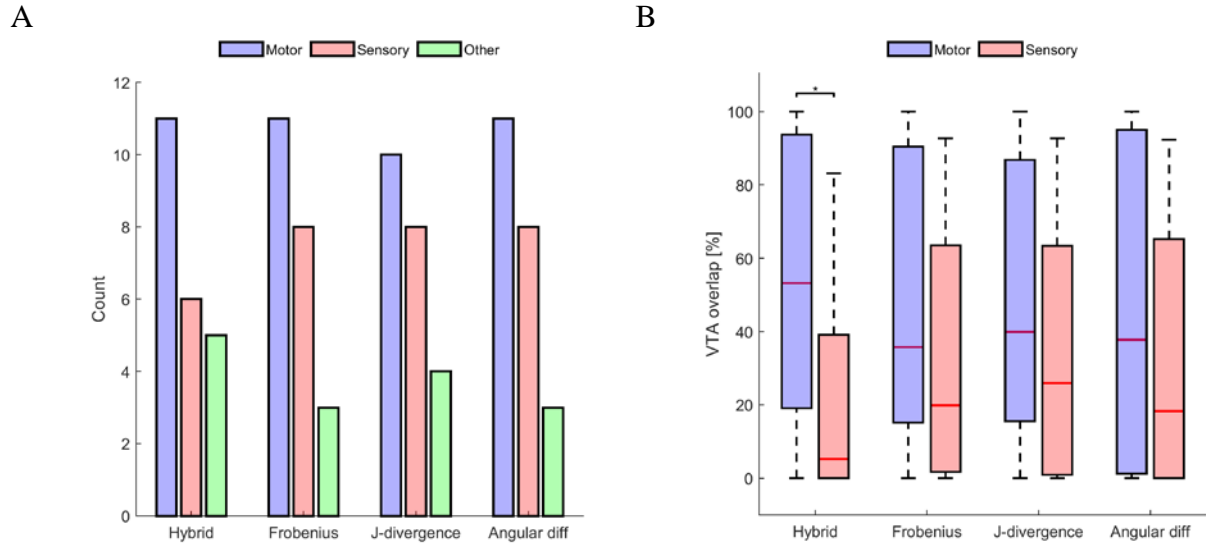


Figure 3-2 Comparison of tensor distance metrics for n-of-1 thalamic segmentation. (A) Location of therapeutic contacts in the segmented thalami. (B) Overlap of therapeutic VTAs with motor and sensory thalamus. * $p < 0.05$, Wilcoxon signed rank test. Motor thalamus consists of VL_a, VL_{pd}, and VL_{pv}; sensory thalamus consists of VPL and VPM; and other consists of the remaining eight subnuclei. Hybrid, Frobenius, and Angular diff correspond to the Hybrid distance, Frobenius norm, and eigenvector angular difference, respectively.

Stability of K-Means Clustering Algorithm

Overall, the k-means clustering algorithm was able to produce similar segmentations despite random displacement of the initial subnuclei centroid coordinates (Figure 3-3). The degree of similarity varied across the three patients and 13 subnuclei. Patient 2 had the most stable segmentation with a mean Dice coefficient between 0.68 and 0.98 across the 13 subnuclei. By comparison, Patient 3 had a mean Dice coefficient between 0.59 and 0.98, while Patient 1 had one between 0.48 and 0.89. Pulvinar (Pul) was the most stable subnucleus with a mean Dice coefficient between 0.89 and 0.98 across the three patients. In contrast, ventral anterior (VA) was the least stable subnucleus with a mean Dice coefficient between 0.52 and 0.81. For the subnuclei comprising motor (VL_a, VL_{pd}, and VL_{pv}) and sensory (VPL and VPM) thalamus, the mean Dice coefficient was between 0.59 and 0.87 across the three patients and five subnuclei.

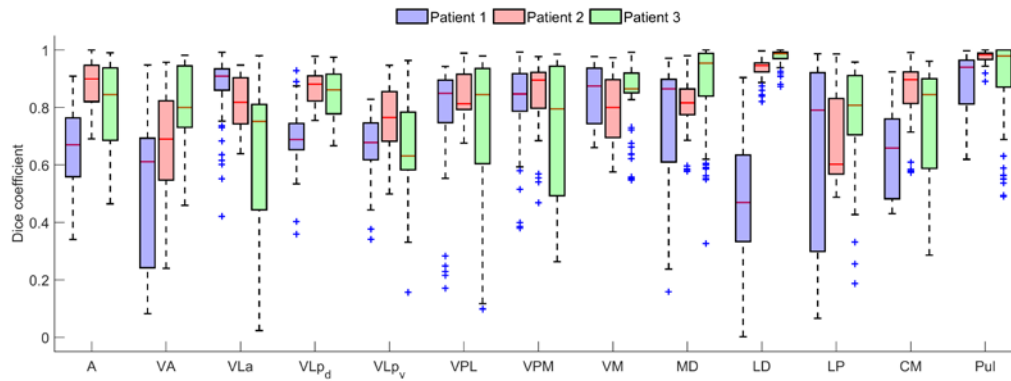


Figure 3-3 Stability analysis for n-of-1 thalamic segmentation. Similarity between subnuclei resulting from the default centroid initialization and those resulting from the randomized centroid initialization for three patients.

Comparison with Atlas-Based Thalamic Segmentation

Twenty-two individual thalami were segmented using the DT-based k-means clustering algorithm and an atlas-based approach. An example segmentation for one patient is shown in Figure 3-4. Thirteen subnuclei in total were identified: anterior (A); ventral anterior (VA); ventral lateral anterior (VL_a); ventral lateral posterior, dorsal part (VL_{pd}); ventral lateral posterior, ventral part (VL_{pv}); ventral posterior lateral (VPL), ventral posterior medial (VPM), ventromedial (VM), medial dorsal (MD), lateral dorsal (LD), lateral posterior (LP), centromedian (CM), and pulvinar (Pul). All subnuclei correspond to the nomenclature used in the Morel atlas.

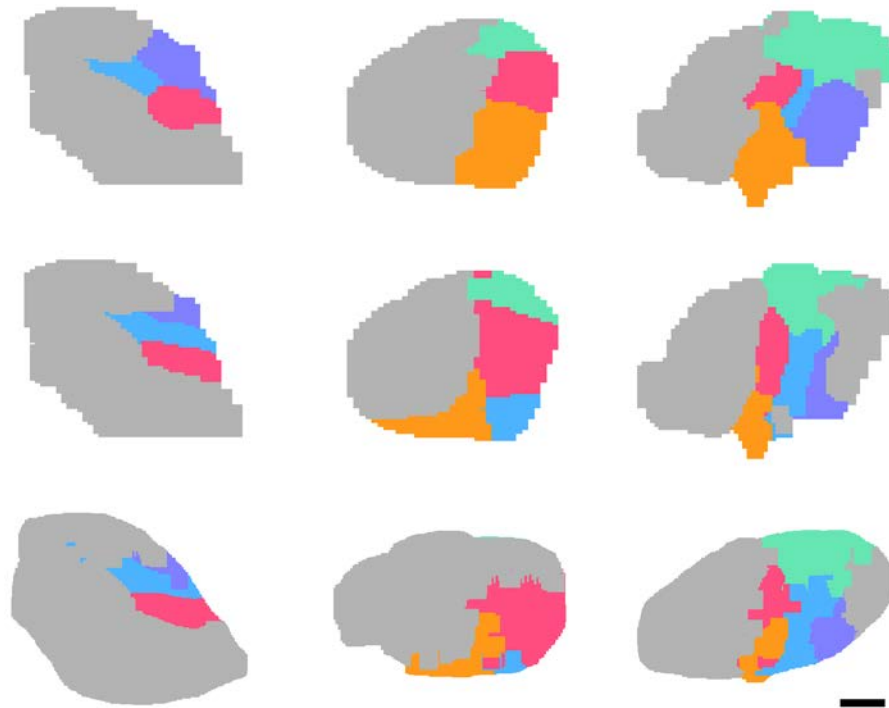


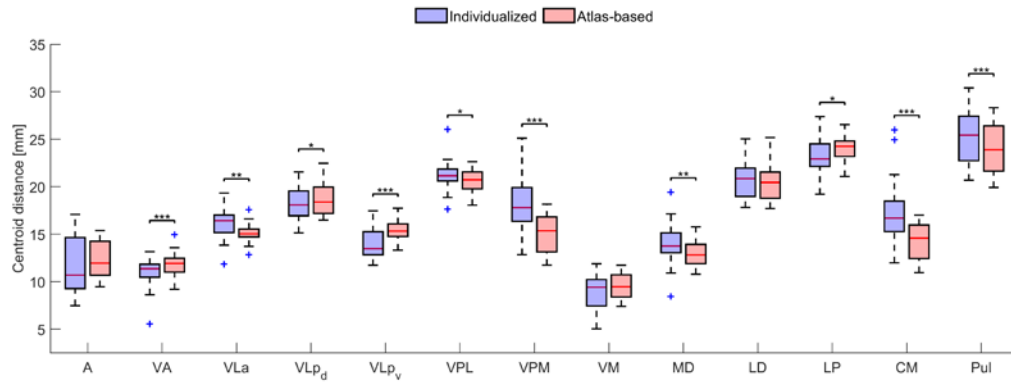
Figure 3-4 Comparison of n-of-1 and atlas-based thalamic segmentation for one patient. Top row: N-of-1 thalamic segmentation. Middle row: Atlas-based thalamic segmentation. Bottom row: Morel atlas. Motor thalamus, comprised of VLa, VLpd, and VLpv, and sensory thalamus, comprised of VPL and VPM, are shown in purple, green, blue, red, and orange, respectively. The rest of the thalamus is shown in gray. Axial, coronal, and sagittal views are displayed. The 2D slices in each column all correspond to the same level. Scale bar equals 5 mm.

Difference in Thalamic Anatomy

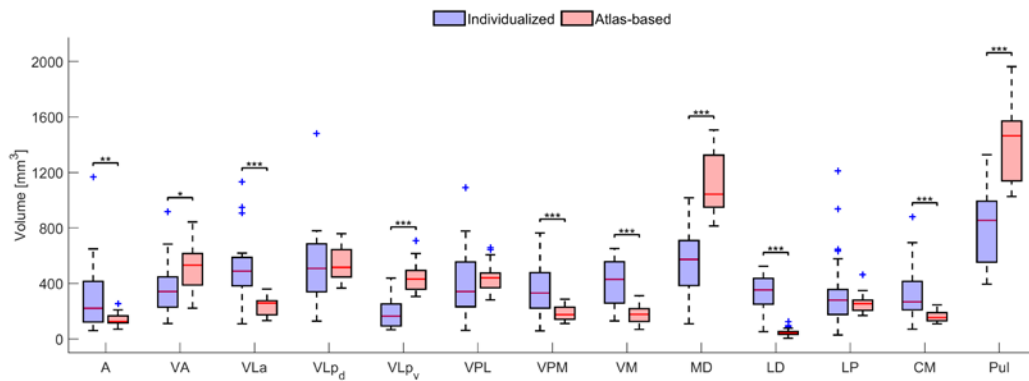
There were significant anatomical differences between n-of-1 and atlas-based thalamic segmentation in terms of subnucleus centroid distance (relative to the MCP) and volume (Figure 3-5). Ten out of 13 subnuclei (VA, VLa, VLpd, VLpv, VPL, VPM, MD, LP, CM, and Pul) had significantly different centroid distances between the two segmentation approaches ($p < 0.05$, Wilcoxon signed rank test). The mean absolute difference between the centroid distances from n-of-1 thalamic segmentation and those from atlas-based thalamic segmentation ranged from 0.9 to 2.9 mm across the 13 subnuclei. Along each direction, the mean absolute difference ranged from

0.6 to 2.8 mm (lateral-medial), 0.7 to 3.6 mm (anterior-posterior), and 0.5 to 3.0 mm (dorsal-ventral). For VLpv, the atlas subnucleus that best corresponds to the VIM DBS target, the mean absolute difference was 1.7 mm. Ten out of 13 subnuclei (A, VA, VL_a, VL_{pv}, VPM, VM, MD, LD, CM, and Pul) also had significantly different volumes between the two segmentation approaches ($p < 0.05$, Wilcoxon signed rank test). Four of those 10 subnuclei, including VL_{pv}, were significantly smaller using n-of-1 compared to atlas-based thalamic segmentation.

A



B



C

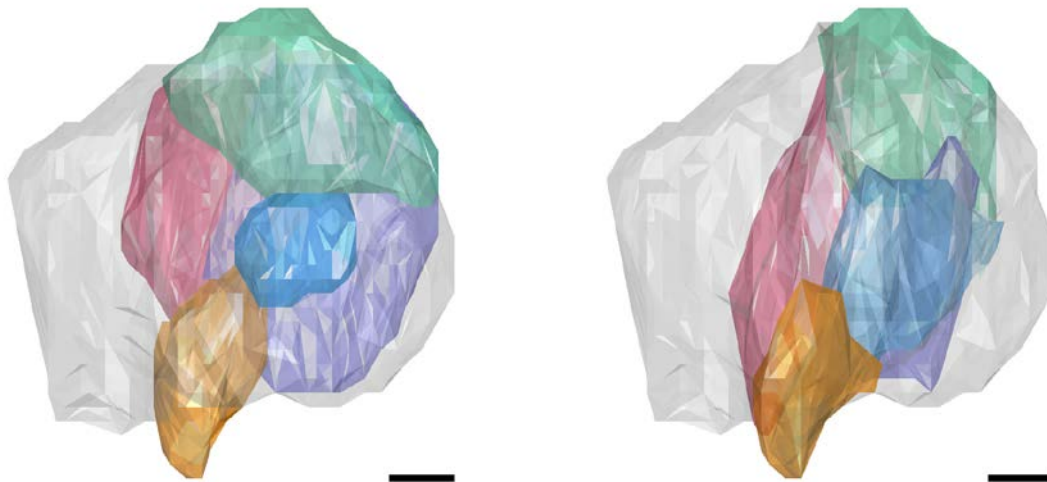


Figure 3-5 Difference in subnuclei location and size between n-of-1 and atlas-based thalamic segmentation. (A) Centroid distance (relative to the MCP). (B) Volume. * $p < 0.05$, ** $p < 0.01$, and *** $p < 0.001$, Wilcoxon signed rank test. (C) Example of n-of-1 (left) and atlas-based (right) thalamic segmentation for one patient. VLd, VLpd, and VLpv (motor thalamus) are shown in purple, green, and blue, respectively; VPL and VPM (sensory thalamus) are shown in red and orange, respectively. A sagittal view is displayed. Scale bars equal 5 mm.

Difference in Therapeutic Contact Location

There were also significant differences in therapeutic contact location between n-of-1 and atlas-based thalamic segmentation (Figure 3-6). Using n-of-1 thalamic segmentation, 11/22 therapeutic contacts (50%) were located in motor thalamus, defined as the union of VL_a, VL_{pd}, and VL_{pv}. The mean therapeutic contact was located 13.7 ± 1.6 mm lateral, 5.5 ± 2.3 mm posterior, and 3.9 ± 2.6 mm dorsal to the MCP, while the mean VL_{pv} centroid was located 11.0 ± 1.4 mm lateral, 4.8 ± 2.4 mm posterior, and 6.3 ± 1.9 mm dorsal. On average, the therapeutic contact was located 2.7 ± 1.9 mm lateral, 0.7 ± 2.9 mm posterior, and 2.3 ± 3.0 mm ventral to the VL_{pv} centroid, which equated to a Euclidean distance of 5.6 ± 1.7 mm between the two points. In contrast, 19/22 therapeutic contacts (86%) were located in motor thalamus using atlas-based thalamic segmentation. The mean VL_{pv} centroid was located 13.5 ± 1.0 mm lateral, 5.3 ± 1.6 mm posterior, and 4.5 ± 1.1 mm dorsal to the MCP. On average, the therapeutic contact was located 0.2 ± 1.6 mm lateral, 0.2 ± 2.6 mm posterior, and 0.6 ± 2.7 mm ventral to the VL_{pv} centroid, which equated to a Euclidean distance of 3.7 ± 1.6 mm between the two points. The distance from the therapeutic contact to the VL_{pv} centroid differed significantly in the lateral-medial and dorsal-ventral directions between the two segmentation approaches ($p < 0.001$, Wilcoxon signed rank test), but not in the anterior-posterior direction.

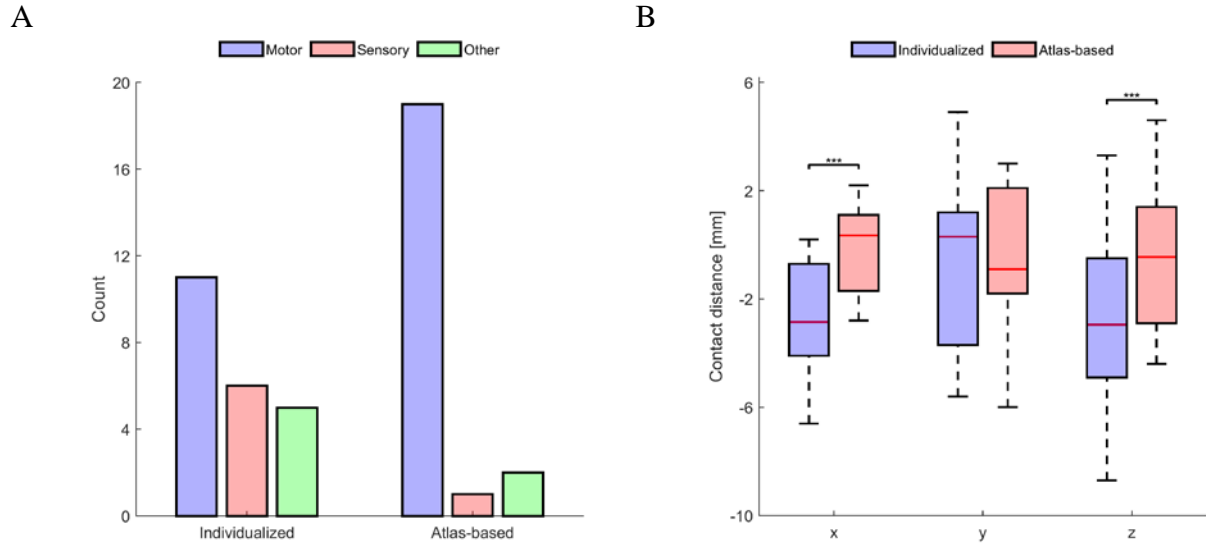


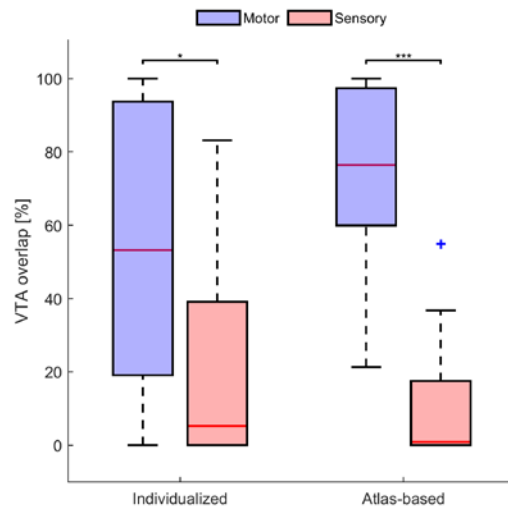
Figure 3-6 Difference in therapeutic contact location between n-of-1 and atlas-based thalamic segmentation. (A) Location of therapeutic contacts in the segmented thalami. Motor thalamus consists of VLa, VLpd, and VLpv; sensory thalamus consists of VPL and VPM; and other consists of the remaining eight subnuclei. (B) Therapeutic contact distance (relative to the VLpv centroid). Positive x, y, and z correspond to the lateral, anterior, and dorsal directions, respectively. *** $p < 0.001$, Wilcoxon signed rank test.

Difference in VTA Location and Predictive Capability

Using n-of-1 thalamic segmentation, 20/22 VTAs associated with therapeutic outcome (91%) overlapped with motor thalamus despite only 50% of the therapeutic contacts being located in the subnuclei comprising the structure, while 14/22 therapeutic VTAs (64%) overlapped with sensory thalamus, defined as the union of VPL and VPM. Fifteen out of 22 therapeutic VTAs (68%) overlapped more with motor than sensory thalamus. In contrast, 22/22 therapeutic VTAs (100%) overlapped with motor thalamus using atlas-based thalamic segmentation, while 11/22 therapeutic VTAs (50%) overlapped with sensory thalamus. Twenty out of 22 therapeutic VTAs (91%) overlapped more with motor than sensory thalamus. There was a significant difference in the amount of therapeutic VTA overlap with motor thalamus between n-of-1 and atlas-based thalamic segmentation ($p < 0.01$, Wilcoxon signed rank test), as well as with sensory thalamus ($p < 0.05$, Wilcoxon signed rank test). However, both

segmentation approaches showed that therapeutic VTAs had significantly more overlap with motor than sensory thalamus ($p < 0.05$, Wilcoxon signed rank test) (Figure 3-7). Still, some patients had large discrepancies between their n-of-1 and atlas-based thalamic segmentation results. Figure 3-7B shows one patient whose n-of-1 thalamic segmentation results more accurately reflect their therapeutic outcome based on the location of the VTA than their atlas-based thalamic segmentation results. The n-of-1 thalamic segmentation results show the therapeutic VTA contained within motor thalamus. In contrast, the atlas-based thalamic segmentation results show most of the therapeutic VTA spreading to sensory thalamus.

A



B

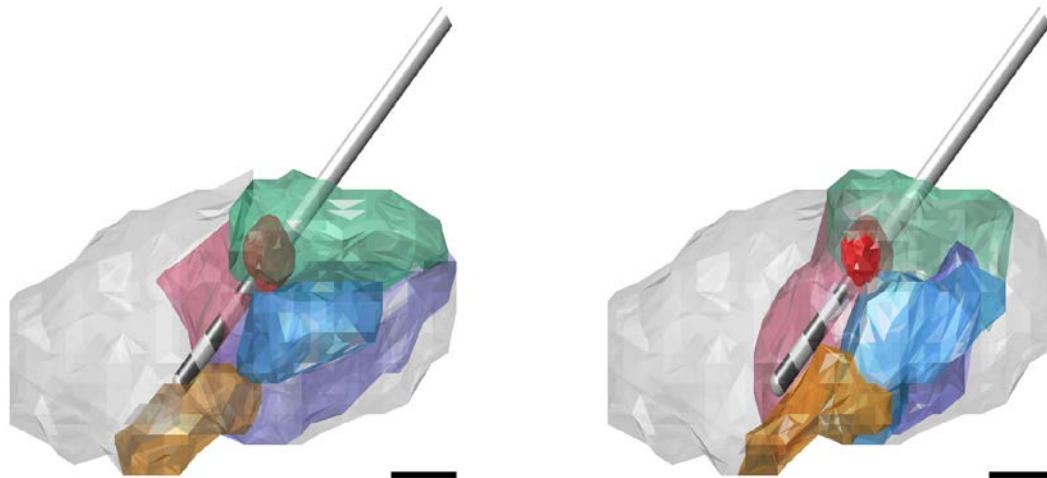
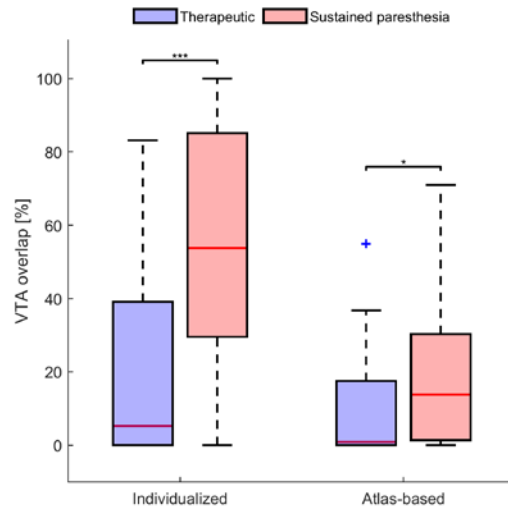


Figure 3-7 Difference in the amount of motor and sensory thalamus stimulation associated with therapeutic VTAs between n-of-1 and atlas-based thalamic segmentation. (A) Overlap of therapeutic VTAs with motor and sensory thalamus. Motor thalamus consists of VLa, VLpd, and VLpv; sensory thalamus consists of VPL and VPM. * $p < 0.05$ and *** $p < 0.001$, Wilcoxon signed rank test. (B) Example of n-of-1 (left) and atlas-based (right) thalamic segmentation for one patient. VLa, VLpd, VLpv, VPL, and VPM are shown in purple, green, blue, red, and orange, respectively. The therapeutic VTA is shown in dark red, DBS lead is shown in gray, and electrode contacts are shown in dark gray. A sagittal view is displayed. Scale bars equal 5 mm.

The VTA analysis was then repeated for VTAs associated with side effects, specifically sustained paresthesia and dysarthria/motor contraction. Using n-of-1 thalamic segmentation, 33/35 sustained paresthesia VTAs (94%) overlapped with sensory thalamus. In contrast, 26/35

sustained paresthesia VTAs (74%) overlapped with sensory thalamus using atlas-based thalamic segmentation. There was a significant difference in the amount of sensory thalamus stimulation between n-of-1 and atlas-based thalamic segmentation for sustained paresthesia VTAs ($p < 0.001$, Wilcoxon signed rank test). However, both segmentation approaches showed that sustained paresthesia VTAs had significantly more overlap with sensory thalamus than therapeutic VTAs ($p < 0.05$, Mann-Whitney U-test) (Figure 3-8). Again, some patients had large discrepancies between their n-of-1 and atlas-based thalamic segmentation results. Figure 3-8B shows one patient whose n-of-1 thalamic segmentation results more accurately reflect their sustained paresthesia outcome based on the location of the VTA than their atlas-based thalamic segmentation results. The n-of-1 thalamic segmentation results show the sustained paresthesia VTA contained within sensory thalamus. In contrast, the atlas-based thalamic segmentation results show little of the sustained paresthesia VTA spreading to sensory thalamus. When VTA overlap with sensory thalamus was treated as a binary variable for therapeutic and sustained paresthesia VTAs, there was a statistically significant relationship between sensory thalamus stimulation and sustained paresthesia for n-of-1 thalamic segmentation ($p < 0.05$, chi-squared test), but not for atlas-based thalamic segmentation.

A



B

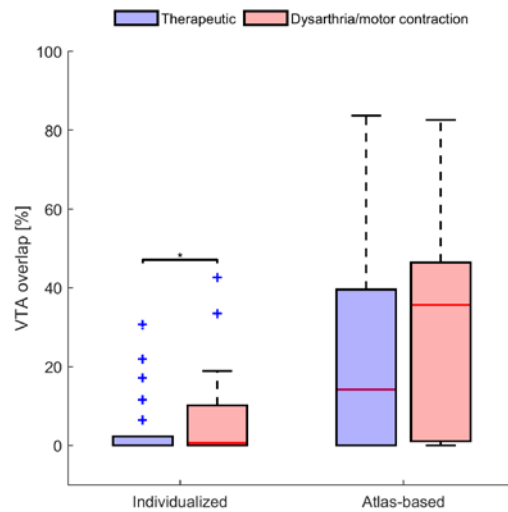


Figure 3-8 Difference in the amount of sensory thalamus stimulation associated with therapeutic and sustained paresthesia VTAs between n-of-1 and atlas-based thalamic segmentation. (A) Overlap of therapeutic and sustained paresthesia VTAs with sensory thalamus. Sensory thalamus consists of VPL and VPM. * $p < 0.05$ and *** $p < 0.001$, Mann-Whitney U-test. (B) Example of n-of-1 (left) and atlas-based (right) thalamic segmentation for one patient. VLa, VLpd, VLpv, VPL, and VPM are shown in purple, green, blue, red, and orange, respectively. The sustained paresthesia VTA is shown in dark red, DBS lead is shown in gray, and electrode contacts are shown in dark gray. A sagittal view is displayed. Scale bars equal 5 mm.

Using n-of-1 thalamic segmentation, 13/19 dysarthria/motor contraction VTAs (68%) spread outside of the thalamus. In contrast, 15/19 dysarthria/motor contraction VTAs (79%) spread outside of the thalamus using atlas-based thalamic segmentation. There was a significant

difference in the amount of external stimulation spreading laterally (a proxy for internal capsule stimulation) between n-of-1 and atlas-based thalamic segmentation for dysarthria/motor contraction VTAs ($p < 0.001$, Wilcoxon signed rank test), which may explain why only n-of-1 thalamic segmentation showed that dysarthria/motor contraction VTAs had significantly more external stimulation than therapeutic VTAs ($p < 0.05$, Mann-Whitney U-test, one-sided) (Figure 3-9). Again, some patients had large discrepancies between their n-of-1 and atlas-based thalamic segmentation results. Figure 3-9B shows one patient whose n-of-1 thalamic segmentation results more accurately reflect their dysarthria/motor contraction and therapeutic outcomes based on the location of the VTA than their atlas-based thalamic segmentation results. The n-of-1 thalamic segmentation results show a clear difference in the amount of external stimulation associated with dysarthria/motor contraction and therapeutic VTAs. In contrast, the atlas-based thalamic segmentation results show a more subtle difference. When external stimulation was treated as a binary variable for therapeutic and dysarthria/motor contraction VTAs, there was a statistically significant relationship between external stimulation and dysarthria/motor contraction for n-of-1 thalamic segmentation ($p < 0.05$, chi-squared test), but not for atlas-based thalamic segmentation.

A



B

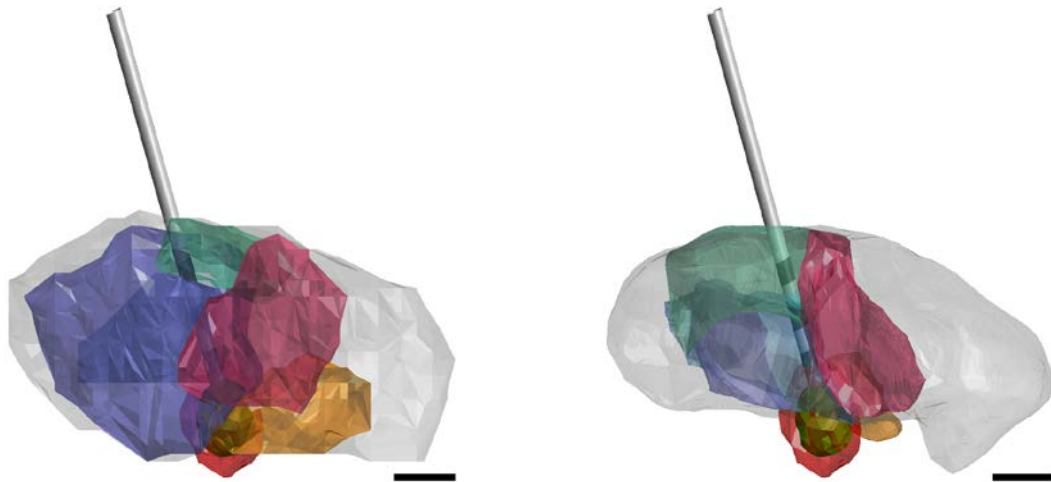


Figure 3-9 Difference in the amount of external stimulation associated with therapeutic and dysarthria/motor contraction VTAs between n-of-1 and atlas-based thalamic segmentation. (A) Overlap of therapeutic and dysarthria/motor contraction VTAs with external thalamus. * $p < 0.05$, Mann-Whitney U-test, one-sided. (B) Example of n-of-1 (left) and atlas-based (right) thalamic segmentation for one patient. VL_a, VL_{pd}, VL_{pv}, VPL, and VPM are shown in purple, green, blue, red, and orange, respectively. The dysarthria/motor contraction VTA is shown in dark red, therapeutic VTA is shown in dark green, DBS lead is shown in gray, and electrode contacts are shown in dark gray. A sagittal view is displayed. Scale bars equal 5 mm.

Discussion

Deep brain stimulation targeting the VIM nucleus of the thalamus (equivalent to the VL_{pv} subnucleus from the Morel atlas) is the primary neurosurgical therapy to treat idiopathic

ET (Benabid et al., 1996; Deuschl et al., 2011; Pahwa et al., 2006). Despite the effectiveness of thalamic DBS, the optimal locus of stimulation and the mechanisms underlying tremor relief remain uncertain (Phibbs et al., 2014; Sandvik et al., 2012; Udupa and Chen, 2015). At present, thalamic DBS appears to favorably modulate pathological cerebellar outflow signals that produce tremor (Gibson et al., 2016). Substantial progress has been made towards improving clinical outcomes for patients receiving thalamic DBS. However, multiple factors still hamper scientific advances, including highly variable thalamic anatomy across animal and human subjects, and neuroimaging limitations for thalamic visualization and DBS targeting. In this study, a novel methodology to evaluate the clinical effects of thalamic DBS is presented – one that combines atlas-independent thalamic segmentation and tissue activation modeling using individual 3 T DT imaging data obtained from 22 patients with ET who received unilateral thalamic DBS. To date, DBS-induced tissue activation has been difficult to investigate within the context of ET because of the challenges associated with visualizing and differentiating the individual subnuclei of the thalamus. To address these challenges, a DT-based k-means clustering algorithm was used to segment individual thalamic subnuclei. The thalamic segmentation results were then combined with finite element computational models of the VTA induced by DBS. Tissue activation volumes associated with therapeutic outcome (tremor suppression) and side effects (sustained paresthesia and dysarthria/motor contraction) were calculated using a truly n-of-1 VTA modeling approach (Chapter 2). The amount of VTA overlap with the motor and sensory regions of the thalamus was then measured to correlate motor and sensory thalamus stimulation with observed outcomes. The results obtained using n-of-1 thalamic segmentation were compared with those obtained using an atlas-based thalamic segmentation approach to further assess the methodology. To the best of our knowledge, this

study is the first to clinically validate an atlas-independent, n-of-1 thalamic segmentation and tissue activation modeling methodology to improve thalamic DBS on an individual patient basis.

Thalamic Segmentation

Direct segmentation of the individual patient thalamus offers an attractive strategy to improve DBS targeting. If individual thalamic subnuclei were accurately identified, the optimal locus of stimulation could be defined and targeted in a straightforward manner. In the past, thalamic segmentation was approximated with standardized stereotactic atlases, which assume a fixed relative position and shape among thalamic subnuclei (Forutan et al., 2015; Lemaire et al., 2010; Morel et al., 1997; Schaltenbrand et al., 1977). More recently, thalamic segmentation algorithms have included linear and non-linear atlas fitting (Phibbs et al., 2014), manual contouring (Zerroug et al., 2016), high-field strength MR imaging (Abosch et al., 2010; Duchin et al., 2012; Kanowski et al., 2014; Tourdias et al., 2014; Xiao et al., 2016), and DT imaging (Akram et al., 2018; Deoni et al., 2007; Johansen-Berg et al., 2005; Lambert et al., 2017; Wiegell et al., 2003).

A previously published k-means clustering algorithm for semi-automatic thalamic segmentation (Wiegell et al., 2003) was refined to evaluate stimulation location and clinical outcomes in individual patients. The k-means clustering algorithm used DT imaging data to segment the thalamus into a predefined number of subnuclei (clusters). Wiegell et al. obtained convincing results using the Frobenius norm as a tensor dissimilarity measure. Building on this foundation, the Frobenius norm, along with three alternative tensor distance metrics: Hybrid distance (de Luis-García et al., 2009), J-divergence (Wang and Vemuri, 2004), and eigenvector angular difference (Ziyan et al., 2006), was assessed based on the location of therapeutic electrode contacts in the segmented thalami and the amount of motor and sensory thalamus

stimulation associated with therapeutic VTAs (Figure 3-2). The Hybrid distance was ultimately chosen over the other tensor distance metrics for n-of-1 thalamic segmentation because it performed best in terms of explaining therapeutic outcome. This finding is consistent with results obtained by de Luis-García et al., who reported that the Hybrid distance performed better than other traditional tensor distance metrics for white matter segmentation (de Luis-García et al., 2012). The stability of the modified k-means clustering algorithm was evaluated by segmenting the thalami of three randomly selected patients 1000 times, each time randomly displacing the initial coordinates of each subnucleus centroid within a 2 mm-radius. The similarity between the subnuclei resulting from the default and randomized centroid initializations was then measured for each trial using the Dice coefficient. Overall, the modified k-means clustering algorithm produced similar segmentations despite random displacement of the initial subnuclei centroid coordinates (Figure 3-3). For the subnuclei comprising motor (VLa, VLpd, and VLpv) and sensory (VPL and VPM) thalamus, the mean Dice coefficient ranged from 0.59 to 0.87 across the three patients and five subnuclei. For comparison, the similarity between thalami obtained from the widely used Morel (Morel et al., 1997) and Mai (Forutan et al., 2015) atlases was also measured. After fitting the atlas thalami to one another via transposition and scaling, the Dice coefficient ranged from 0.01 to 0.68 across 10 equivalent subnuclei. The Morel atlas was ultimately chosen over the Mai atlas because of its use in previous thalamic segmentation studies utilizing k-means clustering (Deoni et al., 2007; Wiegell et al., 2003).

Thalami from 22 individual patients were segmented using the modified, DT-based k-means clustering algorithm and an atlas-based approach. Thirteen subnuclei in total were identified. The subnuclei centroids were initialized by placing them at locations corresponding to the Morel atlas (Deoni et al., 2007). Compared to other centroid initialization schemes, doing this

dramatically reduced the algorithm run time and improved the segmentation results. There were significant anatomical differences between n-of-1 and atlas-based thalamic segmentation in terms of subnucleus centroid distance (relative to the MCP) and volume (Figure 3-5). Ten out of 13 subnuclei had significantly different centroid distances and volumes between the two segmentation approaches. The mean absolute difference between the centroid distances from n-of-1 thalamic segmentation and those from atlas-based thalamic segmentation ranged from 0.9 to 2.9 mm across the 13 subnuclei. Along each direction, the mean absolute difference ranged from 0.6 to 2.8 mm (lateral-medial), 0.7 to 3.6 mm (anterior-posterior), and 0.5 to 3.0 mm (dorsal-ventral). These findings are consistent with results obtained by Deoni et al., who reported an absolute difference of 3.3 mm between their final subnuclei centroid locations and those from the Morel atlas (after registering their segmentation results to the atlas) (Deoni et al., 2007). Along each direction, they reported absolute differences of 2.2 mm (lateral-medial), 1.7 mm (anterior-posterior), and 1.3 mm (dorsal-ventral). It is important to note that atlas-based subnuclei centroid locations, while representative of a general population, are not true comparisons on an individual patient basis. High variability in thalamic size/shape and subnuclear boundaries is expected (and was observed) across individual patients (Akram et al., 2018; Behrens et al., 2003; Johansen-Berg et al., 2005; Lambert et al., 2017). Without a ground truth thalamic segmentation to measure against, it is difficult to determine which segmentation approach is better based on anatomical differences alone.

Therapeutic Contact Localization

N-of-1 thalamic segmentation enabled atlas-independent localization of therapeutic electrode contacts in patient thalami. Fifty percent of the therapeutic contacts were located in motor thalamus, defined as the union of VL_a, VL_{pd}, and VL_{pv}. On average, the therapeutic

contact was located lateral, posterior, and ventral to the VLpv centroid, 5.6 ± 1.7 mm away (Euclidean distance). In contrast, 86% of the therapeutic contacts were located in motor thalamus using atlas-based thalamic segmentation. On average, the therapeutic contact was located lateral, posterior, and ventral to the VLpv centroid, 3.7 ± 1.6 mm away. The distance from the therapeutic contact to the VLpv centroid differed significantly in the lateral-medial and dorsal-ventral directions between the two segmentation approaches, but not in the anterior-posterior direction. Although therapeutic contacts were located in motor thalamus more often using atlas-based thalamic segmentation, active contact position is not an accurate measure of stimulation location. This is because stimulation is not concentrated at a single point in space. Rather, when stimulation is applied by the active contact, an electric field is induced in the brain tissue that spreads outward in all directions. Previous studies have highlighted the need for a more detailed identification of stimulation location relative to DBS targets, one that goes beyond simple active contact position (Caire et al., 2013; Nestor et al., 2014). Some therapeutic contacts were also located near the border between motor and sensory thalamus, which shows the limitation of using a single point to classify its location.

Tissue Activation Modeling

The VTA is a more accurate characterization of stimulation location in the brain than active contact position and it can provide possible explanations for the regional effects of DBS at sites beyond the electrode contact surface. Tissue activation volume analysis has been useful in explaining the therapeutic and side effects of DBS (Astrom et al., 2010; Chaturvedi et al., 2010; Dembek et al., 2017). Conductive and dielectrical isotropy is a common assumption in VTA modeling studies, as computationally manageable spherical regions of activation result from this approximation (Dembek et al., 2017; Kuncel et al., 2008). However, the electrical complexity

introduced by incorporating anisotropy into computational models of DBS likely has one of the most prominent impacts on the accuracy of VTA predictions (Hauelsen et al., 2002; Howell and McIntyre, 2016).

Thalamic segmentation results were combined with VTAs modeled using an atlas-independent, n-of-1 approach (Chapter 2). Within the thalamus, the shape and size of the VTA was highly variable across individual patients, likely due to differences in active contact position and local anisotropic tissue properties. VTAs ranged in appearance from spherical to elongate. They also varied considerably in size, even for patients with similar stimulation parameters. Using n-of-1 thalamic segmentation, 91% of the VTAs associated with therapeutic outcome overlapped with motor thalamus despite only 50% of the therapeutic contacts being located in the subnuclei comprising the structure. Also, 68% of the therapeutic VTAs overlapped more with motor than sensory thalamus, defined as the union of VPL and VPM. In contrast, 100% of the therapeutic VTAs overlapped with motor thalamus using atlas-based thalamic segmentation, while 91% overlapped more with motor than sensory thalamus. Although atlas-based thalamic segmentation performed better overall in explaining therapeutic outcome, both segmentation approaches showed that therapeutic VTAs had significantly more overlap with motor than sensory thalamus (Figure 3-7A). These findings are consistent with results obtained by Kuncel et al., who reported that placement of the active contact in the posterior part of the VIM can cause stimulation of the VPL (Kuncel et al., 2008). It is important to note that for some patients, their n-of-1 thalamic segmentation results more accurately reflected their therapeutic outcome based on the location of the VTA (Figure 3-7B). The strength of n-of-1 thalamic segmentation is most apparent in these specific cases, where the thalamic anatomy of the patient differs considerably in size and shape from the atlas thalamus.

Tissue activation volume analysis was repeated for VTAs associated with side effects, specifically sustained paresthesia and dysarthria/motor contraction. The border between motor and sensory thalamus is commonly assumed to modulate the incidence of sustained paresthesia from stimulation (Keane et al., 2012; Kuncel et al., 2008; Pouratian et al., 2011). Using n-of-1 thalamic segmentation, 94% of the sustained paresthesia VTAs overlapped with sensory thalamus. In contrast, 74% of the sustained paresthesia VTAs overlapped with sensory thalamus using atlas-based thalamic segmentation. N-of-1 thalamic segmentation performed better overall in explaining sustained paresthesia. For example, Figure 3-8B shows a sustained paresthesia VTA contained within sensory thalamus using n-of-1 thalamic segmentation. In contrast, atlas-based thalamic segmentation shows little of the sustained paresthesia VTA spreading to sensory thalamus. Still, both segmentation approaches showed that sustained paresthesia VTAs had significantly more overlap with sensory thalamus than therapeutic VTAs (Figure 3-8A). However, when VTA overlap with sensory thalamus was treated as a binary variable for therapeutic and sustained paresthesia VTAs, there was a statistically significant relationship between sensory thalamus stimulation and sustained paresthesia for n-of-1 thalamic segmentation, but not for atlas-based thalamic segmentation. Using n-of-1 thalamic segmentation, 68% of the dysarthria/motor contraction VTAs spread outside of the thalamus. In contrast, 79% of the dysarthria/motor contraction VTAs spread outside of the thalamus using atlas-based thalamic segmentation. There was a significant difference in the amount of external stimulation spreading laterally (a proxy for internal capsule stimulation) between the two segmentation approaches for dysarthria/motor contraction VTAs, which may explain why only n-of-1 thalamic segmentation showed that dysarthria/motor contraction VTAs had significantly more external stimulation than therapeutic VTAs (Figure 3-9A). For example, Figure 3-9B

shows a clear difference in the amount of external stimulation associated with dysarthria/motor contraction and therapeutic VTAs using n-of-1 thalamic segmentation. In contrast, atlas-based thalamic segmentation shows a more subtle difference. When external stimulation was treated as a binary variable for therapeutic and dysarthria/motor contraction VTAs, there was a statistically significant relationship between external stimulation and dysarthria/motor contraction for n-of-1 thalamic segmentation, but not for atlas-based thalamic segmentation. These findings for paresthesia and dysarthria/motor contraction VTAs suggest that n-of-1 thalamic segmentation performs better than atlas-based thalamic segmentation in explaining DBS side effects (has greater predictive capability).

Limitations, Alternative Approaches, and Future Directions

The primary limitation of this study comes from the unavailability of histological data to evaluate the thalamic segmentations generated by the modified, DT-based k-means clustering algorithm. Historically, the identification and naming of thalamic subnuclei have been a subject of active study and debate (Macchi and Jones, 1997; Percheron et al., 1996). Stereotactic atlases were produced to provide a generalized template for thalamic and other subcortical targeting (Hamani et al., 2006). With the recognition that individual anatomic variability can be substantial across specimens used for axial, coronal, and sagittal sections (Niemann and van Nieuwenhofen, 1999), efforts were made to produce internally consistent atlases, such as the Morel atlas used in this study. Another limitation is the resolution of the DT imaging, which is lower than that of the MR and CT imaging. Acquiring higher resolution DT imaging by modifying the imaging protocol would address this limitation, but would likely require patients to undergo longer scan times. Lastly, since multiple imaging modalities were required to create the models for each patient, image registration error is another limitation to consider. Image registration was

performed using commercial software for visualizing and analyzing medical imaging to minimize error between the pre- and post-operative imaging data. All registrations were carefully done and evaluated by the same individual. If deemed necessary by visual inspection, manual refinements were made to ensure an accurate registration. The presented methodology utilized k-means clustering as a proxy for local histological analysis. Individual patient thalami were segmented based on voxel geometric proximity and diffusion tensor similarity. Each voxel was assigned to its respective subnucleus independent of adjacent voxel properties. As an alternative approach, 7 T field strength MR imaging has been used to identify thalamic subnuclei and other subcortical structures (Abosch et al., 2010; Xiao et al., 2016). Other strategies have used measures of diffusivity, such as functional connectivity and tractography, to segment the thalamus (Akram et al., 2018; Behrens et al., 2003; Elias et al., 2012; Lambert et al., 2017). Such approaches have also been applied to DBS targeting (Akram et al., 2018; Coenen et al., 2014; Kim et al., 2016). The combination of atlas-independent thalamic segmentation and tissue activation modeling presented here, assessed by therapeutic outcome and DBS programming, provides a detailed explanation of clinical outcome on an individual patient basis. Future work incorporating alternative strategies for segmenting the thalamus or examining the therapeutic and side effects of thalamic DBS in a larger population of patients may further improve the n-of-1 thalamic segmentation algorithm.

Conclusion

This study presents a novel modeling methodology that combines atlas-independent thalamic segmentation and tissue activation modeling to evaluate the clinical effects of thalamic DBS on an individual patient basis. While traditional atlas-based thalamic segmentation and VTA modeling are reliable tools for general DBS planning and mechanistic study, enhanced

accuracy at the individual patient level may be possible with atlas-independent, truly n-of-1 modeling approaches utilizing DT imaging data.

References

- Abosch, A., Yacoub, E., Ugurbil, K., Harel, N., 2010. An assessment of current brain targets for deep brain stimulation surgery with susceptibility-weighted imaging at 7 tesla. *Neurosurgery* 67, 1745-1756; discussion 1756.
- Akram, H., Dayal, V., Mahlknecht, P., Georgiev, D., Hyam, J., Foltynie, T., Limousin, P., De Vita, E., Jahanshahi, M., Ashburner, J., Behrens, T., Hariz, M., Zrinzo, L., 2018. Connectivity derived thalamic segmentation in deep brain stimulation for tremor. *Neuroimage Clin* 18, 130-142.
- Alonso, F., Vogel, D., Johansson, J., Wardell, K., Hemm, S., 2018. Electric Field Comparison between Microelectrode Recording and Deep Brain Stimulation Systems-A Simulation Study. *Brain Sci* 8.
- Astrom, M., Diczfalusy, E., Martens, H., Wardell, K., 2015. Relationship between neural activation and electric field distribution during deep brain stimulation. *IEEE Trans Biomed Eng* 62, 664-672.
- Astrom, M., Tripoliti, E., Hariz, M.I., Zrinzo, L.U., Martinez-Torres, I., Limousin, P., Wardell, K., 2010. Patient-specific model-based investigation of speech intelligibility and movement during deep brain stimulation. *Stereotact Funct Neurosurg* 88, 224-233.
- Astrom, M., Zrinzo, L.U., Tisch, S., Tripoliti, E., Hariz, M.I., Wardell, K., 2009. Method for patient-specific finite element modeling and simulation of deep brain stimulation. *Med Biol Eng Comput* 47, 21-28.
- Battistella, G., Najdenovska, E., Maeder, P., Ghazaleh, N., Daducci, A., Thiran, J.P., Jacquemont, S., Tuleasca, C., Levivier, M., Bach Cuadra, M., Fornari, E., 2017. Robust thalamic nuclei segmentation method based on local diffusion magnetic resonance properties. *Brain Struct Funct* 222, 2203-2216.
- Behrens, T.E., Johansen-Berg, H., Woolrich, M.W., Smith, S.M., Wheeler-Kingshott, C.A., Boulby, P.A., Barker, G.J., Sillery, E.L., Sheehan, K., Ciccarelli, O., Thompson, A.J., Brady, J.M., Matthews, P.M., 2003. Non-invasive mapping of connections between human thalamus and cortex using diffusion imaging. *Nat Neurosci* 6, 750-757.
- Benabid, A.L., Pollak, P., Gao, D., Hoffmann, D., Limousin, P., Gay, E., Payen, I., Benazzouz, A., 1996. Chronic electrical stimulation of the ventralis intermedius nucleus of the thalamus as a treatment of movement disorders. *J Neurosurg* 84, 203-214.
- Bentley, J.N., Guan, Z., Cummings, K.S., Chou, K.L., Patil, P.G., 2017. Influence of Intracranial Air on Electrode Position and Clinical Outcomes following Deep Brain Stimulation for Parkinson's Disease. *Stereotact Funct Neurosurg* 95, 6-12.
- Butson, C.R., Cooper, S.E., Henderson, J.M., McIntyre, C.C., 2007. Patient-specific analysis of the volume of tissue activated during deep brain stimulation. *Neuroimage* 34, 661-670.

- Butson, C.R., Cooper, S.E., Henderson, J.M., Wolgamuth, B., McIntyre, C.C., 2011. Probabilistic analysis of activation volumes generated during deep brain stimulation. *Neuroimage* 54, 2096-2104.
- Caire, F., Ranoux, D., Guehl, D., Burbaud, P., Cuny, E., 2013. A systematic review of studies on anatomical position of electrode contacts used for chronic subthalamic stimulation in Parkinson's disease. *Acta Neurochir (Wien)* 155, 1647-1654; discussion 1654.
- Calabrese, E., 2016. Diffusion Tractography in Deep Brain Stimulation Surgery: A Review. *Front Neuroanat* 10, 45.
- Chaturvedi, A., Butson, C.R., Lempka, S.F., Cooper, S.E., McIntyre, C.C., 2010. Patient-specific models of deep brain stimulation: influence of field model complexity on neural activation predictions. *Brain Stimul* 3, 65-67.
- Coenen, V.A., Allert, N., Madler, B., 2011. A role of diffusion tensor imaging fiber tracking in deep brain stimulation surgery: DBS of the dentato-rubro-thalamic tract (drt) for the treatment of therapy-refractory tremor. *Acta Neurochir (Wien)* 153, 1579-1585; discussion 1585.
- Coenen, V.A., Allert, N., Paus, S., Kronenburger, M., Urbach, H., Madler, B., 2014. Modulation of the cerebello-thalamo-cortical network in thalamic deep brain stimulation for tremor: a diffusion tensor imaging study. *Neurosurgery* 75, 657-669; discussion 669-670.
- Conrad, E.C., Mossner, J.M., Chou, K.L., Patil, P.G., 2018. Atlas-Independent, Electrophysiological Mapping of the Optimal Locus of Subthalamic Deep Brain Stimulation for the Motor Symptoms of Parkinson Disease. *Stereotact Funct Neurosurg* 96, 91-99.
- de Luis-García, R., Alberola-López, C., Kindlmann, G., Westin, CF., 2009. Automatic Segmentation of White Matter Structures from DTI Using Tensor Invariants and Tensor Orientation. *Proceedings of the International Society for Magnetic Resonance in Medicine*.
- de Luis-García, R., Alberola-López, C., Westin, CF., 2012. On the Choice of a Tensor Distance for DTI White Matter Segmentation. *New Developments in the Visualization and Processing of Tensor Fields*.
- Dembek, T.A., Barbe, M.T., Astrom, M., Hoevels, M., Visser-Vandewalle, V., Fink, G.R., Timmermann, L., 2017. Probabilistic mapping of deep brain stimulation effects in essential tremor. *Neuroimage Clin* 13, 164-173.
- Deoni, S.C., Rutt, B.K., Parrent, A.G., Peters, T.M., 2007. Segmentation of thalamic nuclei using a modified k-means clustering algorithm and high-resolution quantitative magnetic resonance imaging at 1.5 T. *Neuroimage* 34, 117-126.
- Deuschl, G., Raethjen, J., Hellriegel, H., Elble, R., 2011. Treatment of patients with essential tremor. *Lancet Neurol* 10, 148-161.
- Duan, Y., Li, X., Xi, Y., 2007. Thalamus segmentation from diffusion tensor magnetic resonance imaging. *Int J Biomed Imaging* 2007, 90216.

- Duchin, Y., Abosch, A., Yacoub, E., Sapiro, G., Harel, N., 2012. Feasibility of using ultra-high field (7 T) MRI for clinical surgical targeting. *PLoS One* 7, e37328.
- Elias, W.J., Zheng, Z.A., Domer, P., Quigg, M., Pouratian, N., 2012. Validation of connectivity-based thalamic segmentation with direct electrophysiologic recordings from human sensory thalamus. *Neuroimage* 59, 2025-2034.
- Forutan, H., Majtanik, M., Buehrle, C.P., Treuer, H., Gierich, A., Mai, J.K., 2015. Implementation of the 3D-atlas of the human brain for high precision robot-guided and frame-based stereotactic implantation of intracerebral deep brain electrodes. *Movement disorders* 30, S219-S219.
- Gibson, W.S., Jo, H.J., Testini, P., Cho, S., Felmlee, J.P., Welker, K.M., Klassen, B.T., Min, H.K., Lee, K.H., 2016. Functional correlates of the therapeutic and adverse effects evoked by thalamic stimulation for essential tremor. *Brain* 139, 2198-2210.
- Grassi, A., Cammoun, L., Pollo, C., Hagmann, P., Meuli, R., Thiran, J.P., 2008. Thalamic nuclei clustering on High Angular Resolution Diffusion Images. *International Society for Magnetic Resonance in Medicine*, Toronto.
- Hamani, C., Dostrovsky, J.O., Lozano, A.M., 2006. The motor thalamus in neurosurgery. *Neurosurgery* 58, 146-158; discussion 146-158.
- Haueisen, J., Tuch, D.S., Ramon, C., Schimpf, P.H., Wedeen, V.J., George, J.S., Belliveau, J.W., 2002. The influence of brain tissue anisotropy on human EEG and MEG. *Neuroimage* 15, 159-166.
- Hemm, S., Pison, D., Alonso, F., Shah, A., Coste, J., Lemaire, J.J., Wardell, K., 2016. Patient-Specific Electric Field Simulations and Acceleration Measurements for Objective Analysis of Intraoperative Stimulation Tests in the Thalamus. *Front Hum Neurosci* 10, 577.
- Houshmand, L., 2015. Optimized Targeting in Deep Brain Stimulation for Movement Disorders. *Optimized Targeting in Deep Brain Stimulation for Movement Disorders*.
- Howell, B., McIntyre, C.C., 2016. Analyzing the tradeoff between electrical complexity and accuracy in patient-specific computational models of deep brain stimulation. *J Neural Eng* 13, 036023.
- Jaermann, T., Crelier, G., Pruessmann, K.P., Golay, X., Netsch, T., van Muiswinkel, A.M.C., Mori, S., van Zijl, P.C.M., Valavanis, A., Kollias, S., Boesiger, P., 2004. SENSE-DTI at 3 T. *Magnetic Resonance in Medicine*.
- Jakab, A., Blanc, R., Berenyi, E.L., Szekely, G., 2012. Generation of individualized thalamus target maps by using statistical shape models and thalamocortical tractography. *AJNR Am J Neuroradiol* 33, 2110-2116.

- Johansen-Berg, H., Behrens, T.E., Sillery, E., Ciccarelli, O., Thompson, A.J., Smith, S.M., Matthews, P.M., 2005. Functional-anatomical validation and individual variation of diffusion tractography-based segmentation of the human thalamus. *Cereb Cortex* 15, 31-39.
- Jonasson, L., Hagmann, P., Pollo, C., Bresson, X., Wilson, C.R., Meuli, R., Thiran, J.P., 2007. A level set method for segmentation of the thalamus and its nuclei in DT-MRI. *Signal Processing* 87, 309-321.
- Kanowski, M., Voges, J., Buentjen, L., Stadler, J., Heinze, H.J., Tempelmann, C., 2014. Direct visualization of anatomic subfields within the superior aspect of the human lateral thalamus by MRI at 7T. *AJNR Am J Neuroradiol* 35, 1721-1727.
- Keane, M., Deyo, S., Abosch, A., Bajwa, J.A., Johnson, M.D., 2012. Improved spatial targeting with directionally segmented deep brain stimulation leads for treating essential tremor. *J Neural Eng* 9, 046005.
- Kim, W., Chivukula, S., Hauptman, J., Pouratian, N., 2016. Diffusion Tensor Imaging-Based Thalamic Segmentation in Deep Brain Stimulation for Chronic Pain Conditions. *Stereotact Funct Neurosurg* 94, 225-234.
- Klein, J.C., Barbe, M.T., Seifried, C., Baudrexel, S., Runge, M., Maarouf, M., Gasser, T., Hattingen, E., Liebig, T., Deichmann, R., Timmermann, L., Weise, L., Hilker, R., 2012. The tremor network targeted by successful VIM deep brain stimulation in humans. *Neurology* 78, 787-795.
- Krauth, A., Blanc, R., Poveda, A., Jeanmonod, D., Morel, A., Szekely, G., 2010. A mean three-dimensional atlas of the human thalamus: generation from multiple histological data. *Neuroimage* 49, 2053-2062.
- Kuncel, A.M., Cooper, S.E., Grill, W.M., 2008. A method to estimate the spatial extent of activation in thalamic deep brain stimulation. *Clin Neurophysiol* 119, 2148-2158.
- Kwon, H.G., Hong, J.H., Hong, C.P., Lee, D.H., Ahn, S.H., Jang, S.H., 2011. Dentatorubrothalamic tract in human brain: diffusion tensor tractography study. *Neuroradiology* 53, 787-791.
- Lambert, C., Simon, H., Colman, J., Barrick, T.R., 2017. Defining thalamic nuclei and topographic connectivity gradients *in vivo*. *Neuroimage* 158, 466-479.
- Lemaire, J.J., Sakka, L., Ouchchane, L., Caire, F., Gabrillargues, J., Bonny, J.M., 2010. Anatomy of the human thalamus based on spontaneous contrast and microscopic voxels in high-field magnetic resonance imaging. *Neurosurgery* 66, 161-172.
- Macchi, G., Jones, E.G., 1997. Toward an agreement on terminology of nuclear and subnuclear divisions of the motor thalamus. *J Neurosurg* 86, 77-92.

- Madler, B., Coenen, V.A., 2012. Explaining clinical effects of deep brain stimulation through simplified target-specific modeling of the volume of activated tissue. *AJNR Am J Neuroradiol* 33, 1072-1080.
- Maks, C.B., Butson, C.R., Walter, B.L., Vitek, J.L., McIntyre, C.C., 2009. Deep brain stimulation activation volumes and their association with neurophysiological mapping and therapeutic outcomes. *J Neurol Neurosurg Psychiatry* 80, 659-666.
- Mang, S.C., Busza, A., Reiterer, S., Grodd, W., Klose, A.U., 2012. Thalamus segmentation based on the local diffusion direction: a group study. *Magn Reson Med* 67, 118-126.
- Morel, A., Magnin, M., Jeanmonod, D., 1997. Multiarchitectonic and stereotactic atlas of the human thalamus. *J Comp Neurol* 387, 588-630.
- Nestor, K.A., Jones, J.D., Butson, C.R., Morishita, T., Jacobson, C.E.t., Peace, D.A., Chen, D., Foote, K.D., Okun, M.S., 2014. Coordinate-based lead location does not predict Parkinson's disease deep brain stimulation outcome. *PLoS One* 9, e93524.
- Niemann, K., van Nieuwenhofen, I., 1999. One atlas - three anatomies: relationships of the Schaltenbrand and Wahren microscopic data. *Acta Neurochir (Wien)* 141, 1025-1038.
- Pahwa, R., Lyons, K.E., Wilkinson, S.B., Simpson, R.K., Jr., Ondo, W.G., Tarsy, D., Norregaard, T., Hubble, J.P., Smith, D.A., Hauser, R.A., Jankovic, J., 2006. Long-term evaluation of deep brain stimulation of the thalamus. *J Neurosurg* 104, 506-512.
- Patil, P.G., Conrad, E.C., Aldridge, J.W., Chenevert, T.L., Chou, K.L., 2012. The anatomical and electrophysiological subthalamic nucleus visualized by 3-T magnetic resonance imaging. *Neurosurgery* 71, 1089-1095; discussion 1095.
- Percheron, G., Francois, C., Talbi, B., Yelnik, J., Fenelon, G., 1996. The primate motor thalamus. *Brain Res Brain Res Rev* 22, 93-181.
- Phibbs, F.T., Pallavaram, S., Tolleson, C., D'Haese, P.F., Dawant, B.M., 2014. Use of efficacy probability maps for the post-operative programming of deep brain stimulation in essential tremor. *Parkinsonism & related disorders* 20, 1341-1344.
- Pouratian, N., Zheng, Z., Bari, A.A., Behnke, E., Elias, W.J., Desalles, A.A., 2011. Multi-institutional evaluation of deep brain stimulation targeting using probabilistic connectivity-based thalamic segmentation. *J Neurosurg* 115, 995-1004.
- Power, B.D., Wilkes, F.A., Hunter-Dickson, M., van Westen, D., Santillo, A.F., Walterfang, M., Nilsson, C., Velakoulis, D., Looi, J.C., 2015. Validation of a protocol for manual segmentation of the thalamus on magnetic resonance imaging scans. *Psychiatry Res* 232, 98-105.
- Rittner, L., Lotufo, R.A., Campbell, J., Pike, G.B., 2010. Segmentation of thalamic nuclei based on tensorial morphological gradient of diffusion tensor fields. *Biomedical Imaging: From Nano to Macro*, 2010 IEEE International Symposium on, pp. 1173-1176.

- Sandvik, U., Koskinen, L.O., Lundquist, A., Blomstedt, P., 2012. Thalamic and subthalamic deep brain stimulation for essential tremor: where is the optimal target? *Neurosurgery* 70, 840-845; discussion 845-846.
- Schaltenbrand, G., Wahren, W., Hassler, R., 1977. *Atlas for Stereotaxy of the Human Brain*. G. Thieme, Stuttgart.
- Schultz, T., 2011. Segmenting Thalamic Nuclei: What Can We Gain from HARDI? In: Fichtinger, G., Martel, A., Peters, T. (Eds.), *Medical Image Computing and Computer-Assisted Intervention – MICCAI 2011*. Springer Berlin Heidelberg, pp. 141-148.
- Spiegelmann, R., Nissim, O., Daniels, D., Ocherashvilli, A., Mardor, Y., 2006. Stereotactic targeting of the ventrointermediate nucleus of the thalamus by direct visualization with high-field MRI. *Stereotact Funct Neurosurg* 84, 19-23.
- Talairach, J., Tournoux, P., 1988. Co-planar stereotaxic atlas of the human brain. 3-Dimensional proportional system: an approach to cerebral imaging. *Co-planar stereotaxic atlas of the human brain. 3-Dimensional proportional system: an approach to cerebral imaging*.
- Tourdias, T., Saranathan, M., Levesque, I.R., Su, J., Rutt, B.K., 2014. Visualization of intrathalamic nuclei with optimized white-matter-nulled MPRAGE at 7T. *Neuroimage* 84, 534-545.
- Tuch, D.S., Wedeen, V.J., Dale, A.M., George, J.S., Belliveau, J.W., 2001. Conductivity tensor mapping of the human brain using diffusion tensor MRI. *Proc Natl Acad Sci U S A* 98, 11697-11701.
- Udupa, K., Chen, R., 2015. The mechanisms of action of deep brain stimulation and ideas for the future development. *Prog Neurobiol* 133, 27-49.
- Vaillancourt, D.E., Sturman, M.M., Verhagen Metman, L., Bakay, R.A., Corcos, D.M., 2003. Deep brain stimulation of the VIM thalamic nucleus modifies several features of essential tremor. *Neurology* 61, 919-925.
- Vassal, F., Coste, J., Derost, P., Mendes, V., Gabrillargues, J., Nuti, C., Durif, F., Lemaire, J.J., 2012. Direct stereotactic targeting of the ventrointermediate nucleus of the thalamus based on anatomic 1.5-T MRI mapping with a white matter attenuated inversion recovery (WAIR) sequence. *Brain Stimul* 5, 625-633.
- Wang, Z.Z., Vemuri, B.C., 2004. An affine invariant tensor dissimilarity measure and its applications to tensor-valued image segmentation. *Proceedings of the 2004 Ieee Computer Society Conference on Computer Vision and Pattern Recognition*, Vol 1, 228-233.
- Wiegell, M.R., Tuch, D.S., Larsson, H.B., Wedeen, V.J., 2003. Automatic segmentation of thalamic nuclei from diffusion tensor magnetic resonance imaging. *Neuroimage* 19, 391-401.
- Xiao, Y., Zitella, L.M., Duchin, Y., Teplitzky, B.A., Kastl, D., Adriany, G., Yacoub, E., Harel, N., Johnson, M.D., 2016. Multimodal 7T Imaging of Thalamic Nuclei for Preclinical Deep Brain Stimulation Applications. *Front Neurosci* 10, 264.

Zerroug, A., Gabrillargues, J., Coll, G., Vassal, F., Jean, B., Chabert, E., Claise, B., Khalil, T., Sakka, L., Feschet, F., Durif, F., Boyer, L., Coste, J., Lemaire, J.J., 2016. Personalized mapping of the deep brain with a white matter attenuated inversion recovery (WAIR) sequence at 1.5-tesla: Experience based on a series of 156 patients. *Neurochirurgie* 62, 183-189.

Ziyan, U., Tuch, D., Westin, C.-F., 2006. Segmentation of thalamic nuclei from DTI using spectral clustering. *Segmentation of thalamic nuclei from DTI using spectral clustering*. Springer, pp. 807-814.

Ziyan, U., Westin, C.F., 2008. Joint segmentation of thalamic nuclei from a population of diffusion tensor MR images. *Med Image Comput Comput Assist Interv* 11, 279-286.

Chapter 4

Data-Driven Model Comparing the Effects of Glial Scarring and Interface Interactions on Chronic Neural Recordings in Non-Human Primates

Citation: Karlo A Malaga et al 2016 J. Neural Eng. 13 016010. <https://doi.org/10.1088/1741-2560/13/1/016010>

Abstract

We characterized electrode stability over 12 weeks of impedance and neural recording data from four chronically-implanted Utah arrays in two rhesus macaques, and investigated the effects of glial scarring and interface interactions at the electrode recording site on signal quality using a computational model.

A finite element model of a Utah array microelectrode in neural tissue was coupled with a multi-compartmental model of a neuron to quantify the effects of encapsulation thickness, encapsulation resistivity, and interface resistivity on electrode impedance and waveform amplitude. The coupled model was then reconciled with the *in vivo* data. Histology was obtained 17 weeks post-implantation to measure gliosis.

From week 1-3, mean impedance and amplitude increased at rates of 115.8 k Ω /week and 23.1 μ V/week, respectively. This initial ramp up in impedance and amplitude was observed across all arrays, and is consistent with biofouling (increasing interface resistivity) and edema clearing (increasing tissue resistivity), respectively, in the model. Beyond week 3, the trends leveled out. Histology showed that thin scars formed around the electrodes. In the model,

scarring could not match the *in vivo* data. However, a thin interface layer at the electrode tip could. Despite having a large effect on impedance, interface resistivity did not have a noticeable effect on amplitude.

This study suggests that scarring does not cause an electrical problem with regard to signal quality since it does not appear to be the main contributor to increasing impedance or significantly affect amplitude unless it displaces neurons. This, in turn, suggests that neural signals can be obtained reliably despite scarring as long as the recording site has sufficiently low impedance after accumulating a thin layer of biofouling. Therefore, advancements in microelectrode technology may be expedited by focusing on improvements to the recording site-tissue interface rather than elimination of the glial scar.

Introduction

A brain-machine interface (BMI) is a type of neuroprosthetic device aimed towards restoring lost motor, sensory, and/or cognitive function to patients with neurological disorders (Collinger et al., 2014; Hochberg et al., 2006; Taylor et al., 2002). BMIs use electrical signals from the brain to control external devices such as computer cursors, robotic limbs, and exoskeletons. These neural signals can come from various sources such as electroencephalography (EEG), electrocorticography (ECoG), and single-unit recordings, which differ in their degree of invasiveness, amplitude, and bandwidth. For single-unit recordings, action potentials from individual neurons are measured using electrodes implanted in the brain. Notable examples of intracortical microelectrode arrays used to record single-unit activity include microwires (Williams et al., 1999), Michigan probes (Vetter et al., 2004), and Utah arrays (Nordhausen et al., 1996). Recordings from such devices provide high spatial resolution. However, it can be difficult to identify and isolate individual units. For BMIs to become

clinically viable, electrode arrays must be able to acquire stable, high-quality signals for years. Currently, the ability to reliably record single-unit activity with intracortical microelectrode arrays is hindered by low signal-to-noise ratio (SNR). A low SNR can come from a variety of biological, material, or mechanical failure modes (Barrese et al., 2013).

Over time, signal quality can be affected by many different factors. One factor is the brain tissue response (Polikov et al., 2005; Stensaas and Stensaas, 1976; Szarowski et al., 2003; Turner et al., 1999), which occurs when electrodes are implanted in the brain. This response is divided into two phases: (1) an acute inflammatory response and (2) a chronic foreign body reaction. The acute phase starts upon electrode insertion, is characterized by edema and activated microglia, and usually lasts 1-3 weeks. The chronic phase starts after the acute tissue reaction subsides and is characterized by the formation of a fibrous encapsulation layer around the electrodes, termed glial scarring/encapsulation and/or gliosis, by reactive astrocytes. This accumulation of cells surrounds the surface of the electrodes and is usually complete within 6-8 weeks. The glial scar is hypothesized to decrease signal quality (Biran et al., 2005; Edell et al., 1992; Johnson et al., 2005; Otto et al., 2006). However, there is no accepted electrical explanation for how this occurs. Possible explanations include increased impedance due to the scar insulating the electrode (Johnson et al., 2005; Otto et al., 2006; Prasad and Sanchez, 2012; Williams et al., 2007) and isolation of the electrode from nearby neurons in the surrounding tissue due to growth of the encapsulation layer (i.e., decreased neuronal density) (Biran et al., 2005; Edell et al., 1992). The mechanisms underlying glial scar formation have been studied extensively. However, a consensus regarding its effect on chronic neural recordings has yet to be determined. Some studies have reported conflicting results, showing variable signal quality during the scar formation period followed by still-identifiable neural signals over subsequent

months (Barrese et al., 2013; Chestek et al., 2011; Fraser et al., 2009; Kruger et al., 2010; Simeral et al., 2011; Suner et al., 2005). Furthermore, it is unclear if the glial scar is responsible for device failure multiple years after implantation.

Although less studied, material degradation is another major failure mechanism of implantable electrode arrays (Barrese et al., 2013). To enhance biocompatibility and facilitate recording, electrodes are coated with an insulating material (e.g., polyimide, Parylene C) and metal (e.g., platinum, iridium oxide) is applied to the recording site, respectively. Over time, these materials may start to degrade (Prasad et al., 2014; Takmakov et al., 2015; Xie et al., 2014). For example, the electrode insulation could develop cracks (Prasad et al., 2014; Takmakov et al., 2015) or the tip metallization could be lost (Xie et al., 2014). Therefore, many groups have started investigating alternative coating techniques and materials to extend device longevity (Cui et al., 2003; Green et al., 2012; Selvakumaran et al., 2008; Sommakia et al., 2014; Sommakia et al., 2009). Material failures have become more of a concern with regard to signal stability over time since the glial scar may stabilize within a few months (Barrese et al., 2013).

Another factor that is hypothesized to impact signal quality is the adsorption of proteins on the recording site, termed biofouling. Since biofouling may increase electrode impedance, efforts have been made to reduce the extent of it (Sommakia et al., 2014; Sommakia et al., 2009). One approach is to coat the electrode with anti-fouling materials before implantation. For example, coating with polyethylene glycol (PEG) has been found to reduce protein adsorption and prevent impedance increases (Sommakia et al., 2014; Sommakia et al., 2009).

Alongside experimental studies, there have been a number of computational models developed to better understand neural recordings and how they are affected by different factors (Holt and Koch, 1999; Lempka et al., 2011; Mainen et al., 1995; Moffitt and McIntyre, 2005;

Reimann et al., 2013). Such models are useful for performing analyses that would be difficult to implement experimentally and continue to grow in complexity. For example, they have included explicit representation of a microelectrode implanted in the brain, populated the surrounding tissue with hundreds of individual neuron models, and incorporated sources of thermal and biological noise (Lempka et al., 2011; Moffitt and McIntyre, 2005). Results from these models have been consistent with and validated by experimental findings (Henze et al., 2000). They can also make interesting predictions that can influence and encourage further investigation. For example, one modeling study predicted that electrode encapsulation results in increased waveform amplitude (Moffitt and McIntyre, 2005), which conflicts with current assumptions regarding the effect of the glial scar on single-unit recordings.

In this study, we characterized electrode stability over 12 weeks of impedance (1 kHz) and broadband ($f_s = 30$ kHz) neural recording data from four chronically-implanted Utah arrays in two rhesus macaques (two arrays/monkey). We then investigated the effect of the glial scar, also known as glial encapsulation and/or gliosis, and interface between the recording site and surrounding neural tissue on signal quality using a data-driven neural recording model. A previously-described computational model (Lempka et al., 2011; Moffitt and McIntyre, 2005) was modified with the specific geometry and material properties of a Utah array microelectrode to quantify the effect of encapsulation thickness, encapsulation resistivity, and interface resistivity on electrode impedance and waveform amplitude. The model was then reconciled with the *in vivo* data. Histology, stained for microglia, was obtained from one monkey 17 weeks post-implantation to measure gliosis around the electrodes.

Methods

Experimental Methods

Data Acquisition

All procedures were carried out in accordance with protocols approved by the University Committee on Use and Care of Animals at the University of Michigan. Two rhesus macaques were each implanted with two Utah arrays (Blackrock Microsystems, Salt Lake City, UT, USA) in finger and hand areas of primary motor cortex (M1) using standard neurosurgical techniques (Hatsopoulos et al., 2004). The arrays had 96 active electrode channels, platinum (~400 k Ω at 1 kHz) electrode site metal, and parylene C insulation. The target region was located by identifying the point where the spur of the arcuate sulcus would intersect the central sulcus. The arrays were then placed at this location, just anterior to the central sulcus.

The two monkeys were trained to sit quietly in a chair (Crist Instrument Co., Inc., Hagerstown, MD, USA) during recording sessions, which consisted of two minutes of calm sitting. Broadband neural data were sampled at 30 kHz and recorded using a Cerebus neural signal processor (NSP) (Blackrock Microsystems). Multi-unit recordings were obtained by thresholding at -4.5x the RMS noise on each electrode. After each session, 1 kHz impedance measurements were obtained from each electrode using the same Cerebus system starting one week post-implantation. Complex impedance measurements were also obtained from seven electrodes from one array using a precision LCR meter (LCR-8110G) (GW Instek, New Taipei City, Taiwan). Measurements were taken 2.5 weeks post-implantation at 14 equally spaced (150 Hz) frequencies between 100 and 2050 Hz using a two-electrode setup, with one electrode on the measured pin and the other on the ground pin. Histology was obtained from one monkey after it

was euthanized due to an unrelated health concern. This occurred after the conclusion of this study.

Data Analysis

From four arrays in two monkeys (two arrays/monkey), *in vivo* data from the first 12 weeks post-implantation were analyzed offline. The first 12 weeks were chosen since this is the critical period of scar formation (Polikov et al., 2005). Electrodes were excluded from further analyses if any of their weekly impedance measurements (12 measurements/electrode) exceeded 2.5 M Ω . This was done since such high impedances often come from damaged electrodes (Xie et al., 2014). Of the 384 total electrodes (4 arrays x 96 electrodes/array), 96 were excluded across all four arrays. Specifically, 1, 26, 46, and 23 electrode(s) had a least one impedance measurement greater than 2.5 M Ω from array S-1, S-2, K-1, and K-2, respectively (supplementary data). In addition to looking at all viable ($Z < 2.5$ M Ω) electrodes ($n = 288$), the top 20 electrodes ($n = 80$) with the largest single-units from each array were analyzed separately. Multiple comparisons for one-way analysis of variance (ANOVA) were used to compare mean electrode impedance (1 kHz) and waveform amplitude (peak-to-peak) between different weeks. False discovery rate control and bootstrapping were used to identify significant trends for individual electrodes. All analyses were performed in MATLAB (The MathWorks, Inc., Natick, MA, USA).

Histology

Histology, stained for microglia, was obtained from one monkey 17 weeks post-implantation to measure gliosis around the electrodes. Tissue sections were taken from one array along the shanks, where the glial scar is likely larger compared to at the tips (Thelin et al., 2011). The section was first soaked in 4% (w/v) paraformaldehyde (P6148) (Sigma-Aldrich, St. Louis,

MO, USA) in 1x phosphate buffered saline (PBS) (BP3994) (Fisher Scientific, Waltham, MA, USA) for 24 hours. Once fixed, the tissue was cryoprotected by successive 24 hour-long soaks in 10%, 20%, and 30% (w/v) D-Sucrose (BP220) (Fisher Scientific) in 1x PBS. The tissue was then embedded in Tissue-Tek O.C.T. Compound (4583) (Sakura Finetek Europe B.V., Alphen aan den Rijn, The Netherlands) and frozen at -20°C. The frozen sample was sectioned into 20 µm-thick slices using a Microm HM550 cryostat (Fisher Scientific) and mounted directly onto slides. A hydrophobic barrier was then drawn around each slice using an ImmEdge pen (22312) (Ted Pella, Inc., Redding, CA, USA) and allowed to dry.

Before staining, the slices were rinsed with 1x PBS for 10 minutes. They were then blocked with 10% normal goat serum blocking solution (S-1000) (Vector Laboratories, Inc., Burlingame, CA, USA) in 1x PBS for one hour at room temperature and incubated in a solution of Anti Iba1, Rabbit (1:1,000 dilution) (019-19741) (Wako Chemicals USA, Inc., Richmond, VA, USA), 0.3% Triton X-100 (T8787) (Sigma-Aldrich), and 3% normal goat serum blocking solution in 1x PBS overnight in a covered chamber. The following day, the slices were triple rinsed with 1x PBS, with each rinse sitting for 10 minutes. They were then incubated in a solution of Goat anti-Rabbit IgG (H+L) Secondary Antibody, Alexa Fluor 546 conjugate (1:200 dilution) (A-11035) (Life Technologies, Grand Island, NY, USA), 0.2% Triton X-100, and 5% normal goat serum blocking solution in 1x PBS for two hours at room temperature. Next, the slices were double rinsed with 1x PBS, with each rinse lasting 10 minutes. Slides were then coverslipped using ProLong Gold Antifade Mountant (P36930) (Life Technologies) and allowed to dry overnight before imaging. A LSM 510 META Laser Scanning Confocal Microscope (Zeiss, Oberkochen, Germany) was used to image the stained slices. Encapsulation thickness was

estimated by taking clockwise (3, 6, 9, and 12 o'clock) measurements of the glial scar around the electrodes and averaging the values.

Computational Methods

Finite Element Model

The neural recording model used in this study was similar to previously-described computational models (Lempka et al., 2011; Mainen et al., 1995; Moffitt and McIntyre, 2005). The model consisted of two main components: (1) a three-dimensional finite element model (FEM) of a microelectrode implanted in neural tissue and (2) a multi-compartmental model of a neuron. The FEM was assumed to be electrostatic since the impedance of gray matter is relatively frequency-independent (Logothetis et al., 2007). The FEM was generated and solved in COMSOL Multiphysics 4.4 (COMSOL, Inc., Burlington, MA, USA), as shown in Figure 4-1(a, b). The surrounding tissue was modeled as a cylinder with a height of 16,000 μm and radius of 8,000 μm , while the electrode was modeled as a Utah array microelectrode (Nordhausen et al., 1996). The electrode consisted of: (1) a conical shank with a height of 1,450 μm , top radius of 45 μm , and bottom radius of 14 μm , (2) a conical tip with a height of 50 μm , top radius of 14 μm , and bottom radius of 1.5 μm (exposed surface area = 2,517 μm^2), and (3) an insulation layer around the shank with a uniform thickness of 10 μm . The microelectrode was placed at the center of the neural tissue, such that the center of the bottom of the shank/top of the tip was at the origin. The tip was surrounded by a thin layer with a uniform thickness of 0.5 μm to incorporate the interface between the recording site and surrounding tissue into the FEM (Cantrell et al., 2008; Hoyum et al., 2010; McIntyre and Grill, 2001). In reality, this interface layer has a thickness on the order of nanometers (Hoyum et al., 2010), and, ideally, it would be represented to scale in the FEM. However, meshing such a thin layer of finite thickness requires

a large computational cost. To work around this constraint, the interface layer was made thicker and its electrical properties were adapted to account for the increase in thickness (Hoyum et al., 2010). This was the trade-off between having a realistic model and one that was computationally efficient without reducing accuracy. To complete the FEM, the electrode, including the interface, was surrounded by a layer with a uniform thickness of 20 μm to incorporate the glial scar. The default thickness of the scar was estimated from histology (described below) and was comparable to other observed encapsulation thicknesses (Szarowski et al., 2003; Turner et al., 1999).

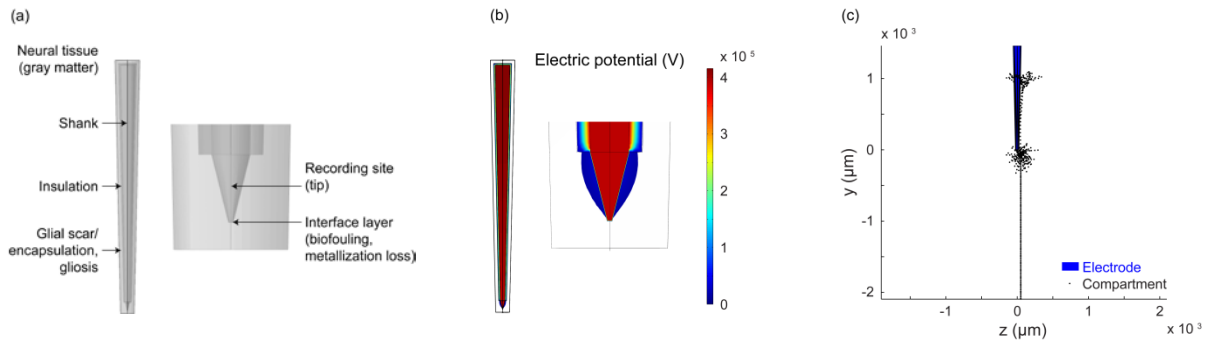


Figure 4-1 Neural recording model. (a) FEM geometry and domains. The glial scar/encapsulation, gliosis domain corresponds to the layer surrounding the entire electrode. The interface layer (biofouling, metallization loss) domain corresponds to the thin layer surrounding the electrode tip. (b) FEM solution. (c) Compartmental model. The axon is parallel to the electrode and the soma is 50 μm away from the bottom of the tip.

The material and electrical resistivity of the FEM domains are shown in Table 4-1. Each domain had a uniform resistivity, which was either acquired or derived from the literature. The interface layer resistivity was estimated with complex impedance data from seven viable electrodes from one array (described above). A previously-described equivalent circuit model for the electrode-tissue interface was used to isolate the interface component (Johnson et al., 2005; Lempka et al., 2011; Otto et al., 2006; Williams et al., 2007). Briefly, the interface can be

modeled as a constant phase element (CPE). CPE impedance (Z_{CPE}) was calculated using the following equation:

$$Z_{CPE} = \frac{K}{(j\omega)^\alpha}$$

where K is an electrode impedance scaling factor, j is the imaginary number, ω is the angular frequency, and α is a phase term defined over $0 \leq \alpha \leq 1$. K ($1.9e^7 \Omega \cdot s^{-\alpha}$ at 1 kHz) and α (0.5) were estimated by fitting the impedance data to the equivalent circuit model and used to calculate Z_{CPE} . The magnitude of Z_{CPE} ($|Z_{CPE}|$) was taken to account for the resistive and capacitive components of the impedance. Since the FEM was assumed to be electrostatic and recording electrodes are typically characterized with impedance measurements at 1 kHz, $|Z_{CPE}|$ was only calculated at that frequency (353.7 k Ω at 1 kHz) (Hoyum et al., 2010). In the FEM, the interface layer resistivity ($1.8e^5 \Omega \cdot \text{cm}$) that yielded an interface impedance (369.3 k Ω) closest to the calculated $|Z_{CPE}|$ was chosen as the default parameter value.

Table 4-1 Material and electrical resistivity of FEM domains

Domain	Material	Electrical resistivity (Ω -cm)
Shank	Doped silicon	3.3
Recording site (tip)	Platinum	$1.1e^{-5}$
Insulation	Parylene C	$1e^{15}$ (Xie et al., 2014)
Glial scar/encapsulation, gliosis	n/a	600 (Grill and Mortimer, 1994)
Interface layer (biofouling, metallization loss)	n/a	$1.8e^5$
Neural tissue (gray matter)	n/a	300 (Haueisen et al., 2002)

The FEM was meshed, with finer meshing applied at the electrode and its layers, and consisted of 685,049 elements. To test for model convergence, the mesh density of the FEM was increased. Increasing the number of elements by 3.5x resulted in a 0.01% change (+0.04 k Ω) in the value of the total system impedance. Therefore, the initial mesh density used was sufficient to confirm model convergence and ensure solution accuracy. The default mesh was used for all simulations involving changes in encapsulation and interface resistivity. Only the resistivity parameter values were adjusted (one at a time) before solving the FEM again (i.e., the FEM was not remeshed). For simulations involving changes in encapsulation thickness, the FEM had to be remeshed for each condition before a solution could be obtained. However, the mesh settings were not changed between simulations. To solve for the electric potential distribution, a load and boundary condition was defined. The load condition was a 1 A point current source placed at the bottom of the tip (described below). This current source was applied at a single element located in the center of the tip domain boundary. The boundary condition required that the surface of the surrounding neural tissue be set to ground. Electrode impedance was calculated by measuring the voltage drop from the bottom of the tip to ground after solving the FEM and dividing by the current source (1 A).

Multi-Compartmental Model

The compartmental model, as shown in Figure 4-1(c), was a layer V pyramidal cell from cat visual cortex that generated action potentials via excitatory synaptic inputs at the apical dendrites (Lempka et al., 2011; Mainen et al., 1995; Moffitt and McIntyre, 2005). Simulations were performed in NEURON 7.3 (Carnevale and Hines, 2006) to solve for the transmembrane currents generated in each compartment ($n = 531$) of the neuron during an action potential.

Model Coupling

The FEM and compartmental model were coupled in MATLAB to complete the computational model. This was accomplished by loading the electric potential distribution solved in COMSOL and the compartment coordinates and currents calculated in NEURON into MATLAB. In the coupled FEM-compartmental model, each neuron compartment was represented as a point current source and was placed accordingly within the FEM. The neuron model was rotated such that the axon was parallel to the electrode and translated such that the soma was 50 μm away from the bottom of the tip (Figure 4-1(c)). Unless otherwise noted, the simulated action potential recorded at the tip was calculated using previously-described methods (Lempka et al., 2011; Moffitt and McIntyre, 2005). Briefly, the potential (Φ) was calculated using the following equation:

$$\Phi = KJ$$

where K is a $(1 \times n)$ vector of the potentials that would be generated at the tip due to each of the n compartment currents and J is a $(n \times t)$ matrix of the compartment currents at each of the t time steps. The J matrix was calculated in NEURON and the K vector was derived from the FEM using a reciprocal solution. This involved applying a unit point current source (1 A) at a single element located in the center of the bottom boundary of the tip domain and then solving for the electric potential distribution in COMSOL. By the theorem of reciprocity, the potential induced at any given element within the FEM by the unit point current source applied at the electrode tip can be considered to be the potential that would be induced at the tip by a unit point current source applied at the same element (Lempka et al., 2011; Moffitt and McIntyre, 2005). For example, if a 1 V potential at element n is induced by the 1 A current source applied at the electrode tip, then the theorem of reciprocity stipulates that a 1 A current source applied at

element n will induce a 1 V potential at the tip. Therefore, the potential recorded at the electrode tip can be calculated by summing the individual contributions from each compartment current of the neuron model. Since the spatial location of the compartments within the FEM did not necessarily correspond to an element of the mesh, the potentials induced by each point current source had to be interpolated from the elements nearest each compartment in MATLAB.

Results

Electrode Impedance

Many existing hypotheses regarding device failure in chronic neural recordings involve increasing amounts of reactive tissue around the electrodes over time, which may increase electrode impedance (Johnson et al., 2005; Otto et al., 2006; Prasad and Sanchez, 2012; Williams et al., 2007). Therefore, impedance was examined over the first 12 weeks post-implantation to determine if it increased. Impedance measurements at 1 kHz were collected from the four arrays. One array was later excluded from the pooled array analyses since it pulled out of the brain due to tension on the wire. However, its individual analyses are included in the supplementary data. Of the 288 viable electrodes, 50 were excluded from this array. Figure 4-2(a) shows mean impedance (821.8 k Ω overall) for all viable electrodes from three arrays ($n = 238$). An overall linear increase of 12.2 k Ω /week was observed, but it was not significant at the 0.05 level ($p = 0.09$). Characteristic of Utah arrays, a subset of electrodes had large, well-defined single-units, while most of the others had smaller single- or multi-units. Therefore, impedance (785.3 k Ω overall) was also examined for the top 20 electrodes with the largest single-units from three arrays ($n = 60$). An overall linear increase of 12.8 k Ω /week was observed, but it also was not significant at the 0.05 level ($p = 0.06$).

Lack of a significant overall linear increase does not preclude a more resistive medium developing around the electrodes. The initial ramp in impedance during the first three weeks post-implantation (all viable: 115.8 k Ω /week, $p = 0.04$; top 20: 99.9 k Ω /week, $p = 0.21$) stands out and is nominally consistent with scarring onset (Polikov et al., 2005; Stensaas and Stensaas, 1976; Szarowski et al., 2003; Turner et al., 1999) and biofouling (Sommakia et al., 2014; Sommakia et al., 2009). Beyond week 3, the trend leveled out (all viable: -0.7 k Ω /week, $p = 0.91$; top 20: 4.2 k Ω /week, $p = 0.60$). Figure 4-2(b) shows mean impedance at week 1, 2, 3, and 12. Week 3 was significantly different from week 1 ($p < 0.001$, multiple comparisons). However, there was no significant difference between week 3 and week 2 and 12 ($p > 0.05$, multiple comparisons).

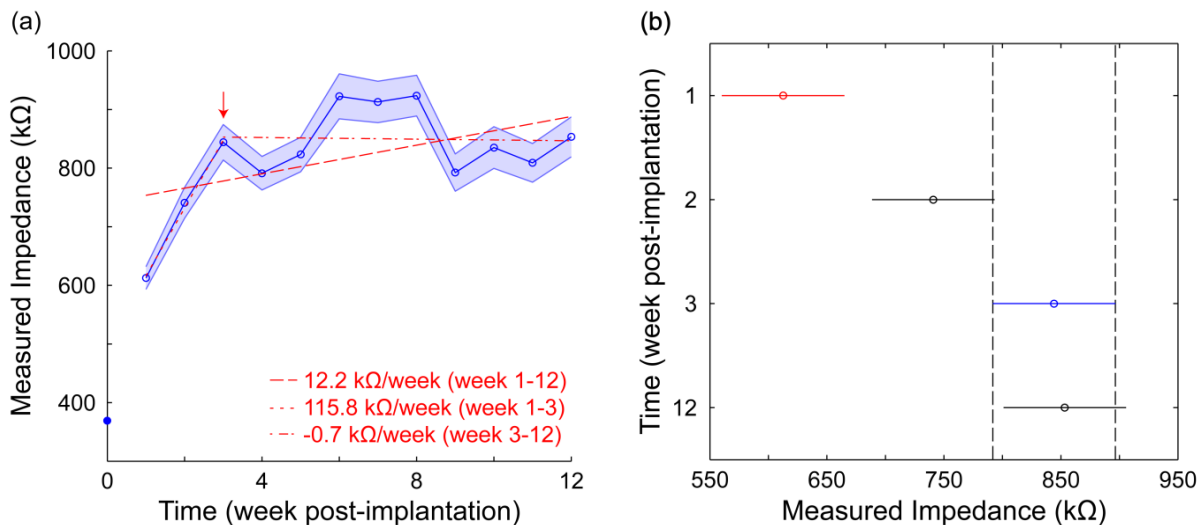


Figure 4-2 Mean impedance (at 1 kHz) over time (3/4 pooled arrays, all viable electrodes). (a) Week 1-12. Red lines are the linear regression fits. Arrow denotes week 3. Solid circle denotes the mean pre-implantation impedance. Error bars denote the standard error of the mean. (b) Week 1, 2, 3, and 12. Bars denote the comparison intervals. Color denotes the test group (blue) and significantly different groups (red).

To determine if this impedance trend was consistent with a previously-described tissue encapsulation model (Lempka et al., 2011; Moffitt and McIntyre, 2005), a sensitivity analysis of

encapsulation thickness was performed in a modified version of said model, which included the specific geometry and material properties of a Utah array microelectrode. With a default encapsulation and interface resistivity of 600 and $1.8e^5 \Omega\text{-cm}$, respectively, encapsulation thickness had a small effect on impedance, as shown in Figure 4-3. For example, a 10x increase in encapsulation thickness (20 to 200 μm) resulted in a mere 1.0% increase (+4.1 k Ω) in impedance. This makes sense since impedance is inversely proportional to the cross-sectional area of the electrode plus the encapsulation layer. As the encapsulation layer thickens, the total cross-sectional area increases. Therefore, any increase in impedance due to the scar thickening is offset by the accompanying increase in total cross-sectional area. Furthermore, there were no significant differences in impedance between simulations with and without an encapsulation layer (i.e., encapsulation resistivity = neural tissue resistivity = 300 $\Omega\text{-cm}$). For example, increasing encapsulation thickness from 0 to 5 μm resulted in only a 3.0% increase (+12.3 k Ω) in impedance and increasing it further had diminishing returns due to increasing cross-sectional area, as previously stated. Therefore, the model was unable to adequately match the observed changes in impedance when it only considered the glial scar. This suggests that scarring is not the main contributor to increasing impedance, assuming that the scar is not dramatically more resistive than the surrounding neural tissue (described below).

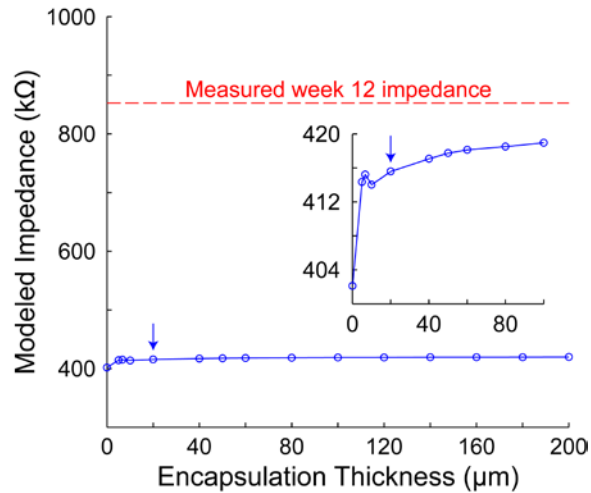


Figure 4-3 Effect of encapsulation thickness on impedance. Arrow denotes the default encapsulation thickness (20 μm). Inset expands the first half of the data.

Histology also confirmed that the contiguous scars did not thicken significantly. Instead, relatively thin scars formed around the electrodes. Figure 4-4 shows histology, stained for microglia, obtained from one monkey 17 weeks post-implantation. Mean microglial encapsulation thickness was 16.1 μm with a standard deviation of 10.0 μm, comparable to other observed encapsulation thicknesses (Szarowski et al., 2003; Turner et al., 1999). Therefore, a default encapsulation thickness of 20 μm was chosen for subsequent simulations.

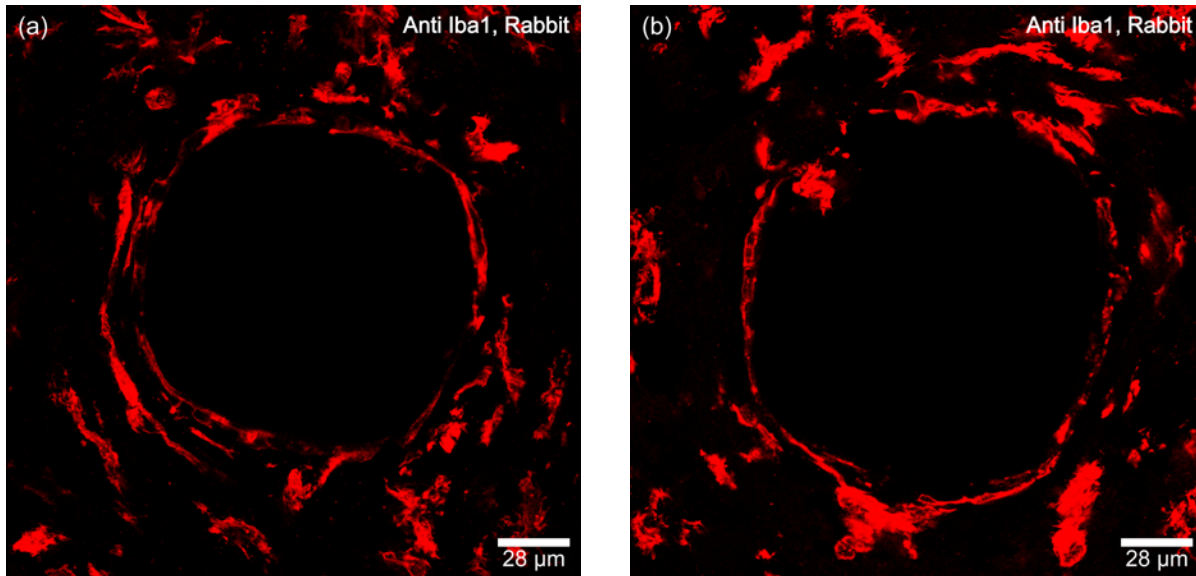


Figure 4-4 Gliosis around the electrodes obtained from one monkey 17 weeks post-implantation. (a, b) Tissue sections were taken from one array along the shanks. Microglia are stained red with Anti Iba1, Rabbit.

Since impedance was largely unaffected by encapsulation thickness, a sensitivity analysis of encapsulation resistivity was performed in the model. With a default encapsulation thickness and interface resistivity of $20\ \mu\text{m}$ and $1.8\text{e}^5\ \Omega\text{-cm}$, respectively, the default encapsulation resistivity would have to increase by 17.8x to reach the mean impedance at week 12, as shown in Figure 4-5. Therefore, the model was unable to adequately match the observed changes in impedance when it only considered the glial scar. This resulted in focus shifting to the interface between the recording site and surrounding neural tissue. The resistivity of the interface layer can be affected by many different factors such as biofouling (Sommakia et al., 2014; Sommakia et al., 2009) and metallization loss (Xie et al., 2014). Therefore, a sensitivity analysis of interface resistivity was performed in the model. With a default encapsulation thickness and resistivity of $20\ \mu\text{m}$ and $600\ \Omega\text{-cm}$, respectively, the default interface resistivity would have to increase by only 2.2x to reach the mean impedance at week 12 (Figure 4-5). Therefore, the model was better able to match the observed changes in impedance when it considered the thin interface around

the electrode tip. Such a layer is meant to be representative of biofouling or metallization loss. However, the model does not differentiate between these two conditions.

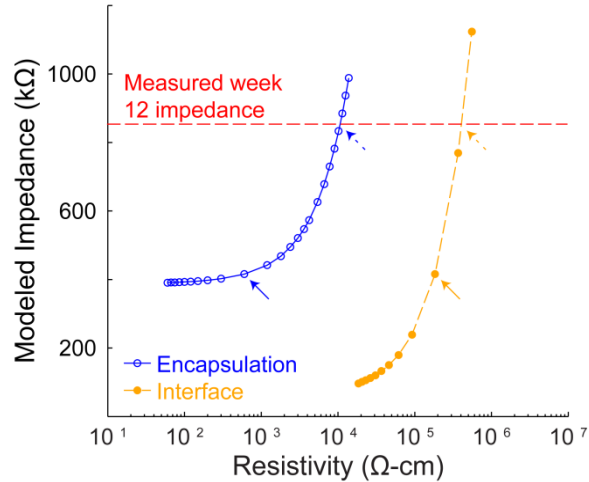


Figure 4-5 Effect of encapsulation and interface resistivity on impedance. Solid arrows denote the default encapsulation ($600 \Omega\text{-cm}$) and interface ($1.8e^5 \Omega\text{-cm}$) resistivity. Dashed arrows denote the encapsulation ($1.1e^4 \Omega\text{-cm}$) and interface ($4.1e^5 \Omega\text{-cm}$) resistivity necessary to match the measured mean impedance at week 12.

Consistent with the population data, impedance trends for individual electrodes tended to increase during the first three weeks post-implantation, showing considerable variation, and leveled out beyond week 3. Figure 4-6(a, b) shows regression slope for all viable electrodes from three arrays at week 1-3 and 3-12, and Table 4-2 summarizes the distributions (mean \pm standard deviation). Similar distributions were observed for the top 20 electrodes. Individual electrodes had significant ($p < 0.05$) positive and negative trends for week 3-12, although most were negative. A bootstrap analysis also yielded similar distributions, although week 1-3 showed more variation. Surprisingly, individual electrodes also had large and transient impedance differences from week-to-week in the positive and negative directions. Figure 4-6(c) shows week-to-week difference for all viable electrodes from three arrays at week 1-12. The distribution had a mean and standard deviation of 21.9 and 394.6 k Ω , respectively. Again, a similar distribution was

observed for the top 20 electrodes ($n = 660$, $20.6 \pm 364.2 \text{ k}\Omega$). A small amount of this variability comes from the measurement system (Figure 4-6(c)). Therefore, to test the accuracy of the Cerebus system, repeated impedance measurements were taken after removing and reattaching the connector between measurements, and without removing the connector between measurements (Figure 4-6(c)). Measurement-to-measurement difference showed considerably less variation than week-to-week difference for removal/reattachment ($n = 504$, $1.0 \pm 143.5 \text{ k}\Omega$) and without removal ($n = 752$, $-1.9 \pm 17.3 \text{ k}\Omega$). The week-to-week difference in impedance from higher-impedance electrodes measured with an Autolab in another study that we performed in a rodent model was also examined (Patel, 2015). Surprisingly, the differences showed even more variation ($n = 480$, $6.7 \pm 1.1 \times 10^3 \text{ k}\Omega$) compared to those observed in this study. While the computational model is able to capture a large range of impedances (Figure 4-5), there currently is no aspect of the model that can explain the large week-to-week differences in impedance observed for the individual electrodes. The source of this impedance variability remains to be identified. However, it may be difficult to pinpoint due to the dynamic nature of the neural environment.

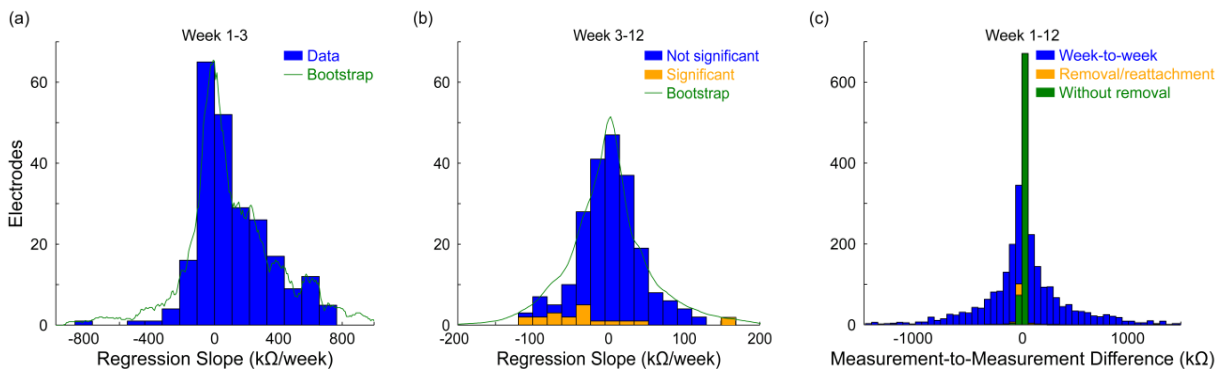


Figure 4-6 Distribution of regression slope and measurement-to-measurement difference in impedance (all viable electrodes, 238/288). (a) Week 1-3. (b) Week 3-12. (c) Week 1-12.

Table 4-2 Distribution of regression slope in impedance (kΩ/week)

All viable electrodes		Top 20 electrodes		Bootstrap	
Week 1-3	Week 3-12	Week 1-3	Week 3-12	Week 1-3	Week 3-12
115.8 ± 239.3	-0.7 ± 47.4	99.9 ± 226.1	4.2 ± 44.6	116.4 ± 332.9	-1.1 ± 58.5

Waveform Amplitude

The amplitude of the action potential, rather than the impedance of the electrode, is the most important measure for assessing signal quality. Therefore, in addition to impedance, electrode stability was characterized by the peak-to-peak amplitude of the largest single-unit on each electrode. As an electrode is encapsulated by reactive tissue over time, it is hypothesized that impedance increases and amplitude decreases (Biran et al., 2005; Edell et al., 1992; Johnson et al., 2005; Otto et al., 2006). However, multiple studies have reported being able to acquire neural signals over extended periods of time after scar formation (Barrese et al., 2013; Chestek et al., 2011; Fraser et al., 2009; Kruger et al., 2010; Simeral et al., 2011; Suner et al., 2005). Therefore, amplitude was examined over the first 12 weeks post-implantation to determine if it was stable. Amplitude measurements were collected from the four arrays. As previously stated, one array was later excluded since it pulled out of the brain. However, its individual analyses are included in the supplementary data. Figure 4-7(a) shows mean amplitude (145.6 μV overall) for all viable electrodes from three arrays ($n = 238$). An overall linear decrease of 0.2 $\mu\text{V}/\text{week}$ was observed, but it was not significant at the 0.05 level ($p = 0.90$). Amplitude (191.7 μV overall) was also examined for the top 20 electrodes with the largest single-units from three arrays ($n = 60$). An overall linear increase of 2.2 $\mu\text{V}/\text{week}$ was observed, but it also was not significant at the 0.05 level ($p = 0.36$). Furthermore, the amplitude trends had small regression slopes compared to impedance.

Like impedance, the initial ramp in amplitude during the first two weeks post-implantation (all viable: 69.6 $\mu\text{V}/\text{week}$; top 20: 99.8 $\mu\text{V}/\text{week}$) stands out and is nominally consistent with a more resistive medium developing around the electrodes due to edema clearing as the injury stabilizes (Moffitt and McIntyre, 2005). However, the time points do not match since amplitude increases from week 1-2 and impedance increases from week 1-3, similar to

another study that we performed in a rodent model. Beyond week 2, the trend leveled out (all viable: $-2.3 \mu\text{V}/\text{week}$, $p = 0.07$; top 20: $-1.2 \mu\text{V}/\text{week}$, $p = 0.42$). Figure 4-7(b) shows mean amplitude at week 1, 2, 3, and 12. Week 2 was significantly different from week 1 and 12 ($p < 0.001$, multiple comparisons). However, there was no significant difference between week 2 and week 3 ($p > 0.05$, multiple comparisons).

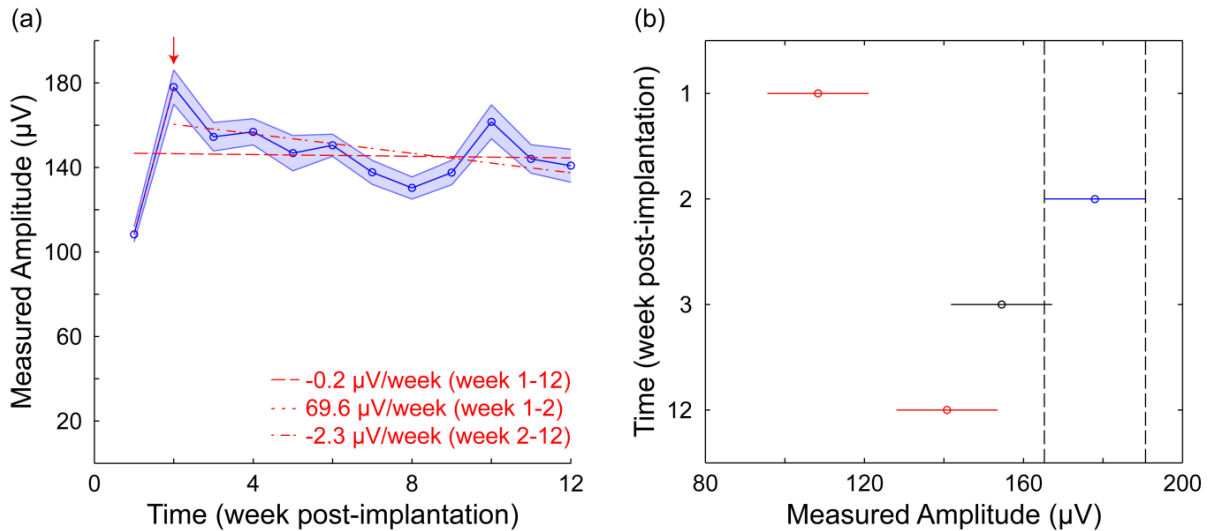


Figure 4-7 Mean amplitude over time (3/4 pooled arrays, all viable electrodes). (a) Week 1-12. Red lines are the linear regression fits. Arrow denotes week 2. Error bars denote the standard error of the mean. (b) Week 1, 2, 3, and 12. Bars denote the comparison intervals. Color denotes the test group (blue) and significantly different groups (red).

To determine if this weak amplitude trend was consistent with the computational model, a sensitivity analysis of encapsulation thickness, encapsulation resistivity, and interface resistivity was performed. With a default encapsulation and interface resistivity of 600 and $1.8e^5 \Omega\text{-cm}$, respectively, encapsulation thickness had a small effect on amplitude for thin ($t < 20 \mu\text{m}$) scars not touching the neuron, as shown in Figure 4-8(a) (untouched). For example, a 2x increase in encapsulation thickness (10 to 20 μm) resulted in a mere 1.6% decrease ($-1.4 \mu\text{V}$) in amplitude. Therefore, the model is consistent with the *in vivo* data. Between 20 and 50 μm , amplitude increased as encapsulation thickness increased (Figure 4-8(a), untouched).

Theoretically, if the neuron was to become embedded in the glial scar as it grew beyond 50 μm , then amplitude would continue increasing, eventually leveling out around 180 μV (Figure 4-8(a), embedded). This makes sense, per Ohm's law ($V = IR$), since the neuron now resides in a more resistive medium. However, if the scar was to displace the neuron as it grew beyond 50 μm , then amplitude would start decreasing (Figure 4-8(a), displaced). For example, a 4x increase in encapsulation thickness (20 to 80 μm , 30 μm displacement) resulted in a 26.8% decrease (-23.7 μV) in amplitude. This suggests that neuron displacement has more of a negative effect on waveform amplitude than the electrical properties of the glial scar and offers a possible explanation of how amplitude may increase despite scarring, as observed in the neural data.

With a default encapsulation thickness, interface resistivity, and soma position of 20 μm , $1.8 \times 10^5 \Omega\text{-cm}$, and 50 μm away from the bottom of the electrode tip, respectively, encapsulation resistivity had a moderate effect on amplitude, as shown in Figure 4-8(b). For example, a 2x increase in encapsulation resistivity (600 to 1,200 $\Omega\text{-cm}$) resulted in a 13.2% decrease (-11.7 μV) in amplitude. Furthermore, a 4x decrease (600 to 150 $\Omega\text{-cm}$, acute edema) resulted in an 8.2% increase (+7.3 μV). The increase in amplitude due to acute edema appears to contradict the increase observed during the first two weeks post-implantation that was attributed to a more resistive medium developing around the electrodes due to edema clearing as the injury stabilizes. However, this assumes that the neuron is untouched (Figure 4-8(a)) by the edematous encapsulation layer. It is more likely that the neuron becomes embedded in an edematous encapsulation upon electrode insertion, which later clears out. Alternatively, the neuron could be displaced by edema at first and then, as the swelling subsides, be moved closer to the recording site.

Interestingly, with a default encapsulation thickness, encapsulation resistivity, and soma position of 20 μm , 600 $\Omega\text{-cm}$, and 50 μm away from the bottom of the electrode tip, respectively, interface resistivity had a small effect on amplitude (Figure 4-8(b)), consistent with previous studies (Moulin et al., 2008; Nelson et al., 2008). For example, a 6x increase in interface resistivity ($1.8e^5$ to $1.1e^6$ $\Omega\text{-cm}$) resulted in a mere 0.1% decrease (-0.1 μV) in amplitude. Despite impedance increasing by a few hundreds of kilohms due to increasing interface resistivity, the same recording characteristic was observed. As previously stated, interface resistivity was better able to match the changes in impedance, and it did so while maintaining signal stability. Therefore, this aspect of the model is consistent with the *in vivo* data. However, each of these model predictions require validation by future experiments.

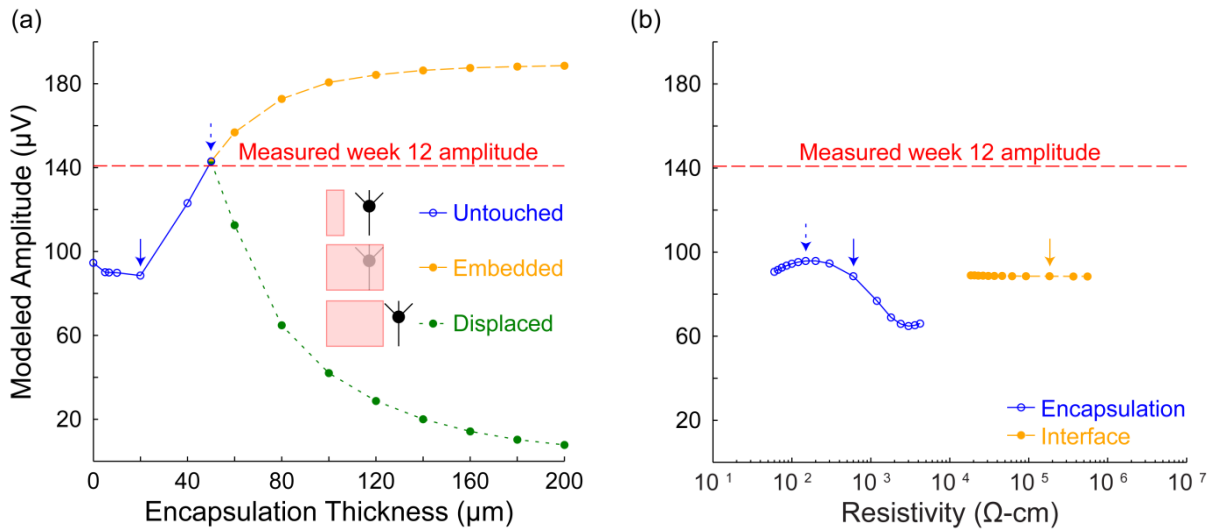


Figure 4-8 Effect of encapsulation and interface on amplitude. (a) Encapsulation thickness. In the untouched condition, the scar (red) does not contact the neuron (black) as it thickens (i.e., encapsulation thickness < 50 μm). In the embedded condition, the scar contacts and encapsulates the neuron (fixed in space) as it thickens beyond 50 μm . In the displaced condition, the scar contacts and moves the neuron (unfixed in space) as it thickens beyond 50 μm . Solid arrow denotes the default encapsulation thickness (20 μm). Dashed arrow denotes the default soma position (50 μm) relative to the electrode tip. (b) Encapsulation and interface resistivity. Simulation results are for the untouched condition in (a) (encapsulation thickness = 20 μm). Solid arrows denote the default encapsulation (600 $\Omega\text{-cm}$) and interface ($1.8e^5$ $\Omega\text{-cm}$) resistivity. Dashed arrow denotes the default encapsulation resistivity (150 $\Omega\text{-cm}$) for acute edema.

Consistent with the population data, amplitude trends for individual electrodes tended to increase during the first two weeks post-implantation, showing less variation than those of impedance, and leveled out beyond week 2. Figure 4-9 shows regression slope for all viable electrodes from three arrays at week 1-2 and 2-12, and Table 2-1 summarizes the distributions (mean \pm standard deviation). Similar distributions were observed for the top 20 electrodes. Individual electrodes had positive and negative trends. None were significant. A bootstrap analysis also yielded similar distributions. Individual electrodes also had smaller amplitude differences from week-to-week in the positive and negative directions compared to those of impedance. The distribution of week-to-week difference for all viable electrodes from three arrays at week 1-12 had a mean and standard deviation of 2.9 and 105.6 μV , respectively. Again, a similar distribution was observed for the top 20 electrodes ($n = 660, 7.2 \pm 165.8 \mu\text{V}$).

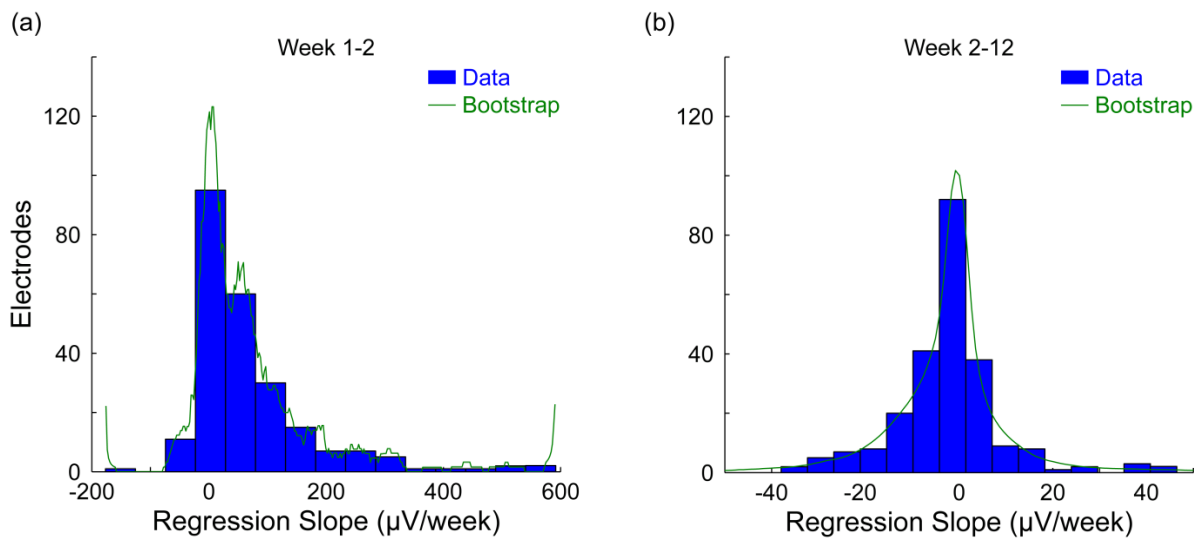


Figure 4-9 Distribution of regression slope in amplitude (all viable electrodes, 238/288). (a) Week 1-2. (b) Week 2-12.

Table 4-3 Distribution of regression slope in amplitude ($\mu\text{V}/\text{week}$)

All viable electrodes		Top 20 electrodes		Bootstrap	
Week 1-2	Week 2-12	Week 1-2	Week 2-12	Week 1-2	Week 2-12
69.6 ± 108.4	-2.3 ± 11.3	100.0 ± 150.6	-1.2 ± 18.2	70.0 ± 108.4	-2.2 ± 14.0

Relationship between Impedance and Signal Quality

Electrode impedance is often used as a predictor of signal quality. However, the computational model predicted interface resistivity to have a large effect on impedance and a small effect on amplitude. To determine if there was a relationship between impedance and amplitude in the *in vivo* data, amplitude was plotted as a function of impedance for all viable electrodes from three arrays ($n = 238$) at week 1-3 and 3-12, as shown in Figure 4-10(a, b). There was a small, positive correlation for week 1-3 ($r = 0.06$, $p = 0.10$) and 3-12 ($r = 0.03$, $p = 0.17$), suggesting that increases in impedance result in increases in amplitude. However, the correlation was not significant for either period. This weak relationship between impedance and amplitude is consistent with the model predictions regarding interface resistivity.

To determine if changes in impedance corresponded to similar changes in amplitude, week-to-week difference in amplitude was plotted as a function of week-to-week difference in impedance, as shown in Figure 4-10(c, d). There was a significant, negative correlation for week 1-3 ($r = -0.11$, $p = 0.01$) and 3-12 ($r = -0.32$, $p = 2.59e^{-51}$), suggesting that increases in impedance result in decreases in amplitude. However, the correlation was small despite its significance for both periods. This reversal in the relationship between impedance and amplitude suggests that impedance is not the best predictor of signal quality, especially since it can be manipulated independently (Purcell et al., 2009).

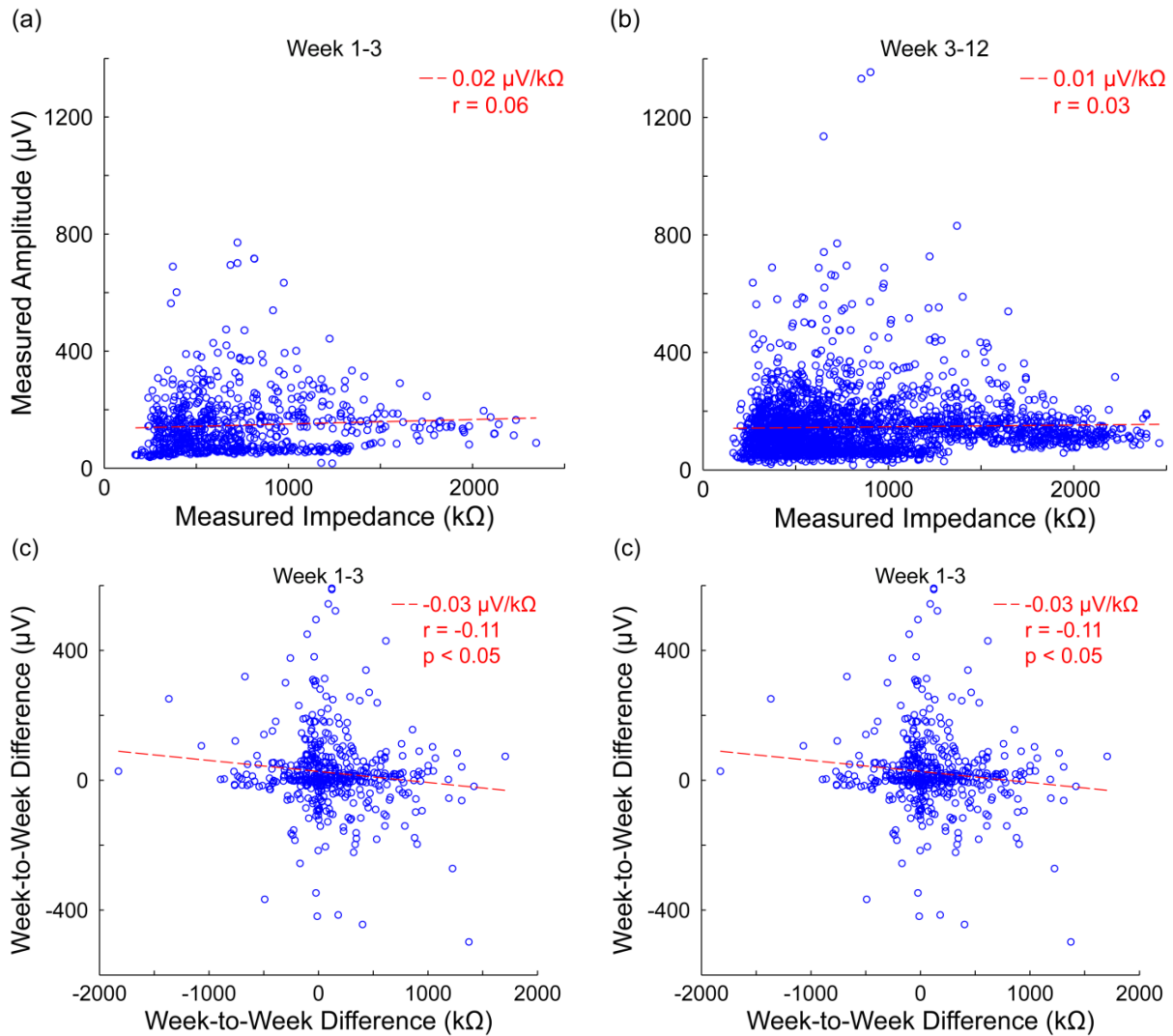


Figure 4-10 Correlation between impedance and amplitude (all viable electrodes, 238/288). (a, b) Measured amplitude versus impedance (week 1-3, 3-12). Line is the linear regression fit. (c, d) Week-to-week difference in amplitude versus week-to-week difference in impedance (week 1-3, 3-12). 9 data points were clipped from plot (d).

Increasing noise due to increasing impedance could lead to difficulty detecting action potentials even in the absence of changes in waveform amplitude. Therefore, RMS noise and SNR were examined over the first 12 weeks post-implantation to determine their trends. RMS noise and SNR measurements were collected from the four arrays. As previously stated, one array was later excluded since it pulled out of the brain. However, its individual analyses are included in the supplementary data. For the top 20 electrodes with the largest single-units from

three arrays ($n = 60$), an overall linear increase of $0.4 \mu\text{V}/\text{week}$ and decrease of $2.2e^{-4}/\text{week}$ was observed for mean RMS noise and SNR, respectively, but neither was significant at the 0.05 level ($p = 0.39$ and 0.997 , respectively). The RMS noise and SNR trends had small regression slopes. Therefore, signal quality was deemed stable despite increasing impedance over time, suggesting that noise was more biological than thermal.

Discussion

Past literature highlights glial scarring as one of the main factors affecting signal quality (Biran et al., 2005; Edell et al., 1992; Johnson et al., 2005; Otto et al., 2006; Polikov et al., 2005; Prasad and Sanchez, 2012; Stensaas and Stensaas, 1976; Szarowski et al., 2003; Turner et al., 1999; Williams et al., 2007). The scar is hypothesized to act as a high-impedance layer that electrically isolates the electrode from nearby neurons in the surrounding tissue (Johnson et al., 2005; Otto et al., 2006; Prasad and Sanchez, 2012; Williams et al., 2007). Because of this, electrode impedance is often used as a predictor of signal quality. Previous studies have reported direct correlations between scarring, impedance, and signal quality (Johnson et al., 2005; Otto et al., 2006; Prasad and Sanchez, 2012; Williams et al., 2007). However, others have reported the opposite, stating that no apparent correlation exists between impedance and signal quality (Barrese et al., 2013; Cui et al., 2003; Suner et al., 2005). Previous studies have also reported being able to acquire neural signals over extended periods of time after scar formation (Barrese et al., 2013; Chestek et al., 2011; Fraser et al., 2009; Kruger et al., 2010; Simeral et al., 2011; Suner et al., 2005). In this study, we show that the glial scar cannot adequately match *in vivo* impedance and neural recording data from chronically-implanted Utah arrays in rhesus macaques using a data-driven neural recording model. We then show how the interface between the recording site and surrounding neural tissue can better match the *in vivo* data.

Increases in electrode impedance and waveform amplitude were steep during the first three weeks post-implantation. Specifically, mean impedance and amplitude increased at a rate of 115.8 k Ω /week (Figure 4-2(a)) and 23.1 μ V/week (Figure 4-7(a)), respectively. This initial ramp in impedance and amplitude was observed across all four arrays (supplementary data), and is nominally consistent with proteins adhering to the recording site (increasing interface resistivity) and edema clearing as the injury stabilizes (increasing tissue resistivity around the electrode and neuron), respectively, in the computational model. Figure 4-7(a) shows that the time points do not match since waveform amplitude mainly ramps up from week 1-2, which is consistent with there being two separate processes that affect impedance and amplitude. A similar result was observed in another study that we performed in a rodent model (Patel, 2015).

In the model, the interface layer was better able to match the observed changes in impedance than the glial scar (Figure 4-5). A possible explanation for this is that the interface is likely much more resistive than the encapsulation layer. Therefore, scarring does not appear to be the main contributor to increasing impedance, assuming that the encapsulation layer is not dramatically more resistive than the surrounding neural tissue. Based off experimental measurements, this assumption appears to be valid (Grill and Mortimer, 1994; Haueisen et al., 2002). Furthermore, there is no significant difference in impedance between simulations with and without a scar (Figure 4-3).

The increase in amplitude observed during the first two weeks post-implantation (Figure 4-7(a)) is nominally consistent with the development of a more resistive medium around the electrode and neuron in the model (Figure 4-8(a), embedded), which can be attributed to edema clearing as the injury stabilizes (Moffitt and McIntyre, 2005). However, glial scarring can decrease amplitude by moving neurons away from the recording site (Figure 4-8(a), displaced)

(Biran et al., 2005; Edell et al., 1992). Beyond week 2, amplitude decreased at a rate of 2.3 $\mu\text{V}/\text{week}$ for a loss of 37.2 μV over the following ten weeks. This decrease is consistent with neuron displacement due to scarring, assuming a constant rate of scar growth. For example, a 10 μm displacement in the model resulted in a 21.2% decrease (-30.4 μV) in amplitude, which is consistent with the neural data. Despite the negative trend, amplitude at week 12 was not significantly different from week 3 ($p > 0.05$, multiple comparisons) (Figure 4-7(b)). By combining the electrophysiological and histological (Figure 4-4) data, it can be concluded that the tissue responses were not severe enough to isolate the electrodes from nearby neurons. Therefore, scarring does not appear to significantly affect amplitude once the scar has stabilized.

While interface resistivity had a large effect on impedance, the model did not predict it to have a large effect on amplitude (Figure 4-8(b)). For example, a 6x increase in interface resistivity (1.8e⁵ to 1.1e⁶ $\Omega\text{-cm}$) resulted in a mere 0.1% decrease (-0.1 μV) in amplitude. A possible explanation for this is that a thin interface at the recording site does not increase the resistivity of the medium that the neurons reside in, unlike glial scarring around the electrode. This is consistent with the standard assumption that the effect of the double layer at the interface on voltage measurements is negligible (Moulin et al., 2008; Nelson et al., 2008). However, this model prediction requires validation by future experiments.

Computational models are useful for performing analyses that would be difficult to implement experimentally. Since they cannot completely capture experimental conditions, assumptions have to be made when developing them and limitations have to be considered when interpreting their results. In this study, first, the brain and interface layer were assumed to be purely resistive and linear with regard to neural recordings (Bedard et al., 2004). Potential limitations with electrostatic solutions could be addressed by frequency-dependent models

coupled with electrode impedance spectroscopy measurements that account for both the resistive and capacitive properties of the interface layer and neural tissue (Lempka and McIntyre, 2013). Second, the glial scar and interface layer were modeled as individual layers of uniform thickness in the FEM. This is a large simplification since, in reality, the scar and interface consist of cells around and proteins adhered to the electrode, respectively. This limitation could be addressed by incorporating more detailed and realistic encapsulation and interface layers into the model. Third, compartments of the neuron model within the encapsulation layer (6/531 compartments within the default 20 μm -thick scar) were kept in all simulations (Moffitt and McIntyre, 2005). The physiological accuracy of this remains uncertain. However, this was done to maintain consistency between the embedded and untouched/displaced conditions examined in Figure 4-8(a). Fourth, while the model is able to capture a large range of impedances (Figure 4-5), there currently is no aspect of it that can explain the large week-to-week differences in impedance observed for individual electrodes (Figure 4-6). These differences are likely not a product of biofouling or metallization loss, which are relatively linear processes. This suggests that there is another factor crucial to the dynamics of the electrode-tissue interface and impedance measurements *in vivo* that remains to be revealed. However, it may be difficult to pinpoint due to the dynamic nature of the neural environment.

Another limitation of this study is that only a single antibody (Anti Iba1, Rabbit) was used to estimate encapsulation thickness (Figure 4-4). Iba1 is specifically expressed in resident microglia and non-resident macrophages. However, the fibrous encapsulation layer around the electrodes is mostly comprised of reactive astrocytes, which usually form a thicker and more robust encapsulation than microglia (Biran et al., 2005). While it is possible that the encapsulation thickness reported in this study is underestimated, the estimate was found to be

comparable to other observed encapsulation thicknesses (Szarowski et al., 2003; Turner et al., 1999). Furthermore, a range of encapsulation thicknesses (0-200 μm) were examined in the model with regard to impedance and amplitude, so thicker scars were accounted for. This limitation could be addressed by using additional stains (e.g., glial fibrillary acidic protein (GFAP), vimentin) and obtaining histology from more than one animal and one array.

Conclusion

Overall, the results of this study challenge current hypotheses regarding the glial scar and its effect on chronic neural recordings by suggesting that the scar does not cause an electrical problem with regard to signal quality. In the computational model, molecular elements (e.g., proteins) that adhere to the surface of the recording site (i.e., biofouling) are treated distinctly from cellular elements (e.g., microglia, astrocytes) that encapsulate the electrode (i.e., scarring). By doing so, we were able to identify interesting observations regarding the implication of the interface layer and electrode impedance. While this layer could increase impedance by hundreds of kilohms in the model, the lack of correlation between interface resistivity and waveform amplitude suggests a divergence between the effect of scarring on impedance and amplitude, which may help to explain the lack of correlation between impedance and amplitude observed by others (Barrese et al., 2013; Cui et al., 2003; Suner et al., 2005). Furthermore, glial scarring does not appear to insulate the electrodes from neural signals (Johnson et al., 2005; Otto et al., 2006; Prasad and Sanchez, 2012; Williams et al., 2007), as has been commonly thought. Rather, neuron displacement due to scar growth may be a more likely explanation for signal loss at the electrode-tissue interface over time (Biran et al., 2005; Edell et al., 1992). Previous studies have shown that it is possible to record action potentials over extended periods of time after scar formation (Barrese et al., 2013; Chestek et al., 2011; Fraser et al., 2009; Kruger et al., 2010;

Simeral et al., 2011; Suner et al., 2005). This suggests that neural signals can be obtained reliably despite scarring as long as the recording site has sufficiently low impedance after accumulating a thin layer of biofouling. Since the scar may only need a few months to stabilize, material failures may be more of a concern when dealing with longer time scales (Barrese et al., 2013; Prasad et al., 2014; Takmakov et al., 2015; Xie et al., 2014). Therefore, advancements in microelectrode technology may be expedited by focusing on improvements to the interface between the recording site and surrounding neural tissue (e.g., reduction of biofouling, preservation of metallization) rather than elimination of the glial scar.

References

- Barrese, J.C., Rao, N., Paroo, K., Triebwasser, C., Vargas-Irwin, C., Franquemont, L., Donoghue, J.P., 2013. Failure mode analysis of silicon-based intracortical microelectrode arrays in non-human primates. *J Neural Eng* 10, 066014.
- Bedard, C., Kroger, H., Destexhe, A., 2004. Modeling extracellular field potentials and the frequency-filtering properties of extracellular space. *Biophysical journal* 86, 1829-1842.
- Biran, R., Martin, D.C., Tresco, P.A., 2005. Neuronal cell loss accompanies the brain tissue response to chronically implanted silicon microelectrode arrays. *Exp Neurol* 195, 115-126.
- Cantrell, D.R., Inayat, S., Taflove, A., Ruoff, R.S., Troy, J.B., 2008. Incorporation of the electrode-electrolyte interface into finite-element models of metal microelectrodes. *J Neural Eng* 5, 54-67.
- Carnevale, N.T., Hines, M.L., 2006. *The NEURON book*. Cambridge University Press, Cambridge, UK ; New York.
- Chestek, C.A., Gilja, V., Nuyujukian, P., Foster, J.D., Fan, J.M., Kaufman, M.T., Churchland, M.M., Rivera-Alvidrez, Z., Cunningham, J.P., Ryu, S.I., Shenoy, K.V., 2011. Long-term stability of neural prosthetic control signals from silicon cortical arrays in rhesus macaque motor cortex. *J Neural Eng* 8, 045005.
- Collinger, J.L., Kryger, M.A., Barbara, R., Betler, T., Bowsher, K., Brown, E.H., Clanton, S.T., Degenhart, A.D., Foldes, S.T., Gaunt, R.A., Gyulai, F.E., Harchick, E.A., Harrington, D., Helder, J.B., Hemmes, T., Johannes, M.S., Katyal, K.D., Ling, G.S., McMorland, A.J., Palko, K., Para, M.P., Scheuermann, J., Schwartz, A.B., Skidmore, E.R., Solzbacher, F., Srikameswaran, A.V., Swanson, D.P., Swetz, S., Tyler-Kabara, E.C., Velliste, M., Wang, W., Weber, D.J., Wodlinger, B., Boninger, M.L., 2014. Collaborative approach in the development of high-performance brain-computer interfaces for a neuroprosthetic arm: translation from animal models to human control. *Clin Transl Sci* 7, 52-59.
- Cui, X., Wiler, J., Dzaman, M., Altschuler, R.A., Martin, D.C., 2003. *In vivo* studies of polypyrrole/peptide coated neural probes. *Biomaterials* 24, 777-787.
- Edell, D.J., Toi, V.V., McNeil, V.M., Clark, L.D., 1992. Factors influencing the biocompatibility of insertable silicon microshafts in cerebral cortex. *IEEE Trans Biomed Eng* 39, 635-643.
- Fraser, G.W., Chase, S.M., Whitford, A., Schwartz, A.B., 2009. Control of a brain-computer interface without spike sorting. *J Neural Eng* 6, 055004.
- Green, R.A., Hassarati, R.T., Bouchinet, L., Lee, C.S., Cheong, G.L., Yu, J.F., Dodds, C.W., Suaning, G.J., Poole-Warren, L.A., Lovell, N.H., 2012. Substrate dependent stability of conducting polymer coatings on medical electrodes. *Biomaterials* 33, 5875-5886.
- Grill, W.M., Mortimer, J.T., 1994. Electrical properties of implant encapsulation tissue. *Ann Biomed Eng* 22, 23-33.

- Hatsopoulos, N., Joshi, J., O'Leary, J.G., 2004. Decoding continuous and discrete motor behaviors using motor and premotor cortical ensembles. *J Neurophysiol* 92, 1165-1174.
- Haueisen, J., Tuch, D.S., Ramon, C., Schimpf, P.H., Wedeen, V.J., George, J.S., Belliveau, J.W., 2002. The influence of brain tissue anisotropy on human EEG and MEG. *NeuroImage* 15, 159-166.
- Henze, D.A., Borhegyi, Z., Csicsvari, J., Mamiya, A., Harris, K.D., Buzsaki, G., 2000. Intracellular features predicted by extracellular recordings in the hippocampus *in vivo*. *J Neurophysiol* 84, 390-400.
- Hochberg, L.R., Serruya, M.D., Friehs, G.M., Mukand, J.A., Saleh, M., Caplan, A.H., Branner, A., Chen, D., Penn, R.D., Donoghue, J.P., 2006. Neuronal ensemble control of prosthetic devices by a human with tetraplegia. *Nature* 442, 164-171.
- Holt, G.R., Koch, C., 1999. Electrical interactions via the extracellular potential near cell bodies. *J Comput Neurosci* 6, 169-184.
- Hoyum, P., Kalvoy, H., Martinsen, O.G., Grimnes, S., 2010. A finite element model of needle electrode spatial sensitivity. *Physiol Meas* 31, 1369-1379.
- Johnson, M.D., Otto, K.J., Kipke, D.R., 2005. Repeated voltage biasing improves unit recordings by reducing resistive tissue impedances. *IEEE Trans Neural Syst Rehabil Eng* 13, 160-165.
- Kruger, J., Caruana, F., Volta, R.D., Rizzolatti, G., 2010. Seven years of recording from monkey cortex with a chronically implanted multiple microelectrode. *Front Neuroeng* 3, 6.
- Lempka, S.F., Johnson, M.D., Moffitt, M.A., Otto, K.J., Kipke, D.R., McIntyre, C.C., 2011. Theoretical analysis of intracortical microelectrode recordings. *J Neural Eng* 8, 045006.
- Lempka, S.F., McIntyre, C.C., 2013. Theoretical analysis of the local field potential in deep brain stimulation applications. *PLoS one* 8, e59839.
- Logothetis, N.K., Kayser, C., Oeltermann, A., 2007. *In vivo* measurement of cortical impedance spectrum in monkeys: implications for signal propagation. *Neuron* 55, 809-823.
- Mainen, Z.F., Joerges, J., Huguenard, J.R., Sejnowski, T.J., 1995. A model of spike initiation in neocortical pyramidal neurons. *Neuron* 15, 1427-1439.
- McIntyre, C.C., Grill, W.M., 2001. Finite element analysis of the current-density and electric field generated by metal microelectrodes. *Ann Biomed Eng* 29, 227-235.
- Moffitt, M.A., McIntyre, C.C., 2005. Model-based analysis of cortical recording with silicon microelectrodes. *Clin Neurophysiol* 116, 2240-2250.
- Moulin, C., Gliere, A., Barbier, D., Joucla, S., Yvert, B., Mailley, P., Guillemaud, R., 2008. A new 3-D finite-element model based on thin-film approximation for microelectrode array recording of extracellular action potential. *IEEE Trans Biomed Eng* 55, 683-692.

- Nelson, M.J., Pouget, P., Nilsen, E.A., Patten, C.D., Schall, J.D., 2008. Review of signal distortion through metal microelectrode recording circuits and filters. *J Neurosci Methods* 169, 141-157.
- Nordhausen, C.T., Maynard, E.M., Normann, R.A., 1996. Single unit recording capabilities of a 100 microelectrode array. *Brain Res* 726, 129-140.
- Otto, K.J., Johnson, M.D., Kipke, D.R., 2006. Voltage pulses change neural interface properties and improve unit recordings with chronically implanted microelectrodes. *IEEE Trans Biomed Eng* 53, 333-340.
- Patel, P.R., 2015. Carbon Fiber Microelectrode Arrays for Neuroprosthetic and Neuroscience Applications. *Carbon Fiber Microelectrode Arrays for Neuroprosthetic and Neuroscience Applications*.
- Polikov, V.S., Tresco, P.A., Reichert, W.M., 2005. Response of brain tissue to chronically implanted neural electrodes. *J Neurosci Methods* 148, 1-18.
- Prasad, A., Sanchez, J.C., 2012. Quantifying long-term microelectrode array functionality using chronic *in vivo* impedance testing. *J Neural Eng* 9, 026028.
- Prasad, A., Xue, Q.S., Dieme, R., Sankar, V., Mayrand, R.C., Nishida, T., Streit, W.J., Sanchez, J.C., 2014. Abiotic-biotic characterization of Pt/Ir microelectrode arrays in chronic implants. *Front Neuroeng* 7, 2.
- Purcell, E.K., Thompson, D.E., Ludwig, K.A., Kipke, D.R., 2009. Flavopiridol reduces the impedance of neural prostheses *in vivo* without affecting recording quality. *J Neurosci Methods* 183, 149-157.
- Reimann, M.W., Anastassiou, C.A., Perin, R., Hill, S.L., Markram, H., Koch, C., 2013. A biophysically detailed model of neocortical local field potentials predicts the critical role of active membrane currents. *Neuron* 79, 375-390.
- Selvakumaran, J., Keddie, J.L., Ewins, D.J., Hughes, M.P., 2008. Protein adsorption on materials for recording sites on implantable microelectrodes. *J Mater Sci Mater Med* 19, 143-151.
- Simeral, J.D., Kim, S.P., Black, M.J., Donoghue, J.P., Hochberg, L.R., 2011. Neural control of cursor trajectory and click by a human with tetraplegia 1000 days after implant of an intracortical microelectrode array. *J Neural Eng* 8, 025027.
- Sommakia, S., Gaire, J., Rickus, J.L., Otto, K.J., 2014. Resistive and reactive changes to the impedance of intracortical microelectrodes can be mitigated with polyethylene glycol under acute *in vitro* and *in vivo* settings. *Front Neuroeng* 7, 33.
- Sommakia, S., Rickus, J.L., Otto, K.J., 2009. Effects of adsorbed proteins, an antifouling agent and long-duration DC voltage pulses on the impedance of silicon-based neural microelectrodes. *Conf Proc IEEE Eng Med Biol Soc* 2009, 7139-7142.

Stensaas, S.S., Stensaas, L.J., 1976. The reaction of the cerebral cortex to chronically implanted plastic needles. *Acta Neuropathol* 35, 187-203.

Suner, S., Fellows, M.R., Vargas-Irwin, C., Nakata, G.K., Donoghue, J.P., 2005. Reliability of signals from a chronically implanted, silicon-based electrode array in non-human primate primary motor cortex. *IEEE Trans Neural Syst Rehabil Eng* 13, 524-541.

Szarowski, D.H., Andersen, M.D., Retterer, S., Spence, A.J., Isaacson, M., Craighead, H.G., Turner, J.N., Shain, W., 2003. Brain responses to micro-machined silicon devices. *Brain Res* 983, 23-35.

Takmakov, P., Ruda, K., Scott Phillips, K., Isayeva, I.S., Krauthamer, V., Welle, C.G., 2015. Rapid evaluation of the durability of cortical neural implants using accelerated aging with reactive oxygen species. *J Neural Eng* 12, 026003.

Taylor, D.M., Tillery, S.I., Schwartz, A.B., 2002. Direct cortical control of 3D neuroprosthetic devices. *Science* 296, 1829-1832.

Thelin, J., Jorntell, H., Psouni, E., Garwicz, M., Schouenborg, J., Danielsen, N., Linsmeier, C.E., 2011. Implant size and fixation mode strongly influence tissue reactions in the CNS. *PloS one* 6, e16267.

Turner, J.N., Shain, W., Szarowski, D.H., Andersen, M., Martins, S., Isaacson, M., Craighead, H., 1999. Cerebral astrocyte response to micromachined silicon implants. *Exp Neurol* 156, 33-49.

Vetter, R.J., Williams, J.C., Hetke, J.F., Nunamaker, E.A., Kipke, D.R., 2004. Chronic neural recording using silicon-substrate microelectrode arrays implanted in cerebral cortex. *IEEE Trans Biomed Eng* 51, 896-904.

Williams, J.C., Hippensteel, J.A., Dilgen, J., Shain, W., Kipke, D.R., 2007. Complex impedance spectroscopy for monitoring tissue responses to inserted neural implants. *J Neural Eng* 4, 410-423.

Williams, J.C., Rennaker, R.L., Kipke, D.R., 1999. Long-term neural recording characteristics of wire microelectrode arrays implanted in cerebral cortex. *Brain Res Brain Res Protoc* 4, 303-313.

Xie, X., Rieth, L., Williams, L., Negi, S., Bhandari, R., Caldwell, R., Sharma, R., Tathireddy, P., Solzbacher, F., 2014. Long-term reliability of Al₂O₃ and Parylene C bilayer encapsulated Utah electrode array based neural interfaces for chronic implantation. *J Neural Eng* 11, 026016.

Chapter 5

Placing the Work in Context

The nervous system exists as over 100 billion neurons organized into networks of increasing size and complexity. These neural networks, comprising the brain, spinal cord, and peripheral nervous system, give rise to the complex, emergent phenomena that make us human, including sensation, memory, and behavior. Network dysfunction results in major neurological diseases, such as Parkinson disease, Alzheimer's, epilepsy, and central pain. Focal structural insults, including amputation, stroke, and spinal cord injury, cause negligible to long-term network disruption with diverse and widespread impact. Understanding and restoring neural circuits, through circuit repair to cure disease or through network signal modulation to ameliorate symptoms, will lead to exciting new and impactful treatment possibilities. Quantitative and computational modeling to understand nervous system function, together with cellular and electronic biointerface strategies to functionally and structurally repair damaged networks, define Restorative Neuroengineering. This novel, cutting-edge field of scientific discovery, technological development, and therapeutic innovation demands synergy and cohesion among neuroscience, engineering, kinesiology, medicine, and a broad array of other disciplines.

Accurate characterization of the spread of stimulation in the brain is important for optimizing deep brain stimulation (DBS) to treat neurological disorders (Conrad et al., 2018; Maks et al., 2009; McIntyre et al., 2004b). As DBS technology progresses towards the adoption of closed-loop stimulation paradigms, where brain signals are recorded to control how

stimulation is delivered in real-time (Ghasemi et al., 2018), an increased understanding of how neural recordings are affected by different biological factors is also key. Broadly, this dissertation utilizes finite element electrode and individual patient modeling in an effort to help improve established procedures in the field of Restorative Neuroengineering. This is shown across three studies – two of which are within the context of neural stimulation and one within neural recording.

Chapter 2 described the development of an atlas-independent, truly n-of-1 tissue activation modeling methodology for DBS and its use in mapping the optimal location of subthalamic nucleus (STN) DBS for Parkinson disease (PD). The optimal location of stimulation was mapped to the dorsolateral border of the STN, in the posterior half of the nucleus. This location varied little when motor symptoms were analyzed individually, suggesting that optimal stimulation sites for rigidity, bradykinesia, and tremor may not be unique. Therapeutic stimulation spread noticeably more in the dorsal direction, providing additional evidence for caudal zona incerta as an important DBS target (Blomstedt et al., 2012; Plaha et al., 2006). High variability in neuroanatomy, stimulation location, and motor improvement across patients highlighted the need for n-of-1 modeling approaches.

Chapter 3 applied the tissue activation modeling methodology from Chapter 2 to thalamic DBS for essential tremor and combined it with atlas-independent, n-of-1 thalamic segmentation (k-means clustering-based) to evaluate the clinical effects of DBS on an individual patient basis. Within the thalamus, the shape and size of the volume of tissue activated (VTA) was highly variable across patients. Both n-of-1 and atlas-based thalamic segmentation showed that therapeutic VTAs had significantly more overlap with motor than sensory thalamus and that sustained paresthesia VTAs had significantly more overlap with sensory thalamus than

therapeutic VTAs. However, only the n-of-1 approach showed that dysarthria/motor contraction VTAs had significantly more external stimulation than therapeutic VTAs. Overall, n-of-1 thalamic segmentation performed better than atlas-based segmentation in terms of explaining DBS side effects, especially when the thalamic anatomy of the patient differed considerably in size and shape from the atlas thalamus. Although traditional atlas-based thalamic segmentation and VTA modeling are reliable tools for general DBS planning and mechanistic study, increased accuracy at the individual patient level may be possible with atlas-independent, truly n-of-1 modeling approaches utilizing diffusion tensor imaging data.

Chapter 4 investigated the effects of gliosis and interface interactions at the electrode recording site on single-unit recording quality using a computational model incorporating impedance and neural data acquired from chronically-implanted Utah arrays in rhesus macaques (Malaga et al., 2016). Although the interface layer could increase impedance by hundreds of kilohms in the model, the lack of correlation between interface resistivity and waveform amplitude suggested a divergence between the effect of gliosis on impedance and amplitude, which may help to explain the lack of correlation between impedance and amplitude observed by other investigators (Barrese et al., 2013; Cui et al., 2003; Suner et al., 2005). Furthermore, gliosis did not appear to insulate the electrodes from neural signals (Johnson et al., 2005; Otto et al., 2006; Prasad and Sanchez, 2012; Williams et al., 2007), as has been commonly thought. Overall, this study challenged current hypotheses regarding gliosis and its effect on chronic neural recordings by suggesting that gliosis does not cause an electrical problem with regard to signal quality.

Future Directions

The significance of the work presented in this dissertation is in the n-of-1 and data-driven modeling framework that it provides – one that can be used to develop, validate, evaluate, and translate new approaches for improving clinical outcome in patients with neurological disorders on an individual basis. While computational models are useful for performing experiments that would be difficult to implement empirically, it is important to note that they cannot completely capture experimental conditions. Consequently, assumptions have to be made when developing them and limitations have to be considered when interpreting their predictions.

In the first study (Chapter 2), the evaluated DBS outcomes were limited to only the primary motor symptoms of PD: rigidity, bradykinesia, and tremor. Side effects and non-motor outcomes were not evaluated. Such outcomes can be readily incorporated into the n-of-1 modeling framework, which future studies will do. Second, only therapeutic electrode contacts and VTAs calculated from clinically optimized stimulation settings were evaluated (one active contact and VTA per hemisphere per patient). The remaining three electrode contacts were not evaluated. Tissue activation volumes associated with sub-optimal stimulation or side effects at different electrode contacts can be analyzed in the same manner, which again future studies will do. Third, the brain was assumed to be purely resistive and linear with regard to DBS (Bedard et al., 2004). Consequently, all of the VTA models built were electrostatic. While a reasonable assumption (Grant and Lowery, 2010; Howell and McIntyre, 2016; Logothetis et al., 2007; Schmidt et al., 2013), possible limitations with electrostatic solutions could be addressed by frequency-dependent models combined with impedance spectroscopy measurements that account for the resistive and capacitive properties of the tissue (Lempka and McIntyre, 2013). Lastly, tractography was not incorporated into the n-of-1 modeling framework. Several studies have used tractography to aid in identifying optimal stimulation sites to treat PD with DBS (Akram et

al., 2017; Avecillas-Chasin et al., 2019; Garcia-Gomar et al., 2017; Gunalan et al., 2017; O'Halloran et al., 2016). This is of interest because DBS is hypothesized to elicit its therapeutic effect through a combination of axonal activation and cellular inhibition (McIntyre et al., 2004a; McIntyre and Hahn, 2010). The diffusion tensor (DT) imaging data used to estimate the anisotropic tissue conductivities for each patient can also be used to perform tractography. Doing so would allow direct comparison of gray and white matter stimulation, such as the hyperdirect pathway and internal capsule, and their effects on DBS outcomes (Akram et al., 2017; Chen et al., 2018; Gunalan et al., 2017).

In the second study (Chapter 3), the primary limitation came from the unavailability of histological data to evaluate the thalamic segmentations generated by the DT-based k-means clustering algorithm. Another limitation was the resolution of the DT imaging, which was lower than that of the magnetic resonance and computed tomography imaging. Acquiring higher resolution DT imaging by modifying the imaging protocol would address this limitation, but would likely require patients to undergo longer scan times. k-means clustering was used as a proxy for local histological analysis. As an alternative approach, 7 T field strength MR imaging has been used to identify thalamic subnuclei and other subcortical structures (Abosch et al., 2010; Xiao et al., 2016). Other strategies have used measures of diffusivity, such as functional connectivity and tractography, to segment the thalamus (Akram et al., 2018; Behrens et al., 2003; Elias et al., 2012; Lambert et al., 2017). Such approaches have also been applied to DBS targeting (Akram et al., 2018; Coenen et al., 2011; Kim et al., 2016). Future studies incorporating alternative strategies for segmenting the thalamus may further improve the n-of-1 thalamic segmentation algorithm.

In the third (and final) study (Chapter 4), the brain and interface layer were assumed to be purely resistive and linear with regard to neural recordings (Bedard et al., 2004) (similar to the first study). Again, possible limitations with electrostatic solutions could be addressed by frequency-dependent models combined with electrode impedance spectroscopy measurements that account for the resistive and capacitive properties of the interface layer and tissue (Lempka and McIntyre, 2013). Second, gliosis and the interface layer were modeled as separate layers of uniform thickness. This was a large simplification since, in reality, gliosis and the interface consist of cells surrounding and proteins adhered to the electrode, respectively. This limitation could be addressed by incorporating more detailed and realistic encapsulation and interface layers into the model. Lastly, while the model was able to capture a large range of impedances, there currently is no aspect of it that can explain the large week-to-week differences in impedance observed for individual electrodes. Those differences were likely not a product of biofouling or metallization loss, which are relatively linear processes. This finding suggests that there is another factor crucial to the dynamics of the electrode-tissue interface and impedance measurements *in vivo* that remains to be revealed. However, it may be difficult to pinpoint due to the dynamic nature of the neural environment. Future studies in closed-loop DBS could use a similar modeling approach to investigate the effect of gliosis on recordings from multiple neurons (local field potentials). Due to the greater quantity of neurons available to record from at this larger electrode scale (millimeters versus micrometers), glial scarring may have even less of an effect on the stability of DBS recordings. However, this would depend on the extent of tissue damage, which is much greater when implanting a DBS lead compared to a microelectrode.

To conclude, as insight regarding stimulation spread in the brain increases, the n-of-1 and data-driven modeling approaches described in this dissertation can be applied to other conditions

to inform novel brain stimulation strategies and help bridge the gap between model-based evidence and clinical practice.

References

- Abosch, A., Yacoub, E., Ugurbil, K., Harel, N., 2010. An assessment of current brain targets for deep brain stimulation surgery with susceptibility-weighted imaging at 7 tesla. *Neurosurgery* 67, 1745-1756; discussion 1756.
- Akram, H., Dayal, V., Mahlknecht, P., Georgiev, D., Hyam, J., Foltynie, T., Limousin, P., De Vita, E., Jahanshahi, M., Ashburner, J., Behrens, T., Hariz, M., Zrinzo, L., 2018. Connectivity derived thalamic segmentation in deep brain stimulation for tremor. *Neuroimage Clin* 18, 130-142.
- Akram, H., Sotiropoulos, S.N., Jbabdi, S., Georgiev, D., Mahlknecht, P., Hyam, J., Foltynie, T., Limousin, P., De Vita, E., Jahanshahi, M., Hariz, M., Ashburner, J., Behrens, T., Zrinzo, L., 2017. Subthalamic deep brain stimulation sweet spots and hyperdirect cortical connectivity in Parkinson's disease. *NeuroImage* 158, 332-345.
- Avecillas-Chasin, J.M., Alonso-Frech, F., Nombela, C., Villanueva, C., Barcia, J.A., 2019. Stimulation of the Tractography-Defined Subthalamic Nucleus Regions Correlates With Clinical Outcomes. *Neurosurgery*.
- Barrese, J.C., Rao, N., Paroo, K., Triebwasser, C., Vargas-Irwin, C., Franquemont, L., Donoghue, J.P., 2013. Failure mode analysis of silicon-based intracortical microelectrode arrays in non-human primates. *J Neural Eng* 10, 066014.
- Bedard, C., Kroger, H., Destexhe, A., 2004. Modeling extracellular field potentials and the frequency-filtering properties of extracellular space. *Biophysical journal* 86, 1829-1842.
- Behrens, T.E.J., Johansen-Berg, H., Woolrich, M.W., Smith, S.M., Wheeler-Kingshott, C.A.M., Boulby, P.A., Barker, G.J., Sillery, E.L., Sheehan, K., Ciccarelli, O., Thompson, A.J., Brady, J.M., Matthews, P.M., 2003. Non-invasive mapping of connections between human thalamus and cortex using diffusion imaging. *Nat Neurosci* 6, 750-757.
- Blomstedt, P., Fytagoridis, A., Astrom, M., Linder, J., Forsgren, L., Hariz, M.I., 2012. Unilateral caudal zona incerta deep brain stimulation for Parkinsonian tremor. *Parkinsonism Relat Disord* 18, 1062-1066.
- Chen, Y., Ge, S., Li, Y., Li, N., Wang, J., Wang, X., Li, J., Jing, J., Su, M., Zheng, Z., Luo, T., Qiu, C., Wang, X., 2018. Role of the Cortico-Subthalamic Hyperdirect Pathway in Deep Brain Stimulation for the Treatment of Parkinson Disease: A Diffusion Tensor Imaging Study. *World Neurosurg* 114, e1079-e1085.
- Coenen, V.A., Allert, N., Madler, B., 2011. A role of diffusion tensor imaging fiber tracking in deep brain stimulation surgery: DBS of the dentato-rubro-thalamic tract (drt) for the treatment of therapy-refractory tremor. *Acta Neurochir (Wien)* 153, 1579-1585; discussion 1585.
- Conrad, E.C., Mossner, J.M., Chou, K.L., Patil, P.G., 2018. Atlas-Independent, Electrophysiological Mapping of the Optimal Locus of Subthalamic Deep Brain Stimulation for the Motor Symptoms of Parkinson Disease. *Stereotact Funct Neurosurg* 96, 91-99.

- Cui, X., Wiler, J., Dzaman, M., Altschuler, R.A., Martin, D.C., 2003. *In vivo* studies of polypyrrole/peptide coated neural probes. *Biomaterials* 24, 777-787.
- Elias, W.J., Zheng, Z.A., Domer, P., Quigg, M., Pouratian, N., 2012. Validation of connectivity-based thalamic segmentation with direct electrophysiologic recordings from human sensory thalamus. *NeuroImage* 59, 2025-2034.
- Garcia-Gomar, M.G., Soto-Abraham, J., Velasco-Campos, F., Concha, L., 2017. Anatomic characterization of prelemniscal radiations by probabilistic tractography: implications in Parkinson's disease. *Brain structure & function* 222, 71-81.
- Ghasemi, P., Sahraee, T., Mohammadi, A., 2018. Closed- and Open-loop Deep Brain Stimulation: Methods, Challenges, Current and Future Aspects. *J Biomed Phys Eng* 8, 209-216.
- Grant, P.F., Lowery, M.M., 2010. Effect of dispersive conductivity and permittivity in volume conductor models of deep brain stimulation. *IEEE Trans Biomed Eng* 57, 2386-2393.
- Gunalan, K., Chaturvedi, A., Howell, B., Duchin, Y., Lempka, S.F., Patriat, R., Sapiro, G., Harel, N., McIntyre, C.C., 2017. Creating and parameterizing patient-specific deep brain stimulation pathway-activation models using the hyperdirect pathway as an example. *PloS one* 12, e0176132.
- Howell, B., McIntyre, C.C., 2016. Analyzing the tradeoff between electrical complexity and accuracy in patient-specific computational models of deep brain stimulation. *J Neural Eng* 13, 036023.
- Johnson, M.D., Otto, K.J., Kipke, D.R., 2005. Repeated voltage biasing improves unit recordings by reducing resistive tissue impedances. *IEEE Trans Neural Syst Rehabil Eng* 13, 160-165.
- Kim, W., Chivukula, S., Hauptman, J., Pouratian, N., 2016. Diffusion Tensor Imaging-Based Thalamic Segmentation in Deep Brain Stimulation for Chronic Pain Conditions. *Stereotact Funct Neurosurg* 94, 225-234.
- Lambert, C., Simon, H., Colman, J., Barrick, T.R., 2017. Defining thalamic nuclei and topographic connectivity gradients *in vivo*. *NeuroImage* 158, 466-479.
- Lempka, S.F., McIntyre, C.C., 2013. Theoretical analysis of the local field potential in deep brain stimulation applications. *PloS one* 8, e59839.
- Logothetis, N.K., Kayser, C., Oeltermann, A., 2007. *In vivo* measurement of cortical impedance spectrum in monkeys: implications for signal propagation. *Neuron* 55, 809-823.
- Maks, C.B., Butson, C.R., Walter, B.L., Vitek, J.L., McIntyre, C.C., 2009. Deep brain stimulation activation volumes and their association with neurophysiological mapping and therapeutic outcomes. *J Neurol Neurosurg Psychiatry* 80, 659-666.
- Malaga, K.A., Schroeder, K.E., Patel, P.R., Irwin, Z.T., Thompson, D.E., Nicole Bentley, J., Lempka, S.F., Chestek, C.A., Patil, P.G., 2016. Data-driven model comparing the effects of glial

scarring and interface interactions on chronic neural recordings in non-human primates. *J Neural Eng* 13, 016010.

McIntyre, C.C., Grill, W.M., Sherman, D.L., Thakor, N.V., 2004a. Cellular effects of deep brain stimulation: model-based analysis of activation and inhibition. *J Neurophysiol* 91, 1457-1469.

McIntyre, C.C., Hahn, P.J., 2010. Network perspectives on the mechanisms of deep brain stimulation. *Neurobiol Dis* 38, 329-337.

McIntyre, C.C., Mori, S., Sherman, D.L., Thakor, N.V., Vitek, J.L., 2004b. Electric field and stimulating influence generated by deep brain stimulation of the subthalamic nucleus. *Clin Neurophysiol* 115, 589-595.

O'Halloran, R.L., Chartrain, A.G., Rasouli, J.J., Ramdhani, R.A., Kopell, B.H., 2016. Case Study of Image-Guided Deep Brain Stimulation: Magnetic Resonance Imaging–Based White Matter Tractography Shows Differences in Responders and Nonresponders. *World Neurosurgery*.

Otto, K.J., Johnson, M.D., Kipke, D.R., 2006. Voltage pulses change neural interface properties and improve unit recordings with chronically implanted microelectrodes. *IEEE Trans Biomed Eng* 53, 333-340.

Plaha, P., Ben-Shlomo, Y., Patel, N.K., Gill, S.S., 2006. Stimulation of the caudal zona incerta is superior to stimulation of the subthalamic nucleus in improving contralateral parkinsonism. *Brain* 129, 1732-1747.

Prasad, A., Sanchez, J.C., 2012. Quantifying long-term microelectrode array functionality using chronic *in vivo* impedance testing. *J Neural Eng* 9, 026028.

Schmidt, C., Grant, P., Lowery, M., van Rienen, U., 2013. Influence of uncertainties in the material properties of brain tissue on the probabilistic volume of tissue activated. *IEEE Trans Biomed Eng* 60, 1378-1387.

Suner, S., Fellows, M.R., Vargas-Irwin, C., Nakata, G.K., Donoghue, J.P., 2005. Reliability of signals from a chronically implanted, silicon-based electrode array in non-human primate primary motor cortex. *IEEE Trans Neural Syst Rehabil Eng* 13, 524-541.

Williams, J.C., Hippensteel, J.A., Dilgen, J., Shain, W., Kipke, D.R., 2007. Complex impedance spectroscopy for monitoring tissue responses to inserted neural implants. *J Neural Eng* 4, 410-423.

Xiao, Y., Zitella, L.M., Duchin, Y., Teplitzky, B.A., Kastl, D., Adriany, G., Yacoub, E., Harel, N., Johnson, M.D., 2016. Multimodal 7T Imaging of Thalamic Nuclei for Preclinical Deep Brain Stimulation Applications. *Front Neurosci* 10, 264.